Lens
European Laboratory for
Non-Linear Spectroscopy

Università
degli Studi
Firenze

International Doctorate in
Atomic and Molecular Photonics

XXVIII ciclo

Ultracold atoms in three-dimensional disorder:

measurement of the mobility edge
and effect of weak interactions

Giulia Semeghini

Supervisor:
prof. Giovanni Modugno

2012/2015

Ringraziamenti

The important thing is not to stop questioning. Curiosity has its own reason for existing. One cannot help but be in awe when he contemplates the mysteries of eternity, of life, of the marvelous structure of reality. It is enough if one tries merely to comprehend a little of this mystery every day. Never lose a holy curiosity.

La cosa importante è non smettere mai di interrogarsi. La curiosità esiste per ragioni proprie. Non si può fare a meno di provare riverenza quando si comtemplano i misteri dell'eternità, della vita, della meravigliosa struttura della realtà. Basta cercare di capire un po' di questo mistero ogni giorno. Non perdere mai una sacra curiosità.

(A. Einstein)

Il mestiere del ricercatore è un mestiere bellissimo e strano. Per semplice senso del dovere o desiderio di fama si combina poco. Serve la curiosità di conoscere come stanno le cose e l'umiltà di accettare che la realtà è sempre più grande di quel che ne hai capito. La più profonda gratitudine rispetto a questi tre anni di dottorato è a chi mi è stato maestro ed amico in questo. In primis il mio supervisor Giovanni Modugno, che è curioso in senso assoluto, che ne farebbe (e ne fa!) mille, perchè gli interessa tutto. Lo ringrazio perchè mi ha insegnato a guardare le cose facendomi le domande giuste, perchè ha riposto in me una fiducia esagerata, e perchè in questo mi ha fatto crescere tantissimo. Ringrazio Manu, che è stato il mio "fratello maggiore", mi ha insegnato i trucchi del mestiere ed è stato una quotidiana provocazione, con il suo instancabile desiderio di capire e fare cose nuove. Ringrazio il prof. Massimo Inguscio, perchè ospitandomi nel suo gruppo di ricerca mi ha dato l'opportunità di fare un'esperienza di lavoro stupenda. Ringrazio Marco Fattori, perchè ha lo sguardo del bambino e l'intelligenza dello scienziato. La stima che ripone in me, nonostante i miei limiti e i miei metodi "sportivi", è uno sprone continuo a imparare questo lavoro. Ringrazio Giacomo, che ha avuto la pazienza di sopportarmi per tutto questo tempo e di essermi amico nonostante tutto! Ringrazio tutte le persone con cui ho lavorato, tra cui Patricia, Andreas, Simon, Sanjukta, e i nuovi arrivati Leonardo e Giovanni. Ringrazio quest'ultimo perchè il suo entusiasmo è una compagnia quotidiana e un inaspettato aiuto. Ringrazio gli amici della BEC2, Luca, Eleonora, Lorenzo, Simona e Giulia, affezionati compagni della pausa pranzo. Ringrazio tutte le persone nel gruppo di Atomi Freddi del LENS, che in diversi modi ed occasioni mi hanno insegnato tanto. Una menzione particolare a Giacomo Roati, capofila dei milanesi in terra fiorentina.

Ci sono tanti amici da ringraziare, per tante e diverse ragioni. Ci sono quelli sparsi per il mondo che fanno ricerca come me e che sono una preziosissima compagnia su tutte le domande che sorgono in questo lavoro. Ci sono i tanti che fanno lavori completamente diversi, ma che continuano a chiedermi di spiegare loro che cosa faccio: quante cose ho capito nel tentare i più fantasiosi racconti a pubblici inesperti! La ragione comune della mia gratitudine è l'irrinunciabile compagnia che siete alla mia vita, che custodisce e fa crescere la verità di me, particolarmente dentro al lavoro.

Ringrazio tutta la mia famiglia, che ha contribuito in modo decisivo all'esperienza di questi anni: le preghiere della nonna Carla, il sostegno degli zii, la testimonianza bella di fratelli e loro consorti, e infine la meraviglia dei nipoti, sono stati un aiuto bello e gratuito. In particolare ringrazio i miei genitori: inutile dire che senza di loro non sarebbe stato possibile nulla. Li ringrazio perchè ancora oggi guardano la mia vita con la discrezione e lo stupore di chi osserva una cosa cara, ma che non gli appartiene. Il bene che mi volete mi rende libera di vivere questa bella avventura che è la mia vita.

Contents

Chapter

1 Introduction

When approaching the topic of Anderson localization, one is certainly prejudiced in favor of it by a simple fact: this phenomenon has been discovered more than 50 years ago and intensively studied during all this time; nonetheless it is still at the center of a lively debate and a number of works concerning with it continue to be published unabated. During the three years of my PhD I have had the opportunity of taking on the question about the origin of this huge interest about AL. I must confess that I came in something much richer than I expected.

In 1958 P. W. Anderson found out that the presence of disorder in crystal lattices can have dramatic effects on the electronic transport properties, such that it can turn a metallic material into an insulator [1]. The origin of this is a purely quantum effect: the multiple scattering of a single electron by randomly distributed defects causes a destructive interference effect on its wavefunction, leading to localization on a finite region of space. It is then a single-particle phenomenon, simply related to the wave nature of quantum particles. It took quite some time to understand the importance of this discovery, but, since the time it started to be carefully considered, it became the focus of a lively and widespread interest. The reasons for this are various. On one side there is undoubtedly the relevance of an investigation about it to understand a number of insulating regimes in condensed matter physics. On the other hand, the peculiar properties of this phenomenon, ranging from its ubiquitous nature to the quantum phase transition related to it, gave rise to a fundamental interest about it [2].

The fact that, after almost 60 years of intense study, researchers are still debating about AL highlights also another point: it is not simple at all to investigate it. From a theoretical point of view, disordered systems are certainly more demanding than ordered ones, due to the increased degree of complexity. On the experimental side, while disorder is not so difficult to get, it is much more intricate to control and characterize it (just think for example to the case of disorder in crystal lattices).

A clear example of the difficulty in answering some crucial questions about AL takes us to the main theme of the present thesis. One of the aspects immediately identified in the very first paper by Anderson [1] was the existence of a critical condition for localization. In the specific case considered there he noticed that, given a certain amount of disorder in the system, the occurence of localization depends on the electronic concentration. Later on, N. Mott conceived the idea of a *mobility edge*, that is an energy threshold separating localized low-energy states from extended ones [3]. We can therefore say that the problem of the localization threshold is the oldest issue concerning with AL but it is still eluding a full understanding.

The work of this thesis engages in this long-standing debate, trying to provide a significant contribution to the solution of this fundamental problem: what is the critical energy for localization and how does it depend on the disorder strength?

The basic resource in this endeavour is the employment of ultracold quantum gases. In the past few decades these physical systems have proved to be an extremely versatile tool for the investigation of complex quantum phenomena. They are indeed increasingly used as “quantum simulators”, since they offer an unprecedented control on the fundamental parameters of the system, allowing to reproduce the main features of other physical systems under well known conditions.

This is exactly the spirit of the work I am going to present. The original context of the discovery of AL, and also the one in which it is most relevant, is that of disordered electronic systems. Nontheless an experimental study of AL with electrons has proved to be difficult, due to the effect of Coulomb interactions, which turn the Anderson single-particle phenomenon into a much more intricate one [4]. Using ultracold atoms, we dispose of a sample of quantum particles whose mutual interactions can be tuned to zero. Placing them in a disordered optical potential we can study their transport properties and detect the occurrence of the Anderson transition.

A full assessment of the non-interacting problem is a prerequisite for the even more interesting issue of the interplay between disorder and interactions. This is the realistic situation of electrons in solids and it can be again simulated with ultracold atoms, by tuning the scattering length to finite values.

In Chapter 2 I draw an essential picture of the rich context of the study about Anderson localization, focusing in particular on the problem of the mobility edge. I report the main theoretical and experimental results about the Anderson transition, which represent an instrumental background to our work. In Chapters 3 and 4 I describe the experimental setup we used, i.e. a Bose-Einstein condensate of potassium-39 atoms placed in a disordered optical potential realized by means of laser speckles. In Chapter 5 I present the novel experimental techniques we designed to determine the position of the mobility edge and I report the results we obtained. I also report some preliminary results about the effects of weak interactions on the localization problem. Finally in Chapter 6 I draw the conclusions of this work and its main outlook.

An exemplary demonstration of the versatility of ultracold gases to investigate quantum phenomena is provided by the fact that during my PhD I actually studied, with the same experimental setup, two other major topics besides Anderson localization, i.e. the Efimov effect in the collisional properties of ^{39}K [5] and the observation of a quantum phase transition with parity-simmetry breaking in a double-well potential [6]. In order to preserve the coherence of this thesis, I decided to concentrate the discussion presented here on the work in which I was the main participant, referring the reader to the cited papers for an insight on the other topics.

Chapter

2

Anderson localization and the problem of the mobility edge

During the rich history of Anderson localization (AL), a number of excellent reviews have been written to account for the many results obtained in the field. For this reason it is certainly no use for me to try and provide a complete overview on the many interesting aspects of it. Nonetheless, in the work I carried out during my PhD, I found out that dealing with AL requires to be aware of the ample context of this research field. AL interested theoretical and experimental groups from all over the world since the half of the past century, who developed a number of theoretical approaches and investigated a variety of physical systems to answer the many questions concerning with it. Keeping trace of this rich past is useful on one side to draw a clear picture of the knowledge reached about the phenomenon, and on the other hand it surely helps in understanding the lively interest about it at the present time. I will then try to retrace a path through the research about AL in the past few decades, in order to focus the main results obtained about the specific topic of this thesis, i.e. the Anderson transition and the problem of the mobility edge, which is certainly one of the fundamental and most interesting features of AL.

One of the most fascinating aspects of AL lies in its universality. Being its microscopic origin related to wave interference in a medium with a certain degree of randomness, AL needs few essential ingredients to occur. For this reason it has been observed in a variety of systems, ranging from quantum particles to classical waves. Despite the discovery of AL initially concerned electrons in disordered lattices, since the end of the 1980s the phenomenon has been investigated in many different contexts. In the following there will be no discontinuity in the presentation of the resuls obtained in one or the other of this contexts, since the majority of them equally holds in every physical system, provided that some basic conditions are verified.

In Sec. 2.1 I introduce how P. Anderson figured out the dramatic effect of disorder on the conduction properties of solids and the following success of the phenomenon in the context of metal-insulator transitions. In Secs. 2.2 and 2.3 I provide a brief overview of the theoretical and experimental results that have been relevant for the comprehension of the Anderson transition and that are useful for a comparison to our results. Finally in Sec. 2.4 I summarize what is the state-of-the-art, thus clarifying which are the firm points and the open questions about the mobility edge and the critical behaviors in its vicinity.

2.1 From 1958 to 1970s: discovery and success of Anderson localization

2.1.1 1958: "Absence of diffusion in certain random lattices"

The discovery of AL dates back to almost 60 years ago. In the mid-fifties G. Feher's group at Bell Labs was performing experiments on doped semiconductors, where they observed the anomalous localization of a spin excitation [7]. This observation stimulated P. W. Anderson to work out the first systematic treatment of the effects of a disordered potential on the transport of particles. In his famous paper from 1958 [1], he presented a simple model to study the transport of electrons or excitations in a cubic lattice with random on-site energies. This work had to completely change the established understanding of electronic transport in solids. It was of course already known that randomness was a relevant feature in solid state systems, connected with the presence of impurities, vacancies and dislocations in the otherwise ordered structures of crystal lattices. The traditional view was that the presence of disorder in the lattice caused the Bloch waves to lose phase coherence on the length scale of the mean free path, but the wave function remained extended throughout the sample. Anderson found out that something different can happen, i.e. that for strong enough disorder the wave function may become localized. In this concept of "strong enough disorder" we can identify the first primordial definition of what was later called *mobility edge*. He indeed discovered that there is a critical condition for localization to occur, which is defined as a relation between the ability of the particle to move through the lattice, in this case determined by the hopping between neighbouring sites, and the disorder strength.

In the introduction of his paper, Anderson stated:

> *"In this paper, in fact, we attempt only to construct, for such a system, the simplest model we can think of which still has some expectation of representing a real physical situation reasonably well, and to prove a theorem about the model. The theorem is that at sufficiently low densities, transport does not take place; the exact wave functions are localized in a small region of space."*

The simplest model he could think of was that of a cubic lattice in tight-binding approximation, where each electron is preferably bound to one ion of the lattice and it has a certain probability to hop from one site to the next by quantum tunneling. The system Hamiltonian can be written as:

$$H = -V \sum_{\langle i,j \rangle} (a_i^\dagger a_i + h.c) + \sum_i \epsilon_i a_i^\dagger a_i, \tag{2.1}$$

where i, j are the indexes for the lattice sites, a_i and $a_i^\dagger$ are the annihilation and creation operators of the electron on site i, V is the hopping amplitude between next-neighbouring sites, $\langle i, j \rangle$ are the pairs of next-neighbouring sites and ϵ_i is the on-site potential energy. Disorder is inserted in the system by considering that the on-site energies are random variables uniformly distributed between $-W/2$ and $W/2$, where W is the disorder amplitude.

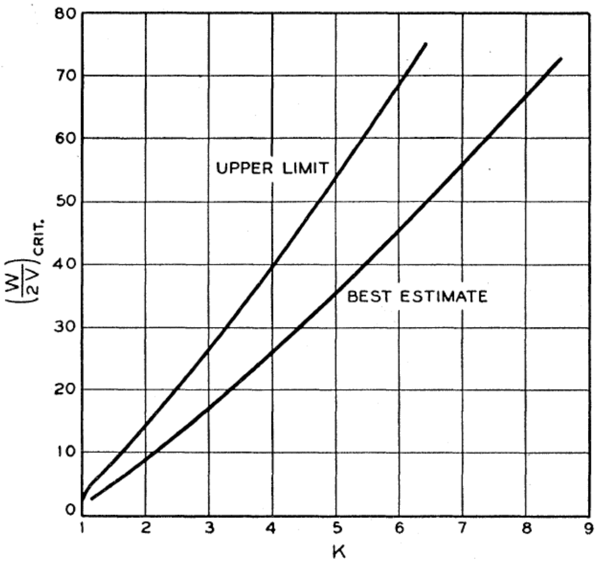

Figure 2.1 | The critical parameter for localization in Anderson's paper fom 1958. The critical value of W/V is plotted as a function of the connectivity K. The figure is taken from [1].

Anderson provided numerical estimations of the critical parameter for localization, defined by the ratio W/V. I report in Fig. 2.1 the plot of the critical W/V as a function of the system parameter K, defined as the "connectivity" of the localized electronic states. I am not interested in the exact meaning of these results, since the curves plotted there have little to do with the present concept of mobility edge. The graph I report here has the only purpose to show that the problem of determining the critical conditions for localization is at the heart of the same discovery of Anderson localization.

2.1.2 The idea of *mobility edge* and metal-insulator transitions

The importance of Anderson's work was not immediately understood, not even by Anderson himself. It was only in the 1970s, mainly thanks to the work carried out by N. Mott, that the Anderson mechanism for localization started to be appreciated and intensively studied.

Mott's merit in understanding the importance of Anderson's discovery was so significant that the two shared the Nobel Prize in 1977 for their work on disordered systems. Among many contributions that Mott brought to this field is the concept of *mobility edge*. He was indeed the first who focused that, for a fixed amount of disorder in a system, there exists an energy threshold separating localized low-energy states from extended ones. The name he gave to this critical energy manifests the connection between the nature of the energy eigenstates and the conduction properties of the whole system. Below the threshold the mobility of electrons is inhibited and no current flow can occur in the sample, at least at zero temperature. This idea immediately revealed the possible relation between AL and the *metal-insulator transitions* observed in solids. It was indeed the prospect that the newly discovered phenomenon could help to answer a number of unsolved questions in that field that determined the success of AL.

I find it useful here to briefly recall the problem of metal-insulator transitions (MITs) as it was known at the time, since it allows to understand the big efforts that followed Anderson's work and that tried to explore the connection between AL and the conduction properties of certain materials. Besides the historical interest, this also introduces us to one of the oldest but still least understood problems of condensed matter, where our investigation on ultracold gases could help to find long-awaited answers.

In the two decades before Anderson's discovery, it became apparent that the band theory of solids, who had had a great success in explaining the general behavior of condensed matter, failed to describe phenomena relative to the conducting/insulating nature of certain materials. There is indeed a class of compounds which according to band theory should be metallic conductors and are in fact insulators. The question about the origin of this unexpected behavior became even more urgent due to the fact that the materials affected by this kind of phenomena are often the most relevant for technological purposes, as it is the case for doped semiconductors or silicon MOSFETs.

The lively debate about the mechanisms underlying these unexpected insulating regimes led to the conviction that the states of electrons had to be qualitatively different in conductors and insulators, at least at sufficiently low temperature. A signature of that is the different zero-temperature limit of the conductivity. In nonmagnetic metals the conductivity tends to a finite value, whereas in many insulators it drops to zero exponentially with the inverse of the temperature. The origin of this discrepancy was ascribed to the extended or localized nature of the charge carriers in metals and insulators respectively. The distinction between metals and insulators becomes then sharp at zero temperature, indicating that metal-insulator transitions have to be classified as *quantum phase transitions*.

A first mechanism driving certain MITs was discovered in 1949 by N. Mott, who argued that the correlation effects associated with electron-electron interactions could lead to localization of the electronic eigenstates on the single sites of the periodic lattice. When the lattice has integer filling per unit cell, then the electrons can be mobile only if they have enough kinetic energy to overcome the Coulomb energy which repels them from hopping to neighbouring sites. In the narrow band limit, when tunneling is much smaller than Coulomb repulsion, the electrons do not have enough kinetic energy, and a gap opens in the single-particle excitation spectrum, leading to the so-called *Mott insulating* phase.

Mott's discovery helped in understanding a number of insulating regimes, but it could not complete the picture for all the observed phenomena. Given this scenario one can better understand why N. Mott became so enthusiastic about Anderson's work. He had just found out a different mechanism able to localize the electronic eigenstates. Thanks to their joint efforts it was then possible to identify Anderson localization as a second mechanism at the basis of MITs. While in the first case localization was due to Coulomb interactions, in this case the transition is driven by *disorder*.

One of the main differences between Mott and Anderson transitions is that, while the first presents a gap related to the energy cost of hopping in an occupied site, the second is *gapless*. This is indeed a distinctive feature of the Anderson transition, which displays a number of related phenomena, among which the so-called "variable range hopping conductivity" [2].

2.2 Theoretical approaches to Anderson localization

The experimental investigation of AL in solid state systems immediately proved to be challenging, since the presence of Coulomb interactions significantly modifies the single-particle picture of the Anderson model. For this reason, most of the intial efforts to better understand the Anderson phenomenon were performed from the theoretical point of view. In the present Section I will introduce two of the main theoretical approaches that gave significant contributions to the field. The first one, which is also the earliest, is the scaling theory of localization. It will help in clarifying a general picture of the phenomenon, introducing the role of dimensionality and the different expected regimes. The second is the self-consistent theory of localization. It contributes to catch the microscopic mechanism at the origin of AL, providing an analytic, albeit perturbative, description of it. Furthermore, I briefly report some early results of the numerical simulations, which are a powerful tool for the predictions about the mobility edge.

2.2.1 Scaling theory of localization

In general terms, scaling theories are those which describe the relevant properties of a system by considering their behavior under changes of the system size. In this way they can capture those features that are important on a macroscopic scale, without taking care of the microscopic details. In the 1960s scaling arguments started to be used for describing phase transitions and critical phenomena, which are an exemplary case where macroscopic changes of a system occur, driven by some control parameter.

An early formulation of a scaling approach to AL was proposed by Thouless and coworkers in the mid-seventies [8]. Their ideas were then took up by the so-called "gang of four" (Abrahams, Anderson, Licciardello and Ramakrishnan), who combined them with perturbation theory and worked out the first complete formulation of a scaling theory of localization [9].

The idea at the basis of this theory is very simple. A solid sample in any dimensions d is thought of as made of n^d elementary building blocks of size L^d. The scaling hypothesis assumes that the properties of the $(nL)^d$ hypercube is only a function of the properties of the elementary L^d one. Moreover, they assume that the metallic/insulating regime of the system can be identified by making use of a single parameter, i.e. the dimensionless conductance g. It is defined as the ratio $g = G/(e^2/\hbar)$, where G is the conductance and e is the electron charge. If one considers a single block as in Fig.2.2, the value of its conductance will be proportional to the ratio:

$$g \propto \frac{\Delta E}{\delta W}, \tag{2.2}$$

where ΔE is the coupling strength between eigenstates in neighbouring blocks and δW is the average spacing between the energy levels. The conductance was argued to be determined by the interplay of these two energy scales. ΔE couples the states in neighbouring blocks and favors propagation. It therefore dominates in the regime of weak disorder, allowing the admixtures of electronic states and thus the conduction of currents through the sample. On the other hand δW increases as the disorder gets stronger and it weakens the coupling between neighbouring blocks, thus favoring localization of the electronic wavefunctions.

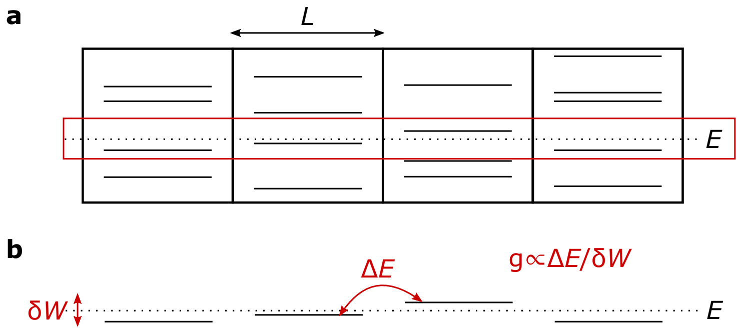

Figure 2.2 | Scheme of the basic idea of scaling theory. The conductance g of a large system can be deduced from the value of g of its elementary components of mesoscopic size L^d. $g(L)$ is measured by the ratio of the coupling to neighbouring blocks ΔE to the average distance of the energy levels δW. The value of g gives a measure of the disorder in the system, since it is small for large disorder and conversely.

The two situations briefly sketched here correspond to two limiting cases for the dependance of g on the system size L. The powerful intuition underlying scaling theory lies indeed here: the value of the conductance of the single L^d block provides a microscopic measure of disorder, being small if the disorder is strong and conversely; at the same time it also defines the scaling of g when the system size is increased from L^d to $(nL)^d$.

- In the first case, when the disorder is weak and the coupling between neighbouring blocks is good, the electron wave function is extended and nearly plane-wave like. The dependance of g on the size L is then provided by Ohm's law:

$$g(L) \propto L^{d-2} \tag{2.3}$$

- If the random potential is strong enough to dominate over the coupling to neighboring blocks, the electronic states are localized and the charge transport through the sample can only occur by an electron's hopping to an unoccupied state close in energy to the intial one. However, localized states close in energy are usually far apart in space, so that the hopping matrix element between them is exponentially small. In this regime the expected behavior for $g(L)$ is
$$g(L) \propto e^{-L/\xi} \tag{2.4}$$
where ξ is the localization length of the electronic wavefunction.

The key quantity that allows to catch all these scaling arguments at a glance is the scaling function $\beta(g)$, defined by the logarithmic derivative

$$\beta(g) = \frac{d\ln g}{d\ln L}. \tag{2.5}$$

It was indeed argued that this quantity is a function of the conductance g alone, which reflects the idea introduced above: the change of g when the size of the system increases from L to $L + \delta L$ is solely determined by its value at the previous length scale. The two limiting cases of Eqs. 2.3 and 2.4 obviously reflect in two limiting cases for $\beta(g)$:

- If $g > g_c$, where g_c is a certain critical value of the conductance, the system is a conductor. From Eq. 2.3 one derives
$$\beta(g) = d - 2. \tag{2.6}$$

- In the opposite case, when $g < g_c$, the electronic states are localized. We deduce from Eq. 2.4 that
$$\beta(g) = \ln(g/g_c) + c_d, \tag{2.7}$$
where c_d is a constant which depends on the dimensionality. In this case $\beta(g)$ is always negative, indicating that g decreases as L increases.

Under the assumptions that $\beta(g)$ is continuous and monotonic, the scaling curves of Fig. 2.3 are deduced from the two asymptotic behaviors just described, as a function of the dimensionality d.

In 3D, $\beta(g)$ cuts the zero axis at a critical point $\ln g_c$. If the disorder is weak such that on a certain length scale L the conductance $g(L) > g_c$, then $\beta(g(L)) > 0$ and when the size of the system increases, g increases too (the point moves right on the curve), and reaches the asymptotic behavior $\beta(g) = 1$, i.e. $g \propto L$. The system is therefore metallic at large scales. On the other hand, if the disorder is strong enough, on the length scale L one has $g(L) < g_c$. Then

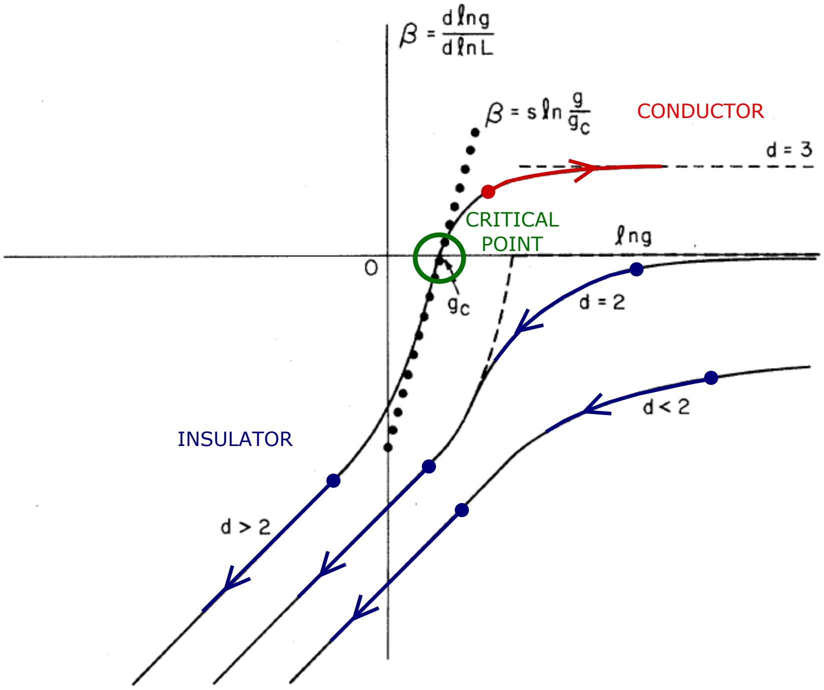

Figure 2.3 | **Scaling Theory of Localization.** Plot of the β-function versus $\ln(g)$ adapted from the original paper by the "gang of four" of 1979 [9]. For $d \leq 2$, $\beta(g)$ is always negative, indicating that the system is always localized. In higher dimensions, the system passes from an insulating phase, for $g < g_c$ to a conducting one. The critical point g_c, where β crosses zero and becomes positive, indicates the occurrence of the Anderson transition.

$\beta(g(L)) < 0$ and the point moves to the left when L increases, so that $g \to 0$. The system has an insulating behavior. The critical point g_c is therefore an unstable fixed point, while the metallic and insulating phases are stable. It is then found that the scaling theory predicts a metal-insulator transition in 3D. It also gives some predictions about the critical behavior [10]. Near the critical point one finds:

$$L_{loc} \propto (E_c - E)^{-\nu} \qquad \text{and} \qquad \sigma \propto (E - E_c)^s \tag{2.8}$$

where the critical exponents ν and s were found to be related by

$$s = (d-2)\nu. \tag{2.9}$$

For $d = 3$, one has $s = \nu$. Scaling theory does not provide any estimation of the exact value of the critical exponents. The most accurate estimations for them were later provided by numerical calculations of the Anderson model as I report in Sec. 2.2.2.

In 1D and 2D, $\beta(g)$ is always negative and therefore the conductance always flows to $g = 0$ when the size of the system increases. Scaling theory thus predicts that at low dimensionalities the system is always in the insulating regime.

The power of the scaling approach to AL lies in the fact that, starting from simple qualitative arguments, it could provide a first complete picture of the localization phenomenon and of its implications. It correctly predicted the different behaviors as a function of the dimensionality, detecting the presence of a critical point only for $d > 2$, and it defined the critical exponents at the transition.

Many of the predictions of the scaling theory have been later confirmed by a number of different theoretical approaches to the AL problem, as renormalization group calculations [12, 20], perturbation theory [2], self-consistent theory [21, 11], random matrix theory [13] and field-theory approaches [14, 15]. At the end of ths Section, I will report a test of the consistency between scaling and self-consistent theories, referring the readers to the cited references for an insight on the other theories.

2.2.2 Numerical simulations of the Anderson transition

Together with the attempt to find a suitable analytic formulation of localization, big efforts were performed in order to provide a quantitative description of the phenomenon using numerical calculations. The attention was mainly focused on the 3D case, which was clearly highlighted by scaling theory as the most interesting one, due to the presence of the transition.

Simulating the behavior of electrons according to the 3D Anderson model, numerical calculations proved to be very useful to locate the Anderson transition and to characterize the critical behavior close to it. The early results confirmed the predictions of scaling theory as it is shown in Fig. 2.4. The scaling function $\beta(g)$ switches from positive to negative, crossing zero for a critical value of the conductance. Besides confirming the existence of the two regimes, these results show that $\beta(g)$ behaves smoothly across the transition, which is a proof that the Anderson transition is a continuous phase transition of second-order.

Another important contribution coming from numerical results is the calculation of the critical exponents at the transition. The best current estimate for 3D systems is $s = \nu = 1.58 \pm 0.01$ [17, 10].

Finally, I report those results that can be seen as the first analogous of the main result of this thesis, i.e. the determination of the mobility edge trajectory in the disorder-energy plane. This has been the subject of a number of works that have brought to a clear assessment of the mobility edge in the Anderson model [10]. I report in Fig. 2.5 the latest results from [18], which show the calculated critical point for the Anderson transition as a function of the disorder strength W and of the energy E.

This brief overlook about the earlier outcomes of numerical simulations on electronic systems has just the purpose to prove the validity of this tool to provide quantitive results close to the transition. Since the time of the calculations reported here, computation techniques have greatly improved and a number of interesting results have been obtained, also from simulations on physical systems different from electrons in disordered lattices. I will take over this discussion

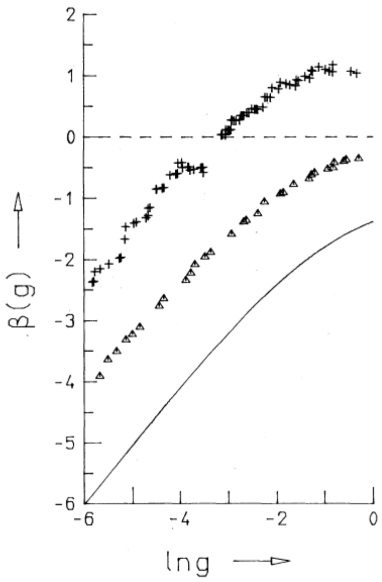

Figure 2.4 | Numerical calculation of the scaling function $\beta(g)$ for the 3D Anderson model. The solid line is for $d = 1$, the triangles for $d = 2$ and the crosses for $d = 3$. The results reported here perfectly match with the expected behavior of Fig. 2.3. The figure is taken from [16].

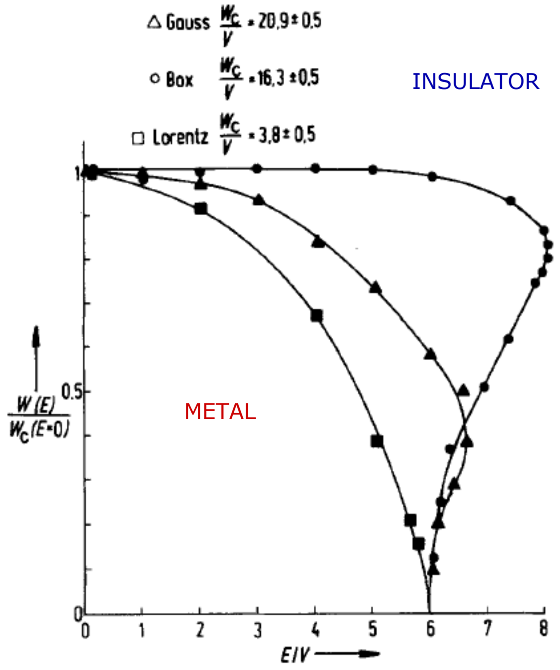

Figure 2.5 | Phase diagram for the 3D Anderson model. The mobility edge trajectories $W_c(E)$ are calculated for the 3D Anderson model, considering different probability distributions of the on-site energies. Below the mobility edge is the metallic phase, above it the insulating one. The figure is adapted from [18].

at the end of Chapter 5, when comparing our experimental results with the most advanced calculations relative to ultracold atomic systems.

2.2.3 Self-consistent theory of localization

Up to the 1980s a genuine microscopic theory for AL was still missing. The metallic/insulating regimes identified by scaling theory were still lacking a physical explanation on the microscopic scale. Realizing that all the efforts to develop an exact theory of the phenomenon ended up to fail, D. Vollhardt and P. Wölfle decided to consider an approximation scheme [21]. They developed a theoretical tool which, starting from an analytical description of the system, keeps trace of all its specific microscopic properties, but accounts approximately for the critical behavior at the transition. The main advantage of this strategy lies in its versatility, since it can be applied to every kind of disordered system, provided few basic conditions are complied with. On the other hand, the main drawback in this scheme is its perturbative nature: most results are obtained from an expansion in powers of the disorder, hence valid only for small enough potential strength. This means that suitable strategies needs to be found to extend its validity close to the localization transition, where the disorder is necessarily strong.

The formulation of the so-called *self-consistent theory* (SC theory) of localization by Vollhardt and Wölfle certainly made a great contribution in the understanding of AL, since it first shed light on the microscopic origin of the phenomenon and provided a helpful theoretical tool for the comparison with experimental results. For these reasons, it worth to spend some time to introduce the basic ideas about the theoretical approach they proposed and its main results [22]. This is especially interesting in the context of this thesis because many of the theoretical results we can compare with are developped in the form of SC theory, so that a basic knowledge of this formalism is of fundamental importance.

Diagrammatic perturbation theory

The point of the game is to draw a description for the quantum transport of a particle in a disordered medium. The language used is that of a *diagrammatic perturbation theory* in the disordered potential. The starting point is a Hamiltonian of the form

$$H = H_0 + V, \tag{2.10}$$

where H_0 describes regular propagation in an ordered structure and V is the disordered potential. The simplest example described by this kind of Hamiltonian is that of a single quantum particle in an external potential: $H = p^2/2m + V(r)$.

Assuming that H_0 is translation-invariant, we can write the equivalent of Eq. 2.10 in Fourier space:

$$H = \sum_k \varepsilon_k^0 a_k^\dagger a_k + \sum_{k,q} V_q a_{k+q}^\dagger a_k, \tag{2.11}$$

where k are the wave vectors used to label the eigenstates of H_0, a_k and $a_k^\dagger$ are the annihilation and creation operators, ε_k^0 is the free dispersion relation ($\varepsilon_k^0 = \hbar^2 k^2/2m$ for matter waves) and V_q is the scattering amplitude, given by the Fourier component of the potential: $V_q = \langle k+q|V|k\rangle$.

A simple representation of V_q is provided by the Feynman diagram:

$$V_q = \qquad (2.12)$$

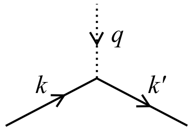

In Eq. 2.11 we can immediately note that the formalism we are introducing here is of general validity for every kind of system, provided one knows the appropriate free dispersion relation ε_k^0 and the scattering potential V_q. As we will see in the following, SC theory has been successfully used in the case of electrons, but also of classical waves and ultracold atoms.

The basic tool I need to introduce here is the *Green function* for the single-particle Hamiltonian, which is the appropriate quantity to describe the time evolution of a state $|\psi\rangle$ according to the Schrödinger equation $i\hbar\partial_t|\psi\rangle = H|\psi\rangle$. The forward-time evolution operator is thus provided by the retarded Green function $G^R(t) = -\frac{i}{\hbar}\theta(t)\exp(-iHt/\hbar)$, which is the solution for the differential equation

$$[i\hbar\partial_t - H]G^R(t) = \delta(t). \qquad (2.13)$$

It is usually more comfortable to work in the Fourier space, going from time to energy domain:

$$G^R(E) = \lim_{\eta\to0^+}\int dt e^{i(E+i\eta)t/\hbar}G^R(t) = \lim_{\eta\to0^+}\frac{1}{E-H+i\eta} =: \frac{1}{E-H+i0}. \qquad (2.14)$$

In the basis where H is diagonal, $G^R(E)$ is diagonal too, so that one can write the spectral decomposition $G(E) = \sum_n |n\rangle(E-\varepsilon_n)^{-1}\langle n|$, where $|n\rangle$ are the eigenstates of H. The matrix elements of $G^R(E)$ are the so-called "propagators". As an example, we can write a propagator in the position representation $\langle r|n\rangle = \psi_n(r)$:

$$G^R(r,r';E) = \langle r'|G^R(E)|r\rangle = \sum_n \frac{\psi_n(r')\psi_n^*(r)}{E-\varepsilon_n+i0} = r \longrightarrow r' \qquad (2.15)$$

The propagator is a crucial quantity since it contains precious information: its singularities on the real axis correspond to the spectrum of H, thus encoding all the possible evolution frequencies, while the residues at these poles provide information about the corresponding eigenfunctions.

We cannot write down analytically the propagators for H, due to the presence of the disorder term V. Then we start drawing the announced perturbation scheme. We write the Green function for the free Hamiltonian H_0, using the momentum representation where H_0 is diagonal:

$$G_0^R(k;E) = \frac{1}{E-\varepsilon_k^0+i0} = \underset{k}{\longrightarrow} \qquad (2.16)$$

Then we insert the perturbation due to V. Being $G(E) = [E-H_0-V]^{-1} = [(E-H_0)(1-(E-H_0)^{-1}V)]^{-1}$, we can write the Born series in powers of V:

$$G(E) = [1-G_0V]^{-1}G_0 = G_0 + G_0VG_0 + G_0VG_0VG_0 + ... \qquad (2.17)$$

It is useful to write down the propagators $\langle k'|G(E)|k\rangle$ using the graphical representation of Feynman diagrams:

$$\langle k'|G(E)|k\rangle = \delta_{kk'}$$

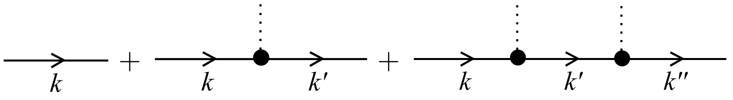

$+ \ldots$ (2.18)

Since we are dealing with a disordered potential, we are not interested in the evaluation of the propagators for each different realization of the potential, but we want to calculate suitable expectation values. We need therefore to perform the *ensemble average* of the above quantities over the disorder distribution. The potential $V(r)$ is completely characterized by its correlation functions $\langle V_1\rangle$, $\langle V_1V_2\rangle$, $\langle V_1V_2V_3\rangle$, etc., where $V_i = V(r_i)$ and the brackets $\langle\cdot\rangle$ represent the ensemble average. We assume that $V(r)$ is statistically homogeneous, so that the correlation functions only depend on the distance $r_{ij} = r_i - r_j$. We define the following correlation functions:

$$\langle V_1\rangle = \langle V\rangle \tag{2.19}$$

$$\langle V_1V_2\rangle = P(r_{12}) = \tag{2.20}$$

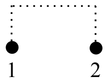

$$\langle V_1V_2V_3\rangle = T(r_{12}, r_{23}) = \tag{2.21}$$

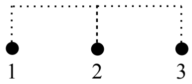

and so on for arbitrary n-point correlation functions. One may always take $\langle V\rangle = 0$ by defining a centered potential $V \mapsto V - \langle V\rangle$, while redefining the zero of energy $E - \langle V\rangle \mapsto E$. In Fourier representation the correlation functions above become:

$$P(q) =$$

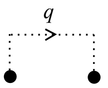

$$, \quad T(q, q') =$$

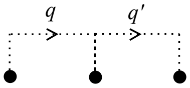

$$, \quad \text{etc.} \tag{2.22}$$

The specific form of these general correlation functions depends on the type of disorder in the system.

Now that we have defined the correlation functions of the disorder, we can go back to the problem of writing the ensemble average of the single-particle propagator in Eq. 2.18. We find:

$$\langle G\rangle = G_0 + G_0\langle VG_0V\rangle G_0 + G_0\langle VG_0VG_0V\rangle G_0 + \ldots \tag{2.23}$$

or equivalently

$$\langle G\rangle =$$

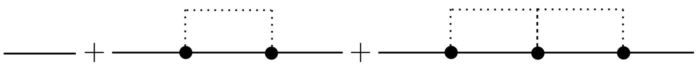

$+ \ldots$ (2.24)

Another quantity typical of diagrammatic expansions comes now to our aid. It is the *self-energy* $\Sigma(E)$, which is defined by the Dyson equation:

$$\langle G\rangle = G_0 + G_0\Sigma\langle G\rangle. \tag{2.25}$$

It worth here to briefly comment about the information encoded in $\Sigma(E)$ and on its physical meaning. By iterating the Dyson equation in Eq. 2.25, one finds that the average propagator $\langle G\rangle$ expands as

$$\langle G\rangle = \rule[0.5ex]{2em}{0.4pt} + \rule[0.5ex]{2em}{0.4pt}\textcircled{Σ}\rule[0.5ex]{2em}{0.4pt} + \rule[0.5ex]{2em}{0.4pt}\textcircled{Σ}\rule[0.5ex]{2em}{0.4pt}\textcircled{Σ}\rule[0.5ex]{2em}{0.4pt} + ... \tag{2.26}$$

It is visible here that the self-energy contains exactly all disorder correlations that cannot be completely factorized by removing a free propagator G_0 in between. These non-factorizable terms are called “one-particle irreducible”. Moreover, the self-energy contains only the correlations and internal propagators, but all the external propagator lines are removed. This makes the self-energy the simplest object describing all relevant disorder correlations.

Let us try to understand which is the physical meaning of $\Sigma(E)$. We can rewrite the Dyson equation and solve it formally for the average operator: $\langle G\rangle = [1 - G_0\Sigma]^{-1}G_0 = [G_0^{-1} - \Sigma]^{-1}$. Its matrix elements are:

$$\langle G^R(k,E)\rangle = \frac{1}{E - \varepsilon_k^0 - \Sigma(k,E)}. \tag{2.27}$$

Comparing it with Eq. 2.16, we recognize that the self-energy effectively modifies the free dispersion relation. Generally, $\Sigma(E)$ is a complex quantity with a real and an imaginary part. The modified dispersion relation coming from Eq. 2.27

$$E_k = \varepsilon_k^0 + \mathrm{Re}\Sigma(k, E_k) \tag{2.28}$$

is an implicit equation for the new eigen-energy E_k of the mode k. So one effect of the disorder is to shift the energy levels. But plane waves with fixed k are no longer proper eigenstates of the disordered system. This is encoded in the imaginary part of $\Sigma(E)$. We define $\Gamma_k = -2\mathrm{Im}\Sigma(k, E_k)$. The *spectral density* is then

$$A(k,E) = -2\mathrm{Im}\langle G^R(k,E)\rangle = \frac{\Gamma_k}{(E - E_k)^2 + \Gamma_k^2/4}. \tag{2.29}$$

The spectral function is the probability density that an excitation k has energy E. The integral over k therefore gives the average density of states per unit volume:

$$N(E) = \frac{1}{2\pi}\int \frac{d^dk}{(2\pi)^d} A(k,E). \tag{2.30}$$

Comparing Eq. 2.29 with the spectral function for the free Hamiltonian $A_0(k,E) = 2\pi\delta(E - \varepsilon_k^0)$, one recognizes that the disorder introduces a finite spectral width Γ_k, which implies a finite lifetime $\hbar\Gamma_k^{-1}$. The finite lifetime translates in turn into a finite *scattering mean free path* l_s for the spatial matrix elements of the average propagator:

$$\langle G(r - r', E)\rangle = \int \frac{d^dk}{(2\pi)^d} e^{ik\cdot(r-r')}\langle G(k,E)\rangle = G_0(r - r', E)e^{-|r'-r|/2l_s}, \tag{2.31}$$

showing an exponential decay with $l_s = k\Gamma_k/(2E)$ evaluated at $k = \sqrt{2mE}/\hbar$.

Now that we have introduced most of the relevant tools for our perturbation theory, we start to approach the heart of the problem. The relevant quantity to describe the transport of a quantum particle is the density $n(r,t)$. In the case of our disordered system, we consider the ensemble-averaged density $n(r,t) = \langle\langle r|\rho(t)|r\rangle\rangle$ in the long-time limit. This is indeed the quantity that tells us if the particle is able to spread all over the space or it is confined to a limited region and thus localized. Substituting the time evolution operators with the corresponding Green functions, one finds that the relevant quantity to be calculated is the *average intensity propagator* $\langle G^A(E)G^R(E')\rangle$, where $G^A(E)$ is the advanced Green function corresponding to the backward-time evolution. In analogy to the Dyson equation for the average single-particle propagator (Eq. 2.25), one can write a structurally similar equation for the intensity propagator $\Phi = \langle G^A G^R\rangle$, known as the Bethe-Salpeter equation:

$$\Phi = \langle G^A\rangle\langle G^R\rangle + \langle G^A\rangle\langle G^R\rangle U\Phi, \tag{2.32}$$

where the idea is to separate the evolution with the uncorrelated average amplitudes

$$\langle G^R(k,E)\rangle\langle G^A(k',E')\rangle = \tag{2.33}$$

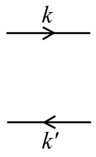

from all the scattering events that couple these amplitudes. All these terms are contained in the *intensity scattering operator U*. Its detailed form again depends on the model of disorder. In all cases, $U_{kk'}(E)$ is essentially the differential cross-section for scattering from k to k' and has the following structure:

$$U(k,k';E) = \tag{2.34}$$

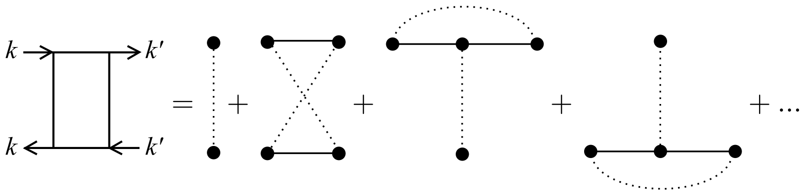

From linear response theory one can see that this scattering vertex allow to calculate the *transport mean free path l*, in close analogy to the calculation of the scattering mean free path l_s from the self-energy. The ratio between the two length scales is found to be

$$\frac{l_s}{l} = 1 - \langle\cos(\theta)\rangle_U \tag{2.35}$$

where θ is the scattering angle between k and k', and the brackets $\langle\cdot\rangle_U$ indicate an average over the scattering cross-section U. The physical interpretation of the two length scales l and l_s is the following: the scattering mean free path l_s measures the distance over which the particle loses memory of its initial phase; the transport mean free path l is instead the distance over which the direction of propagation is randomized.

Here we are at the final crucial step. We need a quantity that allows to catch the macroscopic transport properties of a system, i.e. to characterize the expansion of $n(r,t)$. Let us consider the generic behavior that one may expect for transport in a disordered environment, that is *diffusion*. Diffusive transport derives from two very basic hypotheses: 1) the local conservation law $\partial_t n + \nabla \cdot j = s$, with $j(r,t)$ the current density associated with $n(r,t)$ and $s(r,t)$ the source function; 2) the linear response $j = -D\nabla n$, saying that a density gradient induces a current to reestablish global equilibrium. The *diffusion constant* D is thus defined as a linear response coefficient. As immediate consequence of these two conditions, we find the diffusion equation:

$$[\partial_t - D\nabla^2]n(r,t) = s(r,t). \tag{2.36}$$

The solution for a unit source $s(r,t) = \delta(r)\delta(t)$ is provided in the Fourier space by the Green function of this problem (also called density relaxation kernel)

$$\Phi_0(q,\omega) = \frac{1}{-i\omega + Dq^2}. \tag{2.37}$$

By Fourier transforming, one finds that in real space and time

$$\Phi_0(r,t) = \theta(t)(4\pi Dt)^{-d/2}\exp(-r^2/4Dt). \tag{2.38}$$

The relaxation kernel $\Phi_0(r,t)$ then describes diffusive spreading with $\langle r^2\rangle = 2dDt$.

We have then seen how the description of the dynamics on large distances and for long times is defined by the diffusion constant D. What we only need to access the transport properties of the system is then a microscopic theory to calculate D. The idea of SC theory of localization is to use the diagrammatic perturbation theory presented so far to predict the value of D. In the following I report how, by taking into consideration the intensity scattering operator U at different perturbative orders (Eq. 2.34), one can reconstruct classical diffusion and weak localization, and finally get closer to the Anderson transition for strong disorder by implementing a self-consistency scheme.

Diffusion

The first order contribution to U in Eq. 2.34 describes a single-scattering process. We switch to the real space representation in order to better identify the scattering process encoded in it. The conversion is as follows: we draw a full line for every amplitue ψ propagated by G^R (upper lines in 2.34) and a dashed line for every ψ^* propagated by G^A (lower lines). Impurities are represented by black dots.

$$U_B :$$

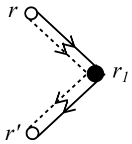

(2.39)

This process is insensitive to phase variations and could just as well take place for classical particles. So this Boltzmann contribution U_B describes classical diffusion with diffusion constant

$$D_B = \frac{vl_B}{d} \tag{2.40}$$

The Boltzmann transport mean free path is calculated by inserting U_B in Eq. 2.35. Depending on the microscopic scattering process, l_B can be longer than l_s, if forward scattering is dominant (this is for example the case for matter waves in spatially correlated potentials), or, in the case of isotropic scattering, one finds $l_s = l_B$.

In this first simple case we have verified that the perturbation theory developed above allows to calculate l_s and thus D_B in the Boltzmann approximation, i.e. to the first perturbative order, using only micorscopic ingredients: the dispersion relation in free space and the correlation function of the scattering potential.

Weak localization

The first corrections to the classical scattering process U_B shown in Eq. 2.34 involve one or more scatterer and several possibilities of intermediate propagation. The most well-known type of correction stems from the diagram with two crossed lines. In real space, the scattering process is

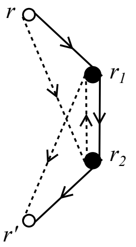

(2.41)

Here interference comes into play, due to a phase shift $\Delta\phi$ between ψ and ψ^*, that depends on the positions of the impurities r_1 and r_2. Contributions of this type are ensemble-averaged to zero, apart from those where $r = r'$. In this case the phase shift picked up by the two counter-propagating amplitudes goes to zero:

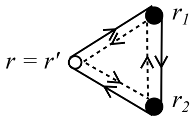

(2.42)

The vanishing phase difference implies constructive interference and therefore enhanced probability to stay at the original position. This holds true for every closed loop, no matter how many scatterers are visited on the path. One can then consider all maximally crossed diagrams:

$U_C =$ 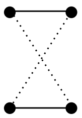 $+$ 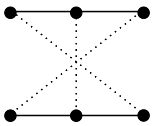 $+ \ldots$ (2.43)

This class of diagrams is usually known with the name of *Cooperon* contribution. This contribution is peaked around backscattering $k = -k'$. One can now introduce a further approximation, considering that the propagation between successive scattering events is purely diffusive, and sum up all contributions with the help of the diffusive kernel in Eq. 2.37 to calculate the corrected diffusion constant. The weak localization correction is found as

$$\frac{1}{D} = \frac{1}{D_B}\left[1 + \frac{1}{\pi N_0 D_B}\int \frac{d^d q}{(2\pi)^d}\frac{1}{q^2 - i0}\right] \tag{2.44}$$

where N_0 is the free density of states. The quantum correction coming from constructive interference in the closed scattering loops (Cooperon contribution) makes $D < D_B$, thus providing the microscopic reason for the so-called *weak localization*.

We consider the $d = 3$ case and matter waves with dispersion relation $\varepsilon = \hbar^2 k^2/2m$. Considering that the Cooperon is isotropic, we can rework Eq. 2.44 and obtain

$$\frac{1}{D} = \frac{1}{D_B}\left(1 + \frac{\hbar}{\pi m k D_B}\int_0^\infty \frac{q^2}{q^2 - i0}dq\right). \tag{2.45}$$

Evaluating the integral with a large-q cutoff at $1/l$, we find:

$$D \approx D_B\left(1 - \frac{3}{\pi (kl)^2}\right). \tag{2.46}$$

The correction found here scales as $1/(kl)^2$. However, this is not the whole story, since other diagrams, not included in U_C, give contributions that are actually more important for small disorder $kl \gg 1$.

From Eq. 2.46 one can derive an approximate criterion for the onset of Anderson localization, since $D \to 0$ when $(kl)_c = O(1)$. This is the well-known *Ioffe-Regel criterion* for localization. However, the precise calculation of the critical point is a delicate task, requiring to go further the simple lowest-order perturbations considered so far.

Self-consistent theory: towards the Anderson transition

The study of weak localization certainly helped us to focus how diffusive transport is affected by interference. However, weak localization is essentially a perturbative result: first, because the Cooperon contribution is evaluated considering diffusive propagation, which is strictly valid only in the absence of interference; second, because this simple approach takes into account only a specific type of diagrams. A weak-disorder perturbation theory in powers of $1/kl$ alone would never be able to describe the Anderson transition in 3D for strong disorder, nor the crossover from weak to strong localization in 1D and 2D.

The self-consistent theory of localization developed by Vollhardt and Wölfle [21] is an attempt to go further this first basic approximation, by applying a suitable self-consistency scheme, as often employed with success to describe phase transitions in statistical physics. Rather then a theory with controlled approximations, it can be thought of as a guess about the most important contributions of diagrams to all orders.

The basic observation is that the diffusive contribution of large closed loops considered in U_C must itself be modified by weak localization: inside a large loop the wave explores smaller loops, leading to a decreased diffusion constant for propagation along the large loop. This argument can be repeated, so that one comes to consider loops within loops within loops..., all the way down to the smallest loops, stopping at the scale of the transport mean free path l.

The simplest idea to implement this is to replace the Boltzmann diffusion constant D_B in Eq. 2.45 with the renormalized diffusion constant D itself, thus generating an implicit equation for D. It turns out that this is not enough, since the single quantity D cannot describe the full dynamics of the particle both for short times, where it is diffusive, and for long times where localization may eventually set in. So the idea is to use a scale-dependent diffusion constant, and it turns out that it is simpler to consider a dependence on the time scale rather than on the spatial one. We thus consider a diffusion constant $D(\omega)$ which depends on frequency ω. The self-consistent expression for $D(\omega)$ is then derived from Eq. 2.45 replacing D_B with $D(\omega)$ and reintroducing the ω dependance:

$$D(\omega) + \frac{\hbar}{\pi m k} \int \frac{q}{q^2 - (i\omega/D(\omega))} dq = D_B. \tag{2.47}$$

In the short-time limit $\omega \to \infty$, one gets back to classical Boltzmann diffusive propagation, as expected. The most interesting part takes place at long times, in the limit $\omega \to 0$. The implicit equation for $D(\omega)/D_B$ has different solutions depending on the value of kl:

- if $kl < (kl)_c = \sqrt{3/\pi}$, D/D_B tends to a finite value as $\omega \to 0$. This means that the system is in a diffusive regime, but the diffusion constant is reduced with respect to the classical one.

- if $kl > (kl)_c$, the ratio $D/D_B \to 0$ when $\omega \to 0$, which means that diffusive transport is inhibited. More precisely, one finds an exponential localization:

  $$D(\omega) \approx -i\omega\xi_{loc}^2 \quad \text{with} \quad \xi_{loc} \sim \frac{1}{(kl)_c - kl} \tag{2.48}$$

  immediately below the transition point, on the insulating side. This means that the critical exponent predicted by SC theory is $\nu = 1$, thus different from $\nu = 1.58$ found in numerical simulations. The reason lies in the approximate character of the self-consistent approach, which cannot account for the large fluctuations close to the transition.

- at the critical point $kl = (kl)_c$, one find $D(\omega) \sim (-i\omega)^{1/3}$. As a consequence, the critical behavior is anomalous diffusion: $\langle r^2(t)\rangle \propto t^{2/3}$.

Early results of self-consistent theory

It is intrinsic to the perturbative nature of this theory that its results may be not quantitatively accurate close to the transition. For this reason it is of fundamental interest to compare its predictions to other reliable results coming from numerics, experiments or controlled theoretical models. I report here two notable examples which contributed to prove the reliability of SC theory under certain circumstances.

The first one is a check of the consistency of self-consistent theory results with the predictions of the scaling theory. In particular, they derived the β-function introduced in Sec. 2.2.1 from the self-consistent equation for the diffusion coefficient [23]. The results for different values of d are reported in Fig. 2.6. The visible agreement of the curves obtained here with the ones of Fig. 2.3 indicates that, when combining scaling arguments with the microscopic description from SC theory, one gets the same behavior of the system deduced from more qualitative arguments. This first test thus proves that self-consistent theory is able to reproduce the relevant physical properties of the disordered systems under consideration.

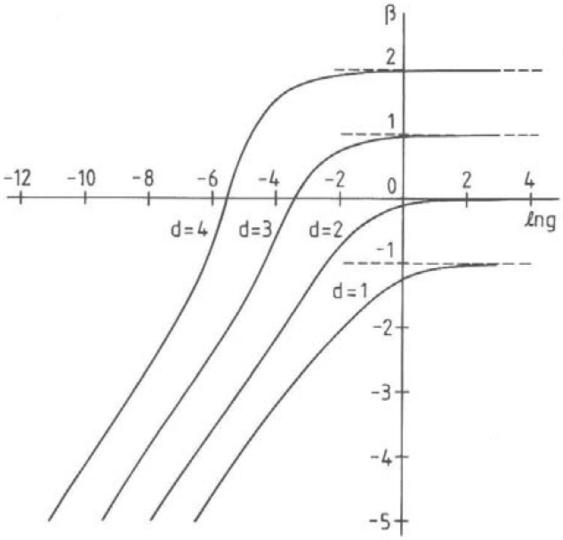

Figure 2.6 | Consistency of self-consistent and scaling theories. The scaling function $\beta(g)$ is calculated starting from the microscopic description of SC theory. The result perfectly matches with the predictions of scaling theory that were based on qualitative arguments, insensitive to the microscopic details of the system. Figure from [23].

A second test consists in the comparison with numerical results for the mobility edge. The same data reported in Fig. 2.5 from [18] are considered. The analytic expression for the phase boundary separating localized and extended states has been derived using the SC theory applied to the same Anderson model used in the numerical simulations. The results are shown in Fig. 2.7: the agreement is seen to be very good.

In conclusion, we can say that the contribution of self-consistent theory is to provide a versatile tool to investigate problems related to transport in disordered media. Its specific merit with respect to pre-existing theoretical approaches is the possibility to incorporate the detailed characteristics of the system under consideration.

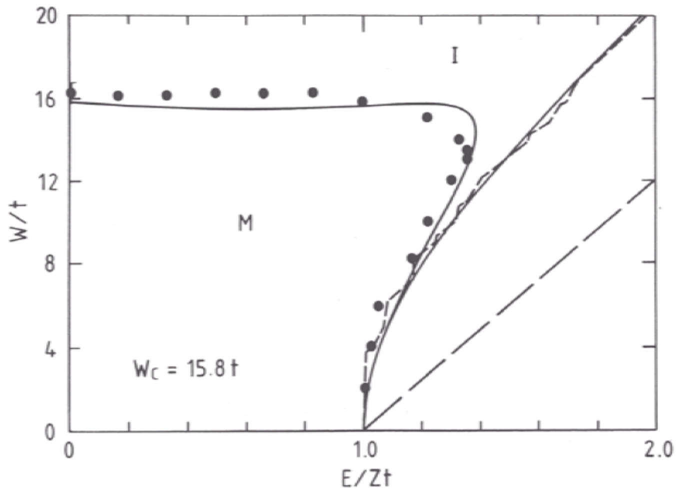

Figure 2.7 | **Numerical and analytical results for the mobility edge in disordered cubic lattice.** The phase diagram showing the metallic (M) and insulating (I) regimes in the tight-binding model with on-site disordered energies is reported. Black dots are the numerical results, while the solid line comes from self-consistent theory. The other lines are bounds on the energy spectrum. Figure from [21].

2.3 Experimental investigation of the Anderson transition

2.3.1 Solid state systems

In parallel to theory and numerical simulations, experiments on solid-state systems have tried to observe and characterize the Anderson transition. A notable example are those performed on doped semiconductors, where the amount of disorder and the electronic concentration can be varied within certain ranges. Although a localization transition could be detected unambiguously, the comparison with theory is quite hard. The reason is that in real electronic systems the Coulomb interaction plays a major role and definitely changes the localization problem with respect to the single-electron Anderson picture.

Figure 2.8 shows the experimental mesurement of the conductivity in a Si-doped AlGaAs crystal as a function of the electron concentration n, which in this case essentially represents the electronic Fermi energy [19]. A clear metal-insulator transition is observed, since the conductivity is flat around zero for small values of n and at a certain critical value it rises to finite values, increasing linearly with n. The linear behavior of conductivity above the transition point indicates a significant deviation from the theoretical predictions about AL. The linear scaling is indeed compatible with a critical exponent $\nu \approx 1$, which is different from the exponent of the pure Anderson transition $\nu = 1.58$, indicating that interaction effects are probably important.

2.3.2 Classical waves

Despite all the intial interest concerning AL was addressed to the problem of disorder in electronic systems, as it became clear that the role of Coulomb interactions could not be neglected, the

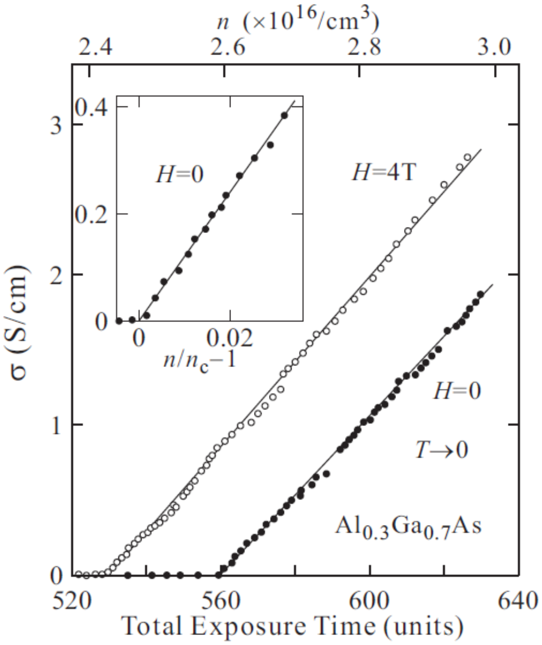

Figure 2.8 | Localization transition in doped semiconductors. The conductivity σ is measured for a Si-doped AlGaAs crystal as a function of the electron concentration n. The linear increase of σ take off at a certain critical value of n, indicating the occurrence of the Anderson transition. The figure is adapted from [19].

question about other physical systems where the pure AL could be observed started to be raised. The idea was certainly supported by the formulation of self-consistent theory, which, clarifying the microscopic mechanism at the basis of AL, pointed out that it was not at all specific of electronic systems. It was indeed clear that the formulation of self-consistent theory could be similarly applied both to the case of the Schrödinger equation for quantum particles

$$\left(-\frac{\hbar^2}{2m}\nabla^2 + V(\mathbf{r}) - E\right)\psi(\mathbf{r}) = 0 \tag{2.49}$$

or to the wave equation for classical monochromatic waves of frequency ω

$$\left(\frac{\omega^2}{c^2(\mathbf{r})} + \nabla^2\right)\psi(\mathbf{r}) = 0, \tag{2.50}$$

where $c(\mathbf{r})$ is the wave velocity at position $\mathbf{r}$ in an inhomogeneous medium, assumed to be a randomly fluctuating quantity. The main difference between Eqs. 2.49 and 2.50 is that in the latter the random potential $1/c^2(\mathbf{r})$ is multiplied by ω^2, so that disorder is suppressed in the limit $\omega \to 0$. By constrast, in the quantum case disorder will be dominant in the limit of low energy E. Apart from this and few minor details, the physics of non-interacting quantum wave packets and classical wave packets is exactly the same.

The great advantage related to classical waves is that they are intrinsically non interacting. Furthermore, they are usually easy to control at room temperatures and they allow to access other physical quantities, in addition to conductance, which are also influenced by the occurrence of localization, as fluctuations in the field amplitude or long-range correlations. The role of energy as the critical parameter to distinguish between localized and extended states is here taken over by frequency. The main drawback in using classical waves is that they do not localize at small frequencies, so that the experimental conditions where to look for AL have to be carefully chosen.

The typical strategy used to detect the occurrence of AL for classical waves is to study how the transmission of an incoming wave scales with the system size. In the diffusive regime the intensity of the output signal is expected to scale linearly with the thickness of the medium, while, in the localized regime, transmission should decay exponentially with the length. Particular attention has to be paid to the possibility of absorption in the medium. In the strong scattering regime where AL occurs, absorption effects are usually strong. The problem concerning the presence of absorption is mainly due to the fact that it also manifests as an exponential decay of the output signal with the system size. One then needs to carefully distinguish the two phenomena in order to unambiguously detect AL.

Starting from the 1990s several experiments trying to detect AL were performed on a rich variety of systems, ranging from light, microwaves, ultrasound and photonic crystals. Here I will only present the results of our interest, i.e. the one concerning the Anderson transition in 3D systems, referring to [24, 25] for a review about the broader context of AL in classical waves.

Detection of the Anderson transition

The detection of the Anderson transition with classical waves hails back to a fairly recent past. The two experiments I briefly report here have had the great merit to report the first unambiguous observation of pure Anderson transitions. The physical systems employed are ultrasound and light.

In order to study the localization of *ultrasound*, in 2008 J. Page, S. Skipetrov and coworkers employed a 3D elastic network of aluminum beads [26]. At the entrance of the sample they placed a point-like source of ultrasound energy and they measured the expansion of the elastic energy in the transverse directions. In diffusive samples the expansion would be proportional to the square root of time, so that the observation of a transverse confinement of the elastic energy is the clear signature of sound localization. In Fig. 2.9 is reported the measurement of the transverse expansion, where a clear deviation from the diffusive behavior can be seen: the data do not follow the linear increase indicated by the dashed lines but apparently tend to a saturation at large time. The results are well interpreted by making use of the self-consistent theory, adapted to the specific parameters of the experimental system. Thanks to comparison with the theoretical model, the authors were able not only to detect the existence of a localized regime, but also to deduce the critical parameters of the transition, i.e. the specific value of $(kl)_c$ at which localization occurs.

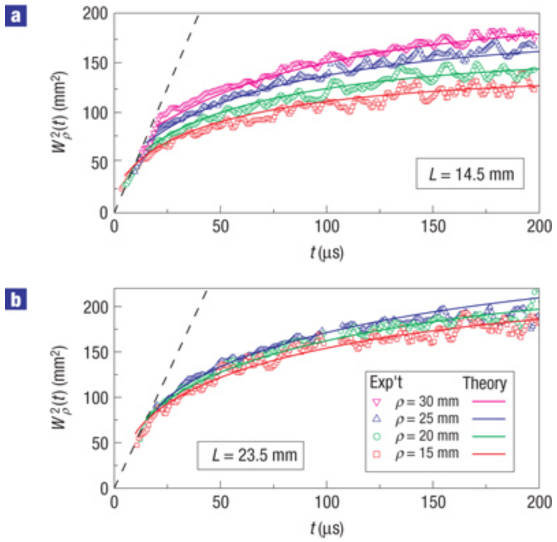

Figure 2.9 | **Transverse localization of ultrasound in a 3D disordered medium.** Time evolution of the squared width $w_p^2(t)$ of the transmitted intensity for two different values of the thickness L of the sample. Different colors correspond to different transverse displacements of the detector. The curves clearly deviate from the diffusive linear behavior represented by the dashed lines, which indicates the occurrence of localization.

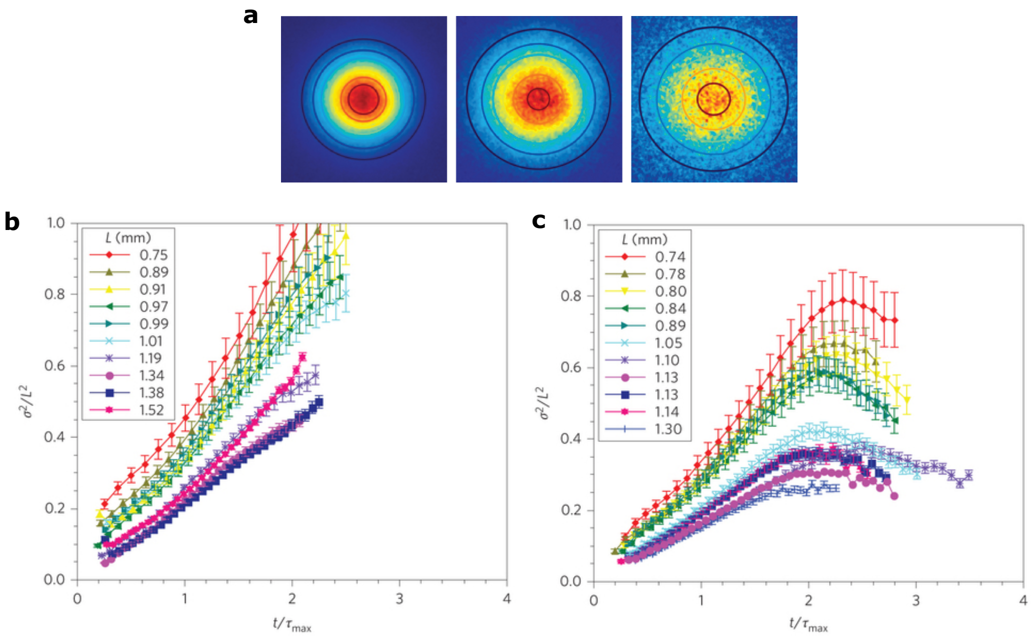

Figure 2.10 | **Evidence of localization of light in a 3D disordered medium.** In **a** are reported the raw data for the transmitted light in a high turbidity sample at three different times (time increases from left to right). The contours displaying the fit of the intensity distributions help to notice that the width increases from the first to the second image, but remains constant from the second to the third. This is even more clear when looking at the plot in **c**, where, after an initial increase of σ^2 with time, the width apparently saturates to a finite value, differently from what happens in **b** for a sample with lower turbidity. The different colors in **b** and **c** correspond to different slab thicknesses. The figures are adapted from [27].

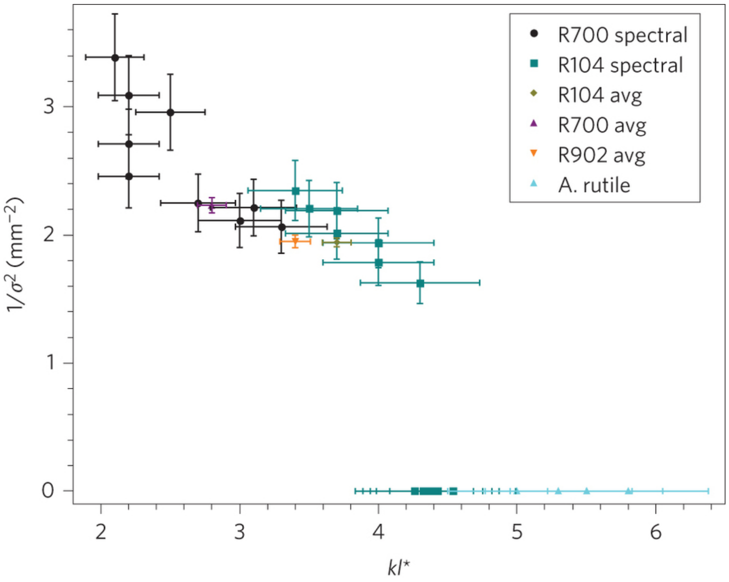

Figure 2.11 | Anderson transition for light. The inverse of the squared localization length is plotted versus the turbity for different samples. The sudden drop of $1/\sigma^2$ to zero around $kl \approx 4.5$ indicates the transition to localization.

The experiment reporting 3D AL of *light* was performed in 2013 by the group of G. Maret [27]. There they studied the transmission of light in 3D open, highly scattering TiO_2 powders. In order to study the dependance of the transport properties of light on the amount of disorder in the system, they vary the turbidity kl of the sample and the slab thickness. Measuring the width of the transmitted light σ as a function of time (similarly to the the case of ultrasound reported above), they observe how the system switches from diffusive to localized as the turbidity is increased (Fig. 2.10). The signature of localization is again the deviation from the diffusive linear behavior and the appearance of a plateau in the time evolution of the squared width.

The saturation value of σ is taken as the localization length. In Fig. 2.11 they report the inverse of the localization length as a function of kl, where one can clearly detect the occurence of the Anderson transition around $(kl)_c \simeq 4.5$, as the localization length diverges.

For completeness I have to mention that some doubts have been raised about the validity of these results, concerning the role of inelastic scattering in the system. For a discussion about this one can refer to [28, 29].

2.3.3 Ultracold atoms

With the advent of laser cooling of atoms, a new type of system to study AL has appeared on the scene. Since the time of the first BECs in 1995, ultracold atoms had proved to be an optimum tool to investigate open problems related to quantum systems. For this reason they immediately appeared an extremely appealing context where AL could be studied under well controlled conditions.

Localization in momentum-space

The first experimental investigation of AL with ultracold atoms was performed achieving localization in momentum space. The idea is to have atoms placed in an optical lattice, which is modulated in time to produce a quasi-random potential. This is realized by using a train of short pulses and an additional sine function of incommensurate frequency. This system is known as the *quasi-periodic atomic kicked rotor* and realizes a momentum-space analogue of the Anderson Hamiltonian. The advantage coming from the fact that the measurements are taken in momentum-space is that one can use very diluted samples, where interactions do not matter. Changing the number of modulating frequencies it is possible to study AL from 1D to 3D or even in higher dimensions [30, 31].

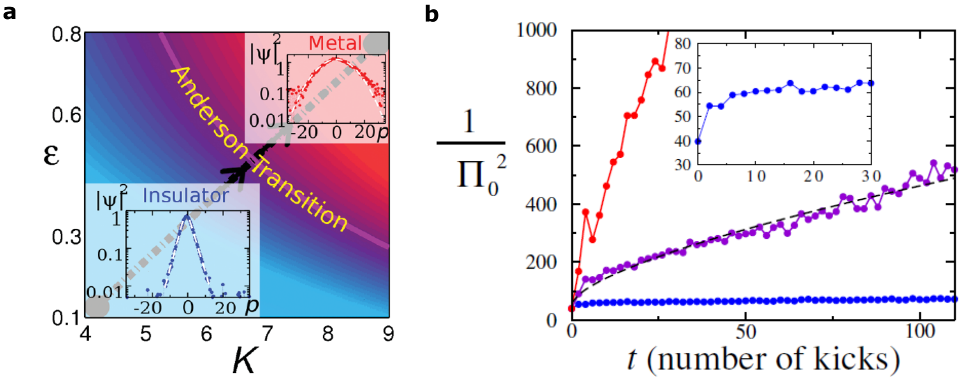

Figure 2.12 | Ultracold atoms: the Anderson transition in momentum space. Panel **a** shows the phase diagram for the quasi-periodic kicked rotors. The black dashed black line shows the trajectory probed in the experiment in [32], so that they could measure the critical parameter on a single point of the (K, ε) space. In **b** one can observe the different time evolution of $\langle p^2(t) \rangle$ above (red) at (purple) and below (blue) the transition. The system goes from diffusive to localized passing through the critical subdiffusive expansion.

Using atomic kicked rotors, it was recently possible to observe the Anderson transition and to measure the analogue of the mobility edge in the specific parameter space of the system. The result was published in 2008 and the experimental system consisted in a sample of cold cesium atoms exposed to a pulsed optical lattice along one spatial direction [32]. The system Hamiltonian is

$$H = \frac{p^2}{2m} + K \cos x [1 + \varepsilon \cos(\omega_2 t) \cos(\omega_3 t)] \sum_{n=0}^{N-1} \delta(t - n) \qquad (2.51)$$

where x is the atom position along the laser axis, p is its momentum, K is the pulse intensity, ε the modulation amplitude and $\omega_{2,3}$ are incommensurate frequencies. The main parameters controlling the dynamics of the system are K and ε. The analogue of the mobility edge trajectory in the disorder-energy plane for localization in real space is here provided by a critical line in the (K, ε) plane (Fig. 2.12a). In the experiment reported in [32] they probe the Anderson transition changing the parameters K and ε, so as to move along the dotted line in Fig. 2.12a. In the localized regime, the evolution of the momentum distribution as a function of the number of kicks "freezes" into an exponential curve $\sim \exp(-|p|/p_{loc})$ after a certain localization time. In the diffusive regime, the intial Gaussian shape is preserved and its squared width increases linearly with the number of kicks. In Fig. 2.12b are reported the data taken at different points on the (K, ε) plane, which clearly show a transition from the localized to the diffusive regime.

Besides providing a measurement of the critical point, the authors also deduce the critical exponents for the divergence of the localization length below the critical point and for the vanishing of the diffusion constant above it. They obtain $s = \nu = 1.6 \pm 0.05$ which is in agreement with the numerical result $\nu = 1.58 \pm 0.01$ [17, 10].

Localization in real space

In the past decade, ultracold gases have proved to be an even more interesting tool for the exploration of disorder-related topics, when one let them interact with spatially disordered potentials. In this case one can realize truly random potentials with almost arbitrary statistical properties, by properly shaping laser light. Exploiting Feshbach resonances, one can tune the atom-atom interaction down to the level of creating an ideal gas of independent particles as in the Anderson Hamiltonian, or use finite attractive or repulsive interactions to investigate the interplay of disorder with nonlinearities. What is also extemely appealing is the possibility of imaging directly the atomic wavefunction. In a study about AL this allows to have direct access to the localized or extended nature of the atomic states, with no need to deduce it from macroscopic observables as the conductivity. From a general point of view, ultracold atomic systems in random optical potentials have all the necessary ingredients to realize the long-awaited quantum simulator of the original Anderson problem, where non-interacting quantum particles move in a disordered potential. Such systems could also allow to simulate how the localization problem changes in presence of interactions, closing the gap with the original problem of disordered electronic systems.

The first series of experiments with ultracold atoms culminated with the observation of AL in 1D in 2008 [33, 34]. Since then the attention has shifted to the 2D and 3D problems, which are more delicate to treat but also much more interesting, since in 3D there is an Anderson transition between localized and diffusive states, and 2D is the critical dimensionality for the transition. Two recent experiments in 3D have reported a clear observation of the Anderson transition, i.e. a dramatic change of the transport properties around a critical energy range [35, 36, 37]. However, a direct determination of the mobility edge has so far not been possible, because of an important missing ingredient, i.e. the capability to control and measure the energy distributions. The experiment reported in this thesis was designed to fill this gap and, through a simultaneous control of the energy distributions of both disorder and atoms, provide the first experimental measurement of the mobility edge in atomic systems.

The two previous experiments on cold atoms in 3D disorder mentioned above have been the first significant results in this context, and have surely inspired the work I am going to present.

It is therefore mandatory for me to briefly report here the main results they achieved.

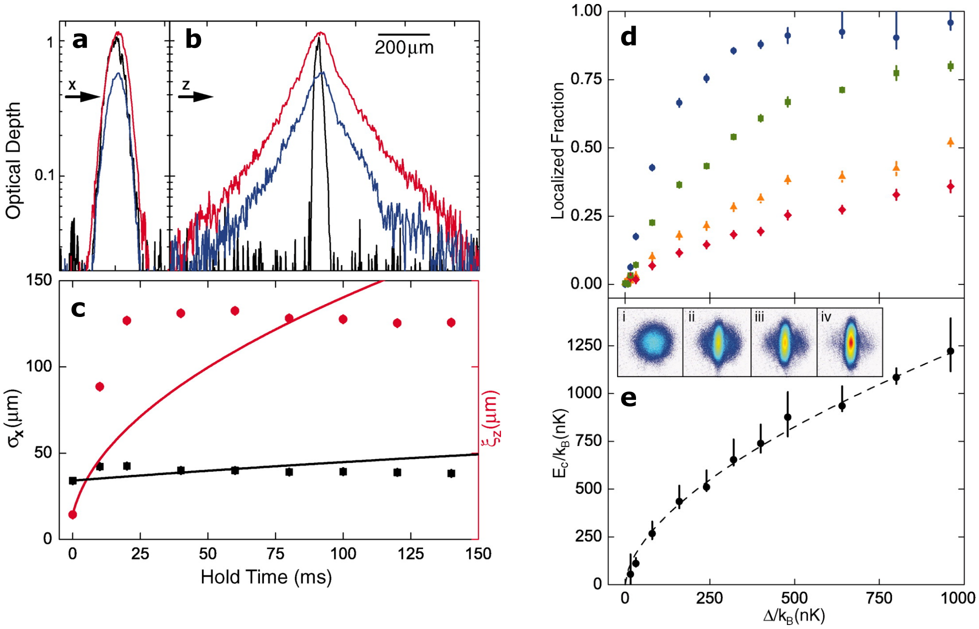

Figure 2.13 | 3D Anderson localization of cold atoms: experiment by the Urbana-Champaign group. In **a,b,c** is showed the dynamics of a localized sample. **a** and **b** are the density profiles at different times (increasing from black to red to blue) along two spatial directions. In **c** is the time evolution of the fitted widths, showing a flattening with respect to the classical evolution (solid lines). In **d** are the data of the localized fraction as a function of the disorder strengths Δ for different temperatures (decreasing from blue to red). Finally, in **e** is the plot of the mobility edge deduced from **d** versus the disorder strength Δ. Figures from [35].

The first experiment was performed in Urbana-Champaign by the group of B. DeMarco [35]. They use fermionic ^{40}K atoms in a single tightly focused speckle beam creating a repulsive disordered potential. They probe the localized/diffusive nature of the atoms by imaging the density profiles after the gas has expanded for a variable time in the speckle potential. For every finite value of the disorder strength Δ they observe double-component profiles, where a fraction of the atoms expand according to a diffusive behavior, while the rest of the atoms get localized by disorder. Using a heuristic fit of the experimental profiles to separate the two components, they reconstruct the localized fraction for different values of the disorder strength and of the initial temperature. The mobility edge is hence deduced from the measured localized fractions assuming that the energy distribution of the atoms is not affected by the disordered potential, thus simply considering the thermal distribution they had before switching on the speckle potential. The results are reported in Fig. 2.13. They find that the mobility edge increases with Δ according to $E_c \propto \Delta^{0.59 \pm 0.02}$. For completeness, I must say that there are several doubts about the validity of these results [38, 39]. They concern in particular: 1) the waiting times used to observe localization, which seem too short to allow a proper distinction between localized and extended states, probably leading to an overestimation of the localized fraction; 2) the assumption that the switching on of the disordered potential does not perturb the atomic energy distribution. The two raised concerns are so significant that they can compromise the validity of the results. For this reason the conclusions reported in [35] about the position of the mobility edge are usually not considered as a conclusive result.

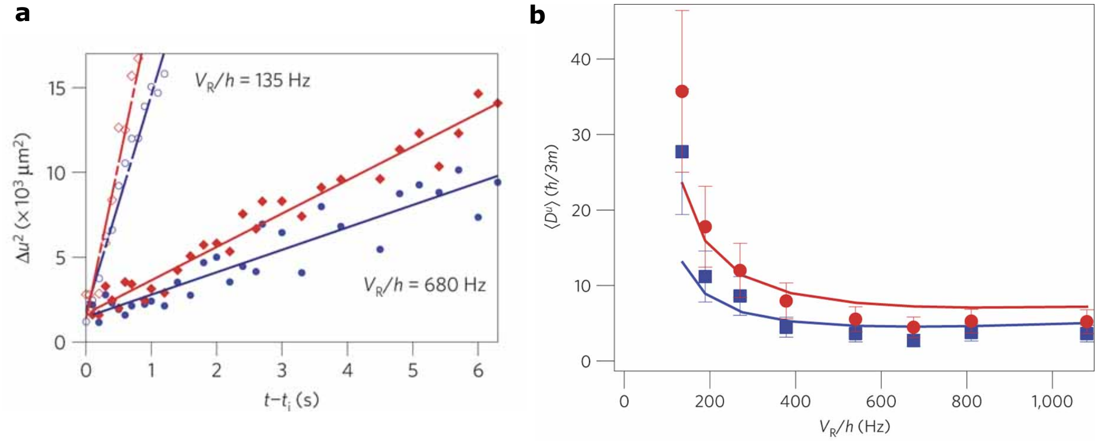

Figure 2.14 | 3D Anderson localization of cold atoms: experiment by the Palaiseau group. In **a** the time evolution of the squared width along two spatial directions (red and blue) for two different disorder strengths. The diffusion coefficients deduced from the linear fits (solid lines) are reported in **b**. D decreases for increasing disorder strengths, finally reaching values of the order of the quantum limit $\hbar/3m$.

The second experiment was performed in Palaiseau by the group of A. Aspect and V. Josse [36]. They use bosonic atoms of ^{87}Rb placed inside an optical disordered potential, realized by means of two coherent speckle beams. Also in this case they study the expansion of the cloud in the speckle potential for different values of the disorder strength. For sufficiently high disorder strengths they observe a double-component behavior in the time evolution of the density profiles. A steady localized part is the replica of the initial profile at all times, while a diffusive fraction continues to evolve. The localized fraction is obtained as the asymptotic limit for $t \to \infty$ of $n(0,0,t)/n_i(0,0)$, that is the ratio of the central peak amplitude at time t over the initial one. The maximum localized fraction they find is 22%. The experimental results are compared with a self-consistent theory calculated for the specific parameters of the experimental setup. They find a qualitative agreement between the two, but a quantitative agreement is restored only by adding a heuristic shift to the energy distribution obtained by simulating the experimental procedure to switch on the disorder. In the absence of an independent determination of the energy distribution they could not provide any estimation for the mobility edge. This second experiment is performed under well controlled experimental conditions and reports a careful analysis of the data, which allows to clearly demonstrate the occurrence of the Anderson transition.

2.4 In summary: results and open quetions about the mobility edge

In the path traced so far I have tried to recall, among the many studies performed about Anderson localization, those results that are most significant to better understand and appreciate the experiment reported in this thesis. Let us briefly summarize which are the questions about the Anderson transition that have been fully or partially understood and those which are still considered open problems.

From the formulation of the scaling theory we have clearly focused the role of dimensionality in AL. For $d \leq 2$ there exists no metallic regime, so that whatever small amount of disorder in the system causes localization. In 1D and 2D there is no Anderson transition and the only effect of an increasing particle energy is a weakening of the localization (the localization length increases with the energy). On the contrary, in 3D the system can be found to be a metal or an insulator. The two phases are separated by a second-order quantum phase transition, which occurs at a critical energy, the mobility edge, whose value depends on the disorder strength. The critical behavior at the transition is characterized by two critical exponents, defining the divergence of the localization length below the mobility edge and the vanishing of the diffusion constant above it. The two critical exponents, which are equal for $d = 3$, have been predicted by numerical simulations and measured in kicked-rotors experiments.

What is still to be investigated is the occurrence of AL in the critical dimension $d = 2$. Experimental results about it are still few. Some of the open questions in this context concern how the phase diagram changes when time-reversal symmetry is broken and how the Anderson transition emerges at $d = 2 + \epsilon$. Further investigations are also required about the universality of critical exponents in 3D, in order to verify if they are affected or not by the specific statistical properties of the disorder potential.

The main issue always remains the position of the mobility edge. Some results have been obtained, but a full assessment of the problem is still missing. Experiments performed with classical waves and atomic kicked rotors have confirmed the qualitative Ioffe-Regel criterion for localization and have measured the critical parameters in a single point of the relative phase diagrams. Theoretical calculations have provided reliable predictions for the mobility edge in the Anderson model but these results could not be tested in any experimental system, since it does not fit with the realistic conditions of electrons in solids. Several improvements have been recently obtained with numerics and perturbative approaches to locate the threshold for realistic experimental conditions, e.g. for ultracold atoms in optical random potentials. These predictions anyway need a confirmation from experiments, since the effect of the finite size in numerical simulations and of approximations in the perturbative theories need to be verified. Recent investigations on ultracold atomic systems in 3D disorder have provided evidence of the Anderson transition. The experiment I am going to present has been designed to have the suitable control on the system parameters to allow a deep characterization of the full 3D phase diagram. I will then show how it allowed to probe the localization threshold on a broad range of disorder strengths so as to provide the first experimental characterization of the mobility edge trajectory in the disorder-energy plane.

Chapter

3 Experimental setup for the production of non-interacting matter waves

In the Introduction of this thesis I anticipated that the principal resource of this work is the use of an atomic Bose-Einstein condensate (BEC). In the last part of the previous chapter I also showed that the most promising results in the recent research about Anderson localization have been obtained in the context of quantum gases. In this chapter I will then present the atomic system used in the experiments of this thesis, introducing the peculiar properties that make it suited for a study about AL and describing the experimental apparatus to produce it.

In order to understand the relevance that cold atoms have had, and still can have, in the study of disorder-related phenomena, it can be useful to briefly mention their importance from a more general point of view. Few years after the first realization of atomic BECs, the Nobel laureate W. Ketterle defined ultracold atomic systems as *"a new window into the quantum world"* [40]: this statement has certainly been proved in the following twenty years. Ultracold gases indeed offer an unprecedented possibility to study quantum phenomena. This is related: 1) to the high degree of controllability on the relevant physical parameters: one can have either fermions or bosons by properly choosing the atomic species, choose the dimensionality of the system, tune the mutual interactions, control the temperature and arrange the shape and the intensity of the external potentials; 2) to the detection possibilities: from the first and simplest imaging techniques that allow to directly access the atomic distributions to the latest single-particle detection; 3) to the various and extreme regimes that can be reached in this 'artificial' systems. It is then clear that the coexistence of such peculiar properties makes ultracold gases a unique investigation tool. The research presented in this thesis takes advantage of this, to study the problem of Anderson localization. I find that the use of cold atoms in this research field is a clear example of what just said. Anderson localization can indeed be considered as one of the simplest quantum phenomena, since it relies on few essential ingredients: waves and disorder. This is apparent in the ubiquity of the phenomenon, which is found wherever these two are present. Nonetheless they are usually mixed up with other elements, as Coulomb interactions for the electrons in solids or absorption effects for light in random media. In this context quantum gases offer their contribution, by allowing to simplify the problem: one can indeed dispose of non-interacting atoms in a random potential, nothing more. Even more interestingly, cold atoms allow to gradually reintroduce those "undesired" effects to study how they perturb the simplest Anderson picture and reproduce the realistic conditions in common materials.

Now that it is clear why to approach ultracold atoms in order to study AL, let us consider the specific case of our interest. For the study we want to carry out, the choice of the atomic species is ditacted by a main requirement: we need to control the atomic interactions. For this reason we decided to employ potassium-39, since it displays convenient magnetic Feshbach resonances that allow to achieve the purpose. It is a bosonic sample which is cooled down to quantum degeneracy and loaded in a random potential. In this chapter I will present the experimental setup for the production of BECs (for a detailed description see Refs. [41, 42, 43]), while the disordered potential is presented in details in Chapter 4.

Here I first recall the essential concepts related to Bose-Einstein condensation and to cooling and manipulation of ultracold atoms (Sec. 3.1). In Sec. 3.2 I introduce the main properties of ^{39}K which are relevant to our study. In Secs. 3.3 and 3.4 I describe the apparatus and the experimental sequence used to produce the BEC. Finally in Sec. 3.5 I introduce the imaging techniques used to detect the atoms.

3.1 Quantum degeneracy and manipulation of neutral atoms: basic concepts

In order to present the setup used to produce our ^{39}K BEC, it is useful to recall the main concepts underlying Bose-Einstein condensation and the techniques to cool and trap the atoms.

3.1.1 Bose-Einstein condensation

Bose-Einstein condensation corresponds to a macroscopic occupation of bosonic particles in the lowest energy state of a quantum system. This condition is achieved when atoms are cooled below a certain critical temperature T_c. Atoms at a temperature T and with mass m can be regarded as quantum-mechanical wavepackets that have a spatial extent on the order of the thermal de Broglie wavelength

$$\lambda_{dB}(T) = \sqrt{\frac{2\pi\hbar^2}{mk_BT}}. \tag{3.1}$$

The value of λ_{dB} is the position uncertainty associated with the thermal momentum distibution and increases with decreasing temperature. In a sample with atomic density n, when atoms are cooled to the point where λ_{dB} is comparable to the interatomic separation, that is when the phase-space density $n\lambda_{dB}^3 \simeq 1$, the atomic wavepackets overlap and the gas starts to become a 'quantum soup' of indistinguishable particles. Bosonic atoms undergo a quantum-mechanical phase transition and form a Bose-Einstein condensate, a cloud of atoms all occupying the same quantum mechanical state.

In cold atoms experiments, Bose-Einstein condensation is typically obtained with atoms held in a harmonic trap. In this case the phase-space density is given by

$$n\lambda_{dB}^3 = \left(\frac{\hbar\omega}{k_B}\right)^3 \frac{N}{T^3} \tag{3.2}$$

where ω is the geometric average of the trapping frequencies along the three spatial directions and N is the atom number. The condition for condensation $n\lambda_{dB}^3 \simeq 1$ is then equivalent to

$$T_c \simeq \frac{\hbar\omega}{k_b} N^{1/3}. \tag{3.3}$$

In the regime where BE condensation occurs, the system reaches densities high enough to make two-body collisions non-negligible. It is then necessary to take into account atom interactions to properly describe the system. In the case of cold dilute gases the interaction problem can be treated with a mean-field description, so that $V_{int}(\mathbf{r}) = g \cdot n(\mathbf{r})$. The coupling constant g is defined by a single parameter, the scattering length a, which describes the effective size of the atom for s-wave scattering: $g = \frac{4\pi\hbar^2}{m}a$ [44].

The evolution of the wavefunction $\psi(\mathbf{r}, t)$ for a weakly interacing condensate with N atoms in an external potential $V(\mathbf{r})$ is governed by the time-dependent Gross-Pitaevskii equation (GPE):

$$i\hbar\frac{\partial}{\partial t}\psi(\mathbf{r}, t) = \left[-\frac{\hbar^2}{2m}\nabla^2 + V(\mathbf{r}) + g|\psi(\mathbf{r}, t)|^2\right]\psi(\mathbf{r}, t). \tag{3.4}$$

This equation simplifies by considering the stationary regime, where the wavefunction is written as $\psi(\mathbf{r}, t) = \phi_0(\mathbf{r})e^{-i\mu t/\hbar}$, with μ the condensate chemical potential, which describes the increase of the total energy by adding an atom to the condensate. The stationary GPE becomes

$$\left[-\frac{\hbar^2}{2m}\nabla^2 + V(\mathbf{r}) + g|\phi_0(\mathbf{r})|^2\right]\phi_0(\mathbf{r}) = \mu\phi_0(\mathbf{r}). \tag{3.5}$$

The terms in the square brackets corresponds, from left to right, to the kinetic energy of the condensate, to its potential energy and to the interaction energy.

When the atom number is large, the interaction energy dominates, so that we can neglect the kinetic term to solve the GPE. This is the so-called Thomas-Fermi regime, where Eq. 3.5 becomes an algebraic equation from which we get the condensate density distribution

$$n_0(\mathbf{r}) = |\psi_0(\mathbf{r})|^2 = \frac{1}{g}\left[\mu - V(\mathbf{r})\right] \tag{3.6}$$

valid for $\mu > V(\mathbf{r})$. Considering the harmonic trapping potential used to hold the atoms, we find that the BEC density distribution assumes the shape of an inverted parabola

$$n_0(\mathbf{r}) = \frac{\mu}{g}\left[1 - \sum_{i=x,y,z}\left(\frac{i}{r_i^{TF}}\right)\right] \tag{3.7}$$

where

$$r_i^{TF} = \sqrt{\frac{2\mu}{m\omega_i^2}} \tag{3.8}$$

is the Thomas-Fermi radius in the i direction.

The Thomas- Fermi description usually holds in the typical situations of atomic BECs. It is also the case of our experiment, where we use finite repulsive interaction to increase the efficiency of the cooling sequence to quantum degeneracy.

I have then introduced the basic idea of Bose-Einstein condensation, defining the critical condition for its occurrence in usual experimental situations and the effect of weak interactions on the condensate wavefunction. It is now interesting to consider which are the typical regimes of temperature and spatial density we want to achieve, in order to understand the constraints we deal with and the experimental techniques that need to be implemented.

For a normal gas at room temperature and atmospheric pressure, the de Broglie wavelength of the atoms is smaller than the atomic radius and the phase-space density of the gas is around 10^{-7}: this is our starting point. We have then to consider how to increase the phase-space density to reach condensation. The first consideration to do concerns with the atomic density. The BEC transition occurs in a region of the phase diagram in which the equilibrium state of matter is a solid. This means that all BECs are metastable states, the solid state being the real ground state of the system. The first process that leads to solidification is the one in which three atoms collide, two of them forming a molecule and the third ensuring the conservation of momentum. The energy gained from the molecule formation is converted into kinetic energy, leading to the loss of all three atoms from the trap: this phenomenon is hence called three-body loss. If the sample is dilute the probability of finding three atoms close enough to determine such a loss is negligible and the lifetime of the BEC can be long. This fact gives us a limit to the density we can achieve in the system, if we want to avoid losses: this value is set around 10^{14} atoms/cm^3, which corresponds to a 10 s lifetime for the condensate. This also means that there is a maximum value for the transition critical temperature: at this density, no BEC will appear as long as temperature is higher than 100 nK. There is then a long way from room temperature to T_c.

Another fact to be considered in the design of the experiment is that the atoms must be thermally isolated from all materials walls. This is done by trapping atoms with magnetic fields or with laser light inside ultrahigh vacuum chambers. Such traps can store atoms for seconds or even minutes, which is enough time to cool and manipulate them. Pre-cooling is a prerequisite for trapping, because conservative atom traps can only confine neutral atoms with a maximum energy of one kelvin at best (in our specific case the trap depth is just a few millikelvin).

In the following I will then recall the main concepts relative to the interaction of atoms with light and magnetic fields. These are indeed necessary for cooling, trapping and also for tuning inter-atomic interactions via Feshbach resonances.

3.1.2 Atom-light interaction

The first phenomenon that is crucial for the manipulation of neutral atoms is the interaction exerted by laser light on matter [45]. This is relevant both in the cooling process and in the production of conservative potentials. The mechanical effects that light produces on the atom are due to the coupling of the electric dipole of the atom with the electric fields of light and vacuum. The atom is submitted to a force that is the sum of a dissipative term, the so-called *radiation pressure*, and a conservative one, the *dipole force*. The dissipative term is at the origin of laser cooling, while the conservative term is used to produce arbitrary potentials for the atoms.

We can understand these two effects by thinking of the atom as a two-level system, with a transition frequency $\omega_0/2\pi$ and lifetime of the excited state Γ^{-1}. Considering a laser with wavelength λ_L, frequency $\omega_L/2\pi$ and intensity $I(\mathbf{r})$, we can define the generalized detuning of the laser to the atomic resonance as

$$\bar{\delta} = \left(\frac{1}{\omega_0 - \omega_L} + \frac{1}{\omega_0 + \omega_L} \right)^{-1} \tag{3.9}$$

Radiation pressure

A laser propagating towards the atom changes the atomic momentum by $\hbar k_L$ at each absorption of a photon, due to momentum conservation. Once excited, the atom emits the photon at a rate

$$\Gamma_{sc} = \frac{\Gamma}{2} \frac{s(\mathbf{r})}{1 + s(\mathbf{r})}, \tag{3.10}$$

where $s(\mathbf{r})$ is the saturation parameter

$$s(\mathbf{r}) = \frac{I(\mathbf{r})/I_{sat}}{1 + 4\bar{\delta}^2/\Gamma^2} \tag{3.11}$$

and I_{sat} is the saturation intensity. As the photon is emitted in a random direction, the repeated absorption of photons results in a dissipative force along the direction of the laser beam with intensity

$$F_{rp}(\mathbf{r}) = \frac{\hbar k_L \Gamma}{2} \frac{s(\mathbf{r})}{1 + s(\mathbf{r})}. \tag{3.12}$$

The optimal condition to have strong radiation pressure is to have the laser on resonance with the atomic transition so as to enhance the probability of photon absorption.

Dipole force

The so-called dipole force is related to a spatial variation of the light amplitude. The origin of this effect lies in the shift induced by light on the energy levels of the atom. The gradient of this energy shift, due to a gradient in the light intensity, is then felt by the atoms as a force. If the laser is red-detuned with respect to the atomic transition, $\omega_L < \omega_0$, the atom is attracted to the region of highest intensity, where the light shift provides the lowest energy state. In the case of blue-detuning, $\omega_L > \omega_0$, the atom is instead repelled from the high intensity regions. This means that red/blue-detuned light corresponds to attractive or repulsive forces respectively.

This type of force is a conservative one and can thus be expressed in terms of a dipole potential

$$V_{dip}(\mathbf{r}) = -\frac{3\pi c^2}{2\omega_0^2} \frac{\Gamma}{\delta} I(\mathbf{r}). \tag{3.13}$$

The dipole force exerted by light is of fundamental importance, since it offers the opportunity to design conservative potentials for the atoms, simply proportional to the light intensity. In our experiment it is used both to trap the atoms during the last part of the cooling sequence (Sec. 3.3.3) and to produce a disordered potential for the atoms (see Chapter 4).

3.1.3 Laser cooling

The basic idea of laser cooling is to exploit the radiation pressure of Eq. 3.12 to slow down, and hence cool, the atoms in a gas. Consider a laser beam red-detuned with respect to the atomic transition. The Doppler effect enhances the absorption of light by atoms moving opposite to the laser propagation, for which the light is shifted up and hence closer to resonance. Photon absorption corresponds to a transfer of momentum $\hbar k_L$ opposite to the initial atom velocity, so that atoms moving towards the laser source experience a friction force that effectively slow them down. In order to have cooling along all three spatial directions, one has then to use three pairs of counter propagating beams along the three axes. This cooling technique is called *optical molasses*. The limit in the cooling power of this strategy is related to the re-emission processes mentioned above (Eq. 3.10). They do not contribute to the mean atom velocity because they occur in random directions, but they generate a random walk in momentum space that results in a minimum attainable temperature, the so-called Doppler temperature $k_B T_D = \hbar\Gamma/2$. This minimum value is reached for a detuning $\delta = \Gamma/2$.

A further development of this cooling technique allows to simultaneously cool and trap the atoms: it is the so-called *magneto-optical trap* (MOT). The arrangement of laser beams is the same as in the optical molasses and a quadrupole magnetic field is used to provide the additional trapping. The Zeeman shift induced by the presence of the magnetic field on the atomic energy levels increases with the radial distance from the centre of the trap. This implies that, for an atom moving away from the centre, the atomic resonance is shifted closer to the laser frequency, enhancing the probability of absorbing a photon that kicks the atom towards the centre of the trap. The atoms are then cooled and collected at the centre of the quadrupole field.

3.1.4 Magnetic trapping

Aside from optical dipole traps which exploit the conservative potential generated by suitably detuned laser light (Sec. 3.1.2), atomic traps can be realized by taking advantage of the interaction of atoms with magnetic fields.

Consider an atom with a finite magnetic moment $\boldsymbol{\mu}$. When it is placed in a magnetic field $\boldsymbol{B}(\boldsymbol{r})$, the field induces a shift on its energy levels provided by

$$\Delta E(\boldsymbol{r}) = -\boldsymbol{\mu} \cdot \boldsymbol{B}(\boldsymbol{r}). \tag{3.14}$$

According to the sign of $\boldsymbol{\mu}$, the atoms can be *low-field seekers* if the lowest energy levels are those at the lowest magnetic field, or *high-field seekers* in the opposite case. Low-field seeker states can then be trapped in the minimum of a suitable spatially varying magnetic field. It is for examble the case of a quadrupole magnetic field generated by coils in anti-Helmholtz configuration, i.e. with current flowing in opposite directions in Helmholtz coils. This technique is used in our experiment to confine the atoms in the first stages of the cooling sequence (see Sec. 3.4).

3.1.5 Evaporative cooling

Laser cooling techniques introduced above (Sec. 3.1.3) typically allow to reach temperatures of few hundreds of μK. The additional cooling strategy to reach BEC is provided by evaporative cooling [46].

Evaporative cooling is done by continuously removing the high energy tail of the thermal distribution from the trap. The evaporated atoms carry away more than the average energy, which means that the temperature of the remaining atoms decreases. The high energy tail must be constantly repopulated by collisions, thus maintaining thermal equilibrium and sustaining the cooling process. The atoms remaining in the trap have much lower average energy and so they occupy a smaller volume near the bottom of the trap, thereby increasing their density. For trapped atoms (either in optical or magnetic traps), this process can be achieved by lowering the depth of the trap, thereby allowing the atoms with energies higher than the trap depth to escape. Since both the temperature and the volume decrease, the phase-space density increases, finally leading to BE condensation.

3.1.6 Feshbach resonances

At the beginning of this chapter I mentioned that the main reason underlying our choice for the atomic species to use is the possibility to control the interatomic interactions. I conclude this brief overview about the theory related to cold atoms experiments by introducing the physical phenomenon at the origin of the tunability of interactions. This opportunity is provided by magnetic Feshbach resonances, which allow to change the scattering length a by applying a uniform magnetic field. I report here a simple intuitive idea of the origin of Feshbach resonances, referring the reader to [47] for a detailed description.

A Feshbach resonance is a scattering resonance that occurs when two free scattering atoms can couple to a bound state during the scattering process. The atoms scatter in the so-called open channel, which corresponds to a certain spin configuration. For a different spin configuration, called the closed channel, there is a bound molecular state close to the scattering continuum. Due to energy conservation, the atoms cannot enter the closed channel, which has a larger continuum energy. However, when the energy difference ΔE between the incident energy and the bound state becomes small, they can couple to that state during the scattering process. For $\Delta E \to 0$, the scattering length diverges. It is positive when the bound state lies below the scattering continuum, and negative when it lies above. If there is a difference $\Delta\mu$ in the magnetic moments of the two channels, ΔE and thus a can be tuned with the help of a homogeneous magnetic field. The resulting dependence of a on the field B can be modeled by

$$a(B) = a_{bg}\left(1 - \frac{\Delta}{B - B_0}\right) \tag{3.15}$$

where a_{bg} is the background scattering length in absence of coupling with the molecular state, B_0 is the center of the resonance and Δ is the width of the resonance, defined as $\Delta = B_0 - B_{zc}$ with B_{zc} the field at which the scattering length vanishes. In proximity of the zero-crossing $B \approx B_{zc}$, the behavior of $a(B)$ is approximately linear, according to

$$a(B) \sim \frac{a_{bg}}{\Delta}(B - B_0). \tag{3.16}$$

In our experiment Feshbach resonances are exploited for two main reasons: during the cooling sequence, and in particular during the evaporative cooling, they are used to increase the collisional rate and improve the evaporation efficiency, while, in the last part of the experimental sequence they are used to achieve a desired interaction strength according to the experiment we want to perform.

3.2 Potassium-39

Most of the existing quantum gases experiments make use of alkali atoms. The main reason for this lies in their optical properties. They indeed have closed transitions with strong dipole moments in a convenient spectral range (visible or near infrared), so that they can be easily manipulated with laser light. In addition to this, they display strong enough magnetic moments, of the order of a Bohr magneton, which allows a good coupling with magnetic fields.

Potassium belongs to this class of atoms. In this experiment we use the most naturally abundant of its bosonic isotopes, i.e. ^{39}K. The optical properties of this atomic species are analogous to those of all the alkalis, while its peculiarity lies in the scattering properties. It indeed presents many convenient Feshbach resonances at easily accessible magnetic fields, which allows to tune the strength of the contact interactions at will.

3.2.1 Optical properties

In Fig. 3.1 I report the relevant hyperfine structure of ^{39}K. The $^2S_{1/2}$ ground state has two sublevels, which are labeled by the value of the total angular momentum $F = 1, 2$. The strongest spectral lines of the ground state are the D1 ($^2S_{1/2} \rightarrow\ ^2P_{1/2}$) and D2 ($^2S_{1/2} \rightarrow\ ^2P_{3/2}$) lines. Among these, the D2 line is the one with the strongest dipole moment and is therefore the most suitable for cooling. Its natural line width is $\Gamma_2/2\pi = 6.035(11)$ MHz. The Doppler temperature associated to this line is $T_D = 145\mu$K and its saturation intensity is 1.75 mW/cm^2.

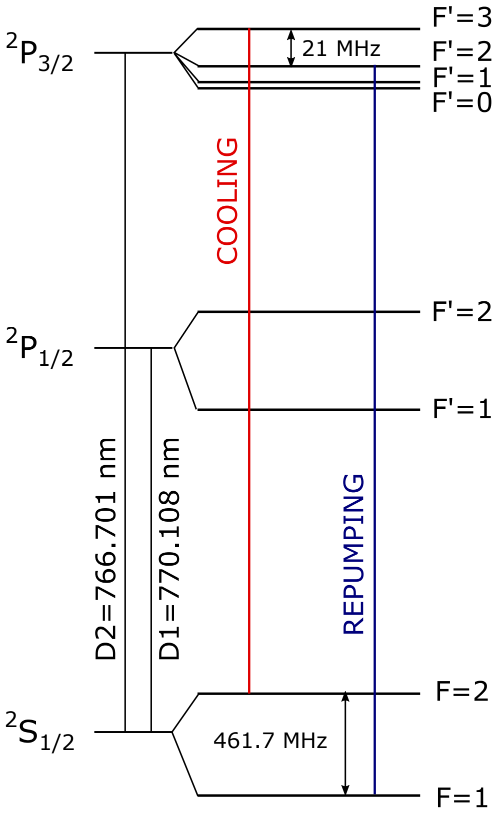

Figure 3.1 | Optical transitions. I report the relevant atomic levels and the corresponding spectral lines of ^{39}K. In red and blue are highlighted the transitions exploited for cooling.

The narrow hyperfine structure of the excited level causes strong out of resonance transitions and thus prevents the use of a single frequency for cooling, which would result in a fast accumulation of atoms in the uncoupled ground state. For this reason we also exploit the $F = 1 \rightarrow F' = 2$ transition to repump the atoms out of the $F = 1$ state.

3.2.2 Zeeman sublevels

In presence of a static magnetic field, the Zeeman effect causes a splitting of the atomic energy levels which depends on the field strength. In Fig. 3.2 I report the structure of these sublevels for the $F = 1$ and $F = 2$ manifolds, which is important both for magnetic trapping and for the implementation of radio-frequency transitions among different hyperfine states. Note that, at low field, the only low-field seeker state in the $F = 1$ manifold is $m_F = -1$.

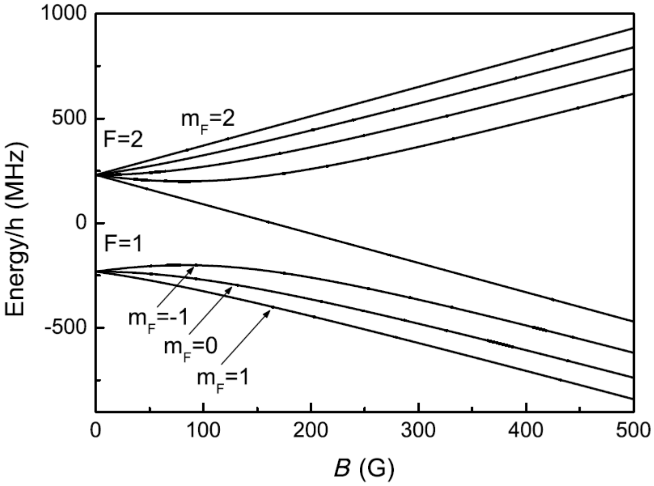

Figure 3.2 | Magnetic field dependence of the hyperfine states of the $^2S_{1/2}$ ground state. The energy levels are labeled by their quantum numbers $|F, m_F\rangle$ at low field B, where the level splitting is well described by the Zeeman effect. For fields higher than 50 G a partial Paschen-Back picture would be more appropriate.

3.2.3 Scattering properties

The natural scattering length of ^{39}K is $-30\ a_0$, where a_0 is the Bohr radius. Such a small and negative scattering length would normally prevent to reach Bose-Einstein condensation. The interesting property of ^{39}K is that it displays a number of magnetic Feshbach resonances that allow to tune the scattering length under achievable experimental conditions. The good properties of a Feshbach resonance for a fine tuning of the scattering length are a small a_{bg} and a large ΔB.

The main resonances of ^{39}K relative to the Zeeman sublevels of the groundstates have been detected in [48] and are listed in Table 3.1. In Fig. 3.3 I report the behavior of $a(B)$ for the Feshbach resonance which is most relevant for our experiment, i.e. the one for the $m_F = 1$ state centered at $B_0 = 403.4$ G.

m_{F_1}, m_{F_2}	$B_0(G)$	$-\Delta B(G)$	$a_{bg}(a0)$
+1, +1	25.85 ± 0.1	0.47	-33
	403.4 ± 0.7	52	-29
	(745.1)	0.4	-35
	752.3 ± 0.1	0.4	-35
0, 0	59.3 ± 0.6	9.6	-18
	66.0 ± 0.9	7.9	-18
	(471)	72	-28
	(490)	5	-28
	(825)	0.032	-36
	(832)	0.52	-36
-1, -1	32.6 ± 1.5	-55	-19
	162.8 ± 0.9	37	-19
	562.2 ± 1.5	56	-29

Table 3.1 | Feshbach resonances for ^{39}K. Numbers in brackets correspond to theoretical predictions. All values are taken from [48].

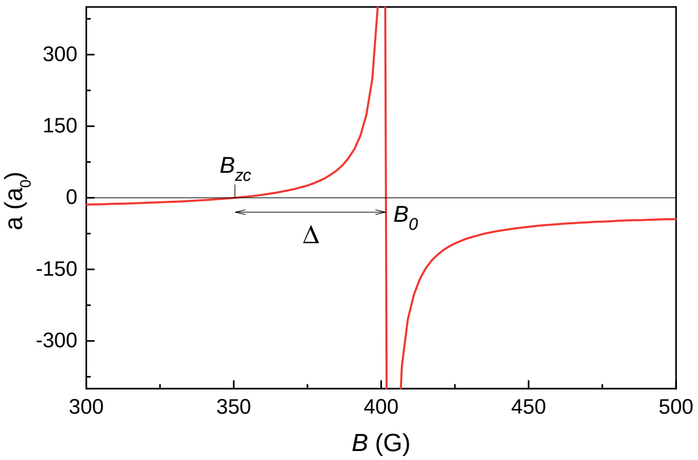

Figure 3.3 | Example of a broad Feshbach resonance of ^{39}K. Magnetic field dependance of the scattering length for the $m_F = 1$ state close to the Feshbach resonance centered at 403.4 G.

3.3 Experimental apparatus

Quantum degeneracy is reached via three successive cooling stages performed in three different vacuum chambers. The basic structure of the experimental apparatus is reported in Fig. 3.4. In the first chamber the atoms are collected from the background gas into a two-dimensional magneto-optical (2D MOT) trap. An atomic beam is then pushed in the following chamber, where the atoms are loaded in a three-dimensional magneto-optical (3D MOT) trap and cooled to sub-Doppler temperatures. The atoms are then transferred to a magnetic trap which is moved, thanks to a motorized translation stage, to the final science chamber. There the sample is loaded into a dipole trap, where we perform evaporative cooling. During this last cooling stage we exploit the Feshbach resonances of ^{39}K, in order to increase the elastic collisional rate

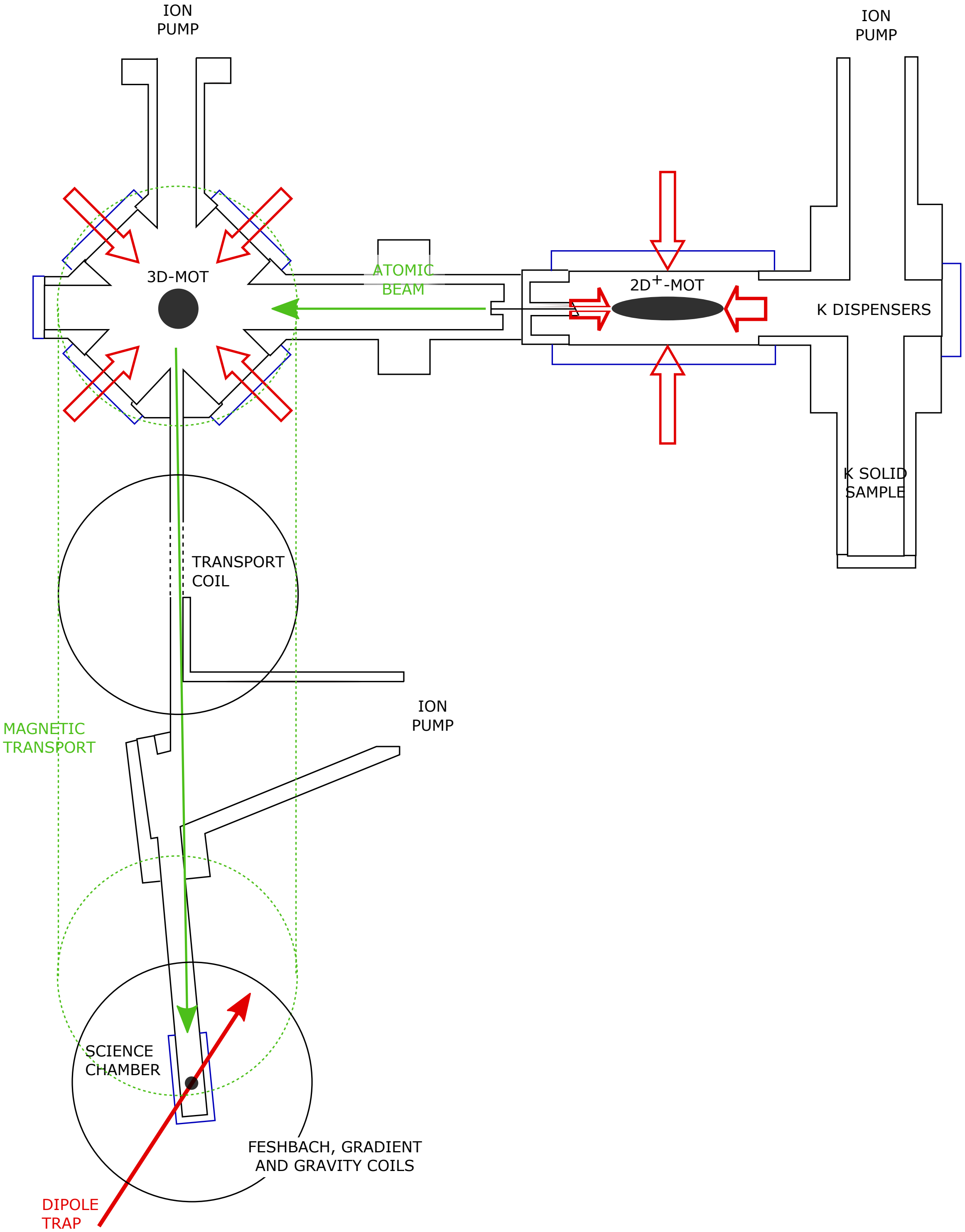

Figure 3.4 | **Scheme of the experimental apparatus.** Top view of the three vacuum chambers, with related vacuum pumps. The cooling laser beams on the horizontal plane are indicated by red arrows, while the main trasport stages are reported in green.

and optimize the efficiency of the cooling process, which finally leads to BEC. In the rest of this Section, I will describe the main parts of the experimental apparatus, i.e. the vacuum chambers, the lasers for cooling and trapping the atoms and the magnetic field coils. The experimental procedure to reach BEC is described in details in Sec. 3.4.

3.3.1 Vacuum chambers

The basic scheme of the experimental apparatus was designed according to two main requirements: a long lifetime and a good optical access onto the atoms in the final science chamber. To this purpose the experiment was built with three different vacuum chambers, each connection between adjacent cells hosting a differential pumping stage that reduces the pressure and increases the lifetime of the atomic sample.

In the 2D MOT chamber we use an ion pump that achieves an effective pumping speed at the chamber of 6.8 l/s. During normal operation, the vapor pressure of potassium is anyway limited by the fact that we continuously release potassium in the chamber, either by using current-driven dispensers or by heating up a solid sample. The estimated pressure there is $p \approx 10^{-8}$ mbar.

In the 3D MOT chamber a second ion pump achieves an effective pumping speed of 17 l/s. Considering the leading contributions to the outgassing rate, we estimate an attainable pressure of $p \approx 7 \times 10^{-10}$ mbar. This pressure is compatible with the measured lifetime of the atomic sample which is around 3-4 s.

The last pumping stage is achieved thanks to the combined action of an ion pump and a titanium sublimation pump. Considering the pumping speed at the science chamber and the outgassing rate of the glass composing the cell, we get an achievable pressure of 10^{-11} mbar. Due to the small section of the glass pipe, the pumping speed at the final position of the atoms is quite low, of the order of 5 l/s. Our strategy consists in achieving a high pumping speed at the conjuction of the glass pipe to the main body of the vacuum system, i.e. to realize a high differential vacuum with respect to the previous chamber. This strategy relies on the low outgassing rate of the materials employed in the final part of the apparatus. The measured lifetime of the atoms in the science chamber confirms the validity of this approach: atoms held by the quadrupole magnetic trap have a lifetime of about 80 s.

A good optical access in the science chamber is granted by the shape of the glass cell and by the absence of MOT beams, which allows to position a large number of additional trapping beams on the atoms.

3.3.2 Cooling laser system

Laser light for both the 2D and the 3D MOT is derived from a single master laser, a Toptica DL Pro 780, which is very stable but provides only 50 mW at our working wavelength. The laser is then amplified by four Master Oscillator Power Amplifiers (MOPAs).

The laser wavelength is locked on the atomic resonance by performing modulation transfer spectroscopy. The cooling and repumping light frequencies of Fig. 3.1 are then obtained from the same source light, using acousto-optical modulators (AOMs) in double-pass configuration to get the desired 460 MHz shift.

A scheme of the laser setup for cooling light is reported in Fig. 3.5.

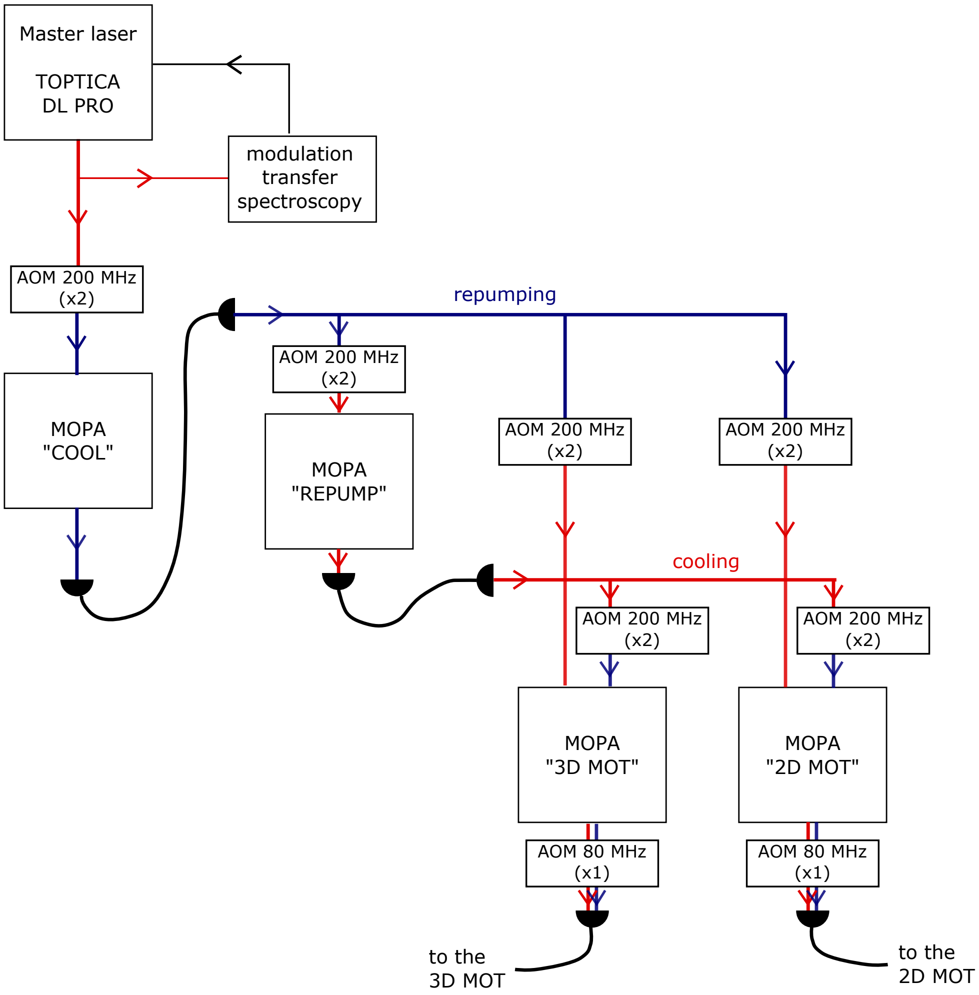

Figure 3.5 | Scheme of the optical setup for the production of cooling light. The light used in the 2D and 3D MOTs is derived from the same laser source, which is locked to the atomic resonance, amplified by four MOPAs and tuned to the proper cooling (red) and repumping (blue) wavelengths by means of double-pass AOMs. Both wavelengths are collected in two separate optical fibers that bring light to the 2D and the 3D MOTs.

3.3.3 Laser light for dipole potentials

As I introduced in Sec. 3.1.2, red/blue-detuned laser light provides an attractive/repulsive potential for the atoms, proportional to its intensity profile according to Eq. 3.13. In the experimental procedure to produce atomic BECs, we use two red-detuned laser beams to create a crossed optical dipole trap to confine the atoms. In the final phase of the experiment, we use instead blue-detuned laser light to produce a disordered potential. I present here the three laser sources used for these purposes.

Main dipole trap

The main trapping beam enters the cell on the horizontal plane at an angle of 45° with respect to the longitudinal axis of the cell (see Fig. 3.6). It is derived from a IPG-photonics YLR-100-LP-AC ytterbium fiber laser. This laser can provide up to 100 W of laser power at a central wavelength $\lambda = 1064$ nm, with an emission linewidth of 2 nm. We typically operate this laser at around 30 W output power, since at higher power we observe strong photo-association losses caused by the wide emission of the laser. Its spectrum largely exceeds the hyperfine splitting of the ground state. For this reason, Raman transitions, in which a photon is absorbed from one beam and emitted into the other, are allowed and can lead to heating of the sample.

The laser is coupled into an AOM for power control, sent to a system of lenses and focused onto the atoms. It is used to capture the atomic cloud from the quadrupole trap and to perform most of the evaporative cooling (see Sec. 3.4).

Vertical dipole trap

The second dipole trap is aligned on the vertical direction and placed such that its focus is nearly superimposed to that of the major horizontal trap (see Fig. 3.6). It is generated from a Nufern ytterbium fiber amplifier seeded by an Innolight Mephisto S S200 NE. The amplifier can provide up to 10 W laser power. It is used in the final part of the evaporation in order to produce the BEC in a crossed dipole trap, tightly confined along all directions (see Sec. 3.4). It is also left on during the whole experimental sequence, but at lower intensity, to compensate for a spurious magnetic gradient (see Sec. 3.3.5).

Disordered optical potential

The laser used to produce a random potential for the atoms is a home-made Ti-Sa. Its main advantage consists in the tunability of the wavelength between 740 and 860 nm. This allows in principle to detune it both on the red and on the blue side of the atomic transition, so as to vary both the intensity and the statistics of the disordered potential. In the experiments reported in this thesis we normally use it at $\lambda = 762$ nm. All the details about the design and characterization of the disordered potential can be found in Chapter 4.

3.3.4 Magnetic field coils

Several magnetic field coils are used in the experiment. Most of them are used to provide a confining potential for the atoms, apart from the coils that produce the so-called "Feshbach field", i.e. the uniform field used to tune the interaction strength. Here I will briefly summarize the main magnetic field coils used and the properties of the fields they generate.

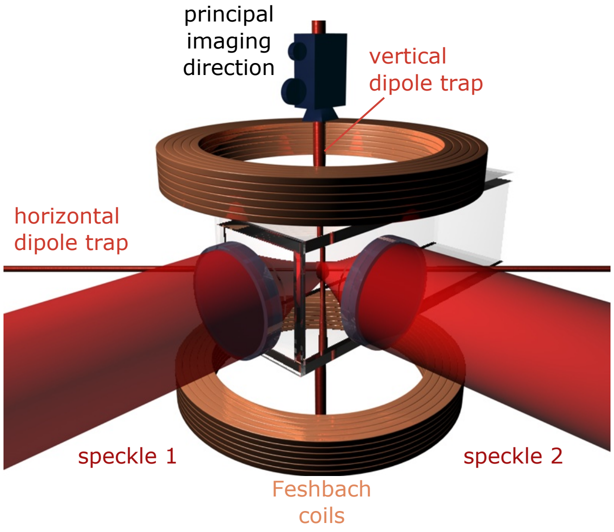

Figure 3.6 | Spatial arrangement of the dipole potentials onto the atoms. The main dipole trap produced by the IPG laser beam is placed horizontally and enters the cell at an angle of 45°. The additional dipole trap is disposed vertically, so as to confine the atoms also along the longitudinal direction of the IPG beam, where it provides only a weak curvature. The two speckle beams enter the cell on the horizontal plane at an angle of 90° one with respect to the other. The position of the Feshbach field coils and of the principal imaging direction are also reported.

MOT coils

In the 2D MOT configuration one needs a magnetic field gradient along the directions of the cooling beams and zero field along the longitudinal axis z. This is realized by means of two pairs of rectangular coils parallel to z and with orthogonal axes (see Fig. 3.7). The current in the four coils flows in such a way that the field gradient generated by each of them sum to the other along the radial directions, while it subtracts to zero along the longitudinal one.

The magnetic field gradient necessary to the 3D MOT operation is produced by a pair of circular coils with their axes along the vertical direction (see Fig. 3.8). They are used in anti-Helmholtz configuration, i.e. with current flowing in opposite directions. In this way one has zero offset field in the center, but a strong field gradient. The gradient on the radial direction is half of that on the vertical one.

Transport coils

The *Transport* coils are the ones placed on a moving cart and aimed at transferring the atoms from the 3D MOT to the science chamber (see Fig. 3.4). They are also used in anti-Helmholtz configuration so that the field gradient at the center produces a strong quadrupole trap for the atoms. Due to the high currents (~ 60 A) used to trap the atoms, the Transport coils are water-cooled, by letting the cooling water flow inside an aluminum box in contact with them.

Feshbach and Gradient coils

The most important among all the magnetic coils are the ones mounted around the science chamber. There we need to produce both a strong quadrupole trap and a uniform magnetic field to tune the atomic interactions via magnetic Feshbach resonances. These two purposes are realized by means of two pairs of concentric coils. One of them (*Feshbach*) is close to the Helmholtz configuration, having the radius approximately equal to the distance between the coils. The other one (*Gradient*) has instead half the radius of the first. Both pairs can be used with current flowing in the same or in opposite directions (Helmholtz/anti-Helmholtz configurations), thanks to a relay system which allows to change the current direction.

Having the Feshbach coils a larger diameter, they are the most suited to trap the atoms from the Transport coils. Therefore they are initially used in anti-Helmholtz configuration. Then the atoms are transferred to the magnetic trap generated by the Gradient coils, so that the first can be switched to the Helmholtz configuration and are used to tune the scattering length.

The coils are mounted in a plastic box where water continuously flows to achieve active cooling.

Gravity compensation coils

The last pair of coils is used to compensate gravity. They are also mounted inside the plastic box around the science chamber and they are used in anti-Helmholtz configuration in order to produce a vertical field gradient opposite to gravity.

3.3.5 Residual curvatures

During the experiments reported in Chapter 5 the only magnetic fields used are the uniform Feshbach field to control the interactions and the field gradient to compensate gravity. The two sets of magnetic field coils generate weak curvatures, which we partially compensate with a weakly focused laser beam in the vertical direction. It is the same laser beam that is initially used to produce the crossed dipole trap, which is now set to a lower power (see Sec. 3.3.3). The first non-negligible terms of the resulting potential around the initial position of the atoms are $V_{res}(x, y, z) \simeq \frac{1}{2}m(-(2\pi \times 3.22\text{Hz})^2 z^2 + (2\pi \times 11\text{Hz})^2 y^2 - (12\text{Hz}^2/\mu m)x^3)$, where z is oriented along the vertical direction, y is the longitudinal direction of the IPG beam and x is orthoghonal to both. The anti-trapping curvature along z is caused by a nonperfect Helmoltz configuration of the Feshbach coils. In the x direction the off-center dipole trap cancels a magnetic field gradient along the same direction. The resulting potential has a cubic spatial dependence, flat around the atoms position to allow for a free expansion in the disorder. In the y direction the same optical trap contributes to a weak trapping potential. By noticing that the typical energy scale in the system is of several tens on nK (see typical energies in Chapter 5), we could define a spatial region in which the spurious fields stay below $\sim$ 5 nK, so that if the system remains within this region, we can consider negligible the effect of the residual curvatures. The size of the region amounts to 144 μm along z, 42 μm along y and 112 μm along x. Note that the potential corresponds to antitrapping in two directions, and to trapping in the third direction, suggesting that the net effect on the 3D problem is less than that in the individual directions.

3.4 Cooling to degeneracy

3.4.1 2D$^+$ MOT

In the first vacuum chamber we implement a 2D$^+$ MOT, which cools down the atoms in the radial direction and produces an atomic beam towards the second chamber. The total laser power used is about 400 mW, which ensures the sufficient velocity capture range and a good atomic flux. The total power is the sum of the cooling and repumping light, which in the 2D MOT beams have equal power. For the radial trapping we employ two transverse beams with 9 and 44 mm vertical and horizontal waists respectively. In the 2D$^+$ configuration two additional laser beams are employed along the atomic beam direction. A "push" beam propagates in the direction of the atomic flux, while a "retarding" beam propagates in the opposite direction. These two beams have a waist of 5 mm. The retarding beam comes into the chamber from below and it is retroreflected by a mirror at 45° with respect to the atomic flux direction, placed inside the vacuum. The mirror has a 1.5 mm diameter hole at its center, through which the atoms are ejected. The hole is 30 mm long, so as to reduce the conductivity towards the 3D MOT chamber. Due to the presence of the hole, the retarding beam has a shadow at its center. For atoms outside the shadow, the radiation pressure is balanced in all directions. Once the atoms are cooled down radially, and therefore spend most of their time at the center of the beam, they experience a radiation pressure imbalance due to the shadow and they are pushed towards the 3D MOT chamber. Adjusting the ratio between the power in the "push" and "retarded" beams we are able to optimize the average velocity of the atomic beam so as to maximize the loading of the 3D MOT. Optimum performances were achieved with a flux of 2×10^{10} atoms/s, with an average velocity of 25 m/s.

3.4.2 3D MOT

In the second chamber a 3D MOT configuration is used to slow down, trap and cool the atoms down to sub-Doppler temperatures [41, 42]. The process here can be seen as the result of three main steps: loading, compression and optical molasses. Also in this case the total power used is about 400 mW, but the ratio between cooling and repumping light is now different: the repumper power is about 1/8 of the cooling one. This laser light is split into six independent beams with a waist of 17.5 mm. During the MOT loading, we estimate a velocity capture range of the order of 50 m/s, which is twice the average velocity of the atomic beam entering the cell. We can capture clouds of almost 3×10^{10} atoms at a temperature of 2 mK in 5 s.

During the compressed MOT phase, we decrease the repumper intensity and increase the cooling light detuning to suppress light-assisted collisions that prevent the atoms from getting

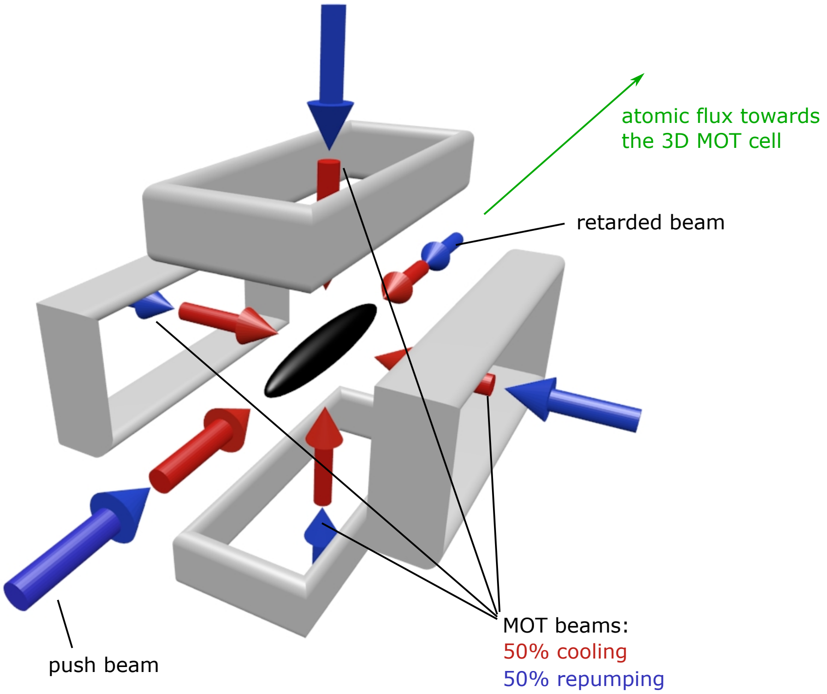

Figure 3.7 | **Scheme of the 2D$^+$ MOT.** In grey are the coils used to produce the suitable magnetic field gradient for the MOT operation. Red and blue arrows represent the laser beams, with the *cooling* and *rempumping* wavelengths respectively. Two pairs of counter propagating beams are used to cool down the atoms along the radial direction. The other two beams cool the atoms along the longitudinal direction until they end up in the central part of the cloud where and are pushed towards the 3D MOT cell, thanks to the radiation pressure imbalance due to the hole at the center of the retarded beam.

too close. This increases the atomic density by a factor 10. Finally, the molasses sequence cools down the sample to sub-Doppler temperatures. This is achieved tuning the cooling light frequency to the red of the strong $F = 2 \rightarrow F' = 3$ D_2 optical transition to exploit sub-Doppler forces, but keeping it sufficiently blue-detuned with respect to the $F = 2 \rightarrow F' = 2$ one to avoid negative friction forces. The narrow separation between the excited states $F' = 3$ and $F' = 2$ might lead to high scatteering rates and strong heating. For this reason we have to accurately tune the light intensity both for the cooling and the repumping wavelengths in order to minimize the achievable temperature. The optimized sequence allows to get about 1.65×10^{10} atoms at a temperature of 25 μK.

At the end of the cooling sequence, we switch off the repumper light so that the atoms are all in the $F = 1$ manifold. Then we switch on a quadrupole field gradient of 30 G/cm. In this way we lose all the atoms which are not in a low-field seeker state, i.e. all the atoms in the $|F = 1, m_F = 0, +1\rangle$ states (see Fig. 3.2). The ones in the $|F = 1, m_F = -1\rangle$ state are instead magnetically trapped. This is a simple procedure to get a fully polarized sample with a reduction of the phase-space density of about 30%.

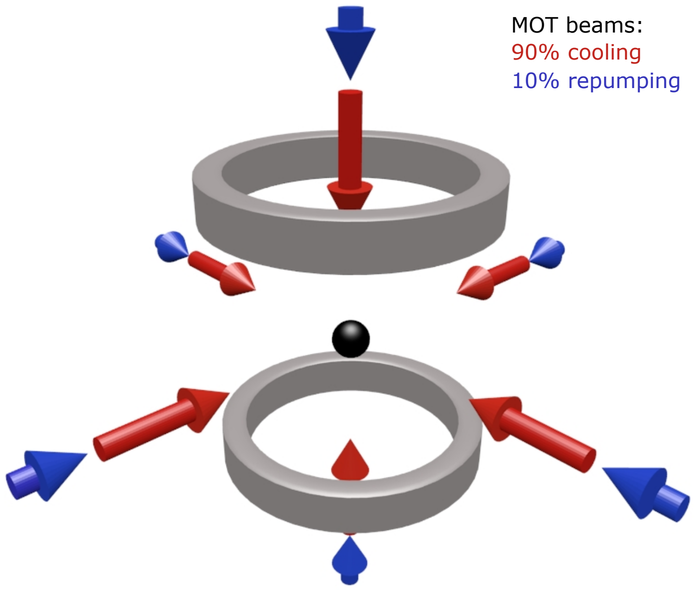

Figure 3.8 | Scheme of the 3D MOT. In grey are the coils to produce the suitable magnetic field gradient for the MOT operation. Three pairs of counter propagating beams are used to cool down the atoms along all directions: red and blue arrows represent *cooling* and *rempumping* wavelengths respectively.

3.4.3 Transfer to the science chamber

In order to transfer the atoms from the 3D MOT chamber to the final glass cell, we ramp up the current in a pair of coils in anti-Helmholtz configuration which are mounted on a moving cart. These generate a magnetic field gradient of 165 G/cm, which allows to transport the atoms over a distance of 540 mm in 2 s with negligible heating. During the trasport phase, we observe atom losses due to the finite lifetime in the tubes connecting the chambers and to the fact that the cloud size is comparable with the tube's cross section. This results in a factor 4 reduction of the phase-space density. When the transport coils are close to the science chamber, the atoms are transferred to a magnetic quadrupole trap generated by the Feshbach coils in anti-Helmholtz configuration. They are finally transferred to the quadrupole trap generated by the Gradient coils, which are adiabatically ramped to their maximum current (~ 60 A) in order to produce a magnetic field gradient of 270 G/cm. At the end of the transfer process we get about 10^9 atoms at a temperature of 250 μK.

3.4.4 Optical dipole trap and evaporative cooling

The last cooling stage to reach Bose-Einstein condensation cannot be performed in a quadrupole trap, due to the presence of a Ramsauer minimum in the elastic cross section of ^{39}K, which occurs for collision energies of 400 μK. The strategy implemented to overcome this limitation is to load the atoms in a dipole trap where we can exploit a magnetic Feshbach resonance to increase the collisional rate and realize efficient evaporative cooling. We use the IPG far-detuned laser beam at 1064 nm introduced in Sec. 3.3.3, which is tightly focused to a waist w=25 μm. The beam is aligned close, but not exactly at, the center of the quadrupole trap to prevent Majorana spin flips. The laser is switched on abruptly and after an optimum loading time the magnetic trap is switched off instantaneously. The optimized loading sequence is achieved for 27 W of trapping laser power and a loading time of 2 s. The number of atoms we can load in the dipole trap is about 30 × 10 ^{6}. The main limitation to the maximum atom number we can achieve is related to the presence of two-body losses. These are mostly attributed to the presence of light-assisted inelastic collisions, enhanced by the multimode spectrum of the laser we use for the dipole trap.

The evaporative cooling is performed by reducing the laser power in the dipole trap from 27 W to about 5 mW in 4 s by means of an acousto-optical modulator (AOM). During the last 1 s of the evaporation sequence, we switch on the vertical dipole trap to increase the trapping frequency along the longitudinal direction of the IPG beam: the power in the vertical beam is reduced together with that of the IPG to perform evaporation. The resulting radial and longitudinal trapping frequencies at the end of the evaporation are 110 Hz and 25 Hz respectively. During the initial part of the evaporation, the scattering length of the atoms is tuned using the low-field Feshbach resonance at 33.6 G for the $m_F = -1$ state. Although the intial density of the cloud is still low, we cannot use too high scattering lengths due to enhanced light-assisted collisional losses close to the resonance. The initial optimum value is $a = 16a_0$, obtained at 70 G. After 100 ms, the lower intensity of the laser reduces atom losses and allows to tune the scattering length to $88a_0$, where the evaporation is more effective. After 1 s, we perform a Landau-Zener radio-frequency sweep to transfer the cloud to the $|F = 1, m_F = +1\rangle$ state and perform the last 3 s of evaporative cooling close to the broad Feshbach resonance at 403.4 G. At the end of the evaporation we obtain BECs with up to 8 × 10^5 atoms. The atoms are suspended against gravity by a vertical magnetic field gradient (see Sec. 3.3.4).

3.5 Imaging techniques

To conclude the presentation of our experimental setup, I briefly introduce the techniques we use to detect the atoms.

3.5.1 Fluorescence imaging of the 3D MOT

In the 3D MOT chamber we dispose of an imaging system which is normally used to check the correct functioning of the first two cooling stages. We use in this case fluoresence imaging, which consists in shining close-to-resonance laser light onto the atoms and recording the light re-emitted by them. We implement this by switching on the MOT laser beams at full power for a very short time and collecting the light emitted by the atoms with a lens placed outside the chamber.

Imaging the cloud at different times during the experimental sequence, we can measure the number and the temperature of the atoms so as to verify the efficiency of the different cooling and trapping steps before the transfer to the science chamber.

3.5.2 Absorption imaging in the science chamber

Detection of the atoms in the glass cell is performed according to the standard absorption imaging technique, i.e. by illuminating the atoms with a resonant laser beam and recording the shadow they produce onto a CCD camera. We obtain a first image which provides us the two-dimensional profile $I_{out}(\mathbf{r})$. A second image is taken without the atoms, obtaining $I_{in}(\mathbf{r})$. We can now infer the density profile of the cloud from the ratio of the two images using the Beer-Lambert law for absorption. We always work in the condition $I/I_s \ll 1$, where I_s is the saturation intensity of the atomic transition. In this case the column density of the atomic cloud, i.e. the density integrated along the direction of the imaging beam, can be obtained as

$$n_{2D}(\mathbf{r}) = \frac{\ln(I_{in}(\mathbf{r})/I_{out}(\mathbf{r}))}{\sigma} \tag{3.17}$$

where σ is the scattering cross section for the imaging light at wavelength λ, expressed by

$$\sigma = \frac{3\lambda^2}{2\pi}\frac{1}{1+4\delta^2/\Gamma^2}, \tag{3.18}$$

with Γ the linewidth of the atomic resonance and δ the detuning. All the relevant information about the atomic sample is then deduced by looking at its spatial density profile, either recorded *in-situ*, i.e. with the external trapping potentials still on, or in time-of-flight, i.e. after releasing the atoms and letting them fly in free space.

In order to let the atoms absorb light and produce a shadow on the laser beam, we use the following procedure. We first pulse light at the repumping frequency to excite the atoms in the $F = 2$ state. Then the cooling light makes the atoms cycle on the $F = 2 \rightarrow F = 3$ transition, which provides the needed absorption. During this sequence all magnetic fields have to be off, to avoid that the atomic transitions are shifted by the Zeeman effect.

We can perform absorption imaging along two directions, i.e. from above and from one side of the cell, which allows to reconstruct the three-dimensional profile of the cloud. The magnifications we get are 6.67 for the vertical direction and 3.36 for the horizontal one, with a theoretical resolution of 1 μm for both. The effective resolution is anyway limited by the finite size of the pixels on the CCD camera, which is 6 μm.

Chapter

4

Disordered optical potential: laser speckles

When talking about *speckles* we refer to the random intensity pattern produced by coherent light when it is reflected or diffused by a rough surface. They simply consist in a fine granular pattern of light (see Fig. 4.1) and one could easily come to see them every time a laser beam is around: speckles are somehow inevitable when dealing with coherent light, since any surface is rough on some small enough length scale.

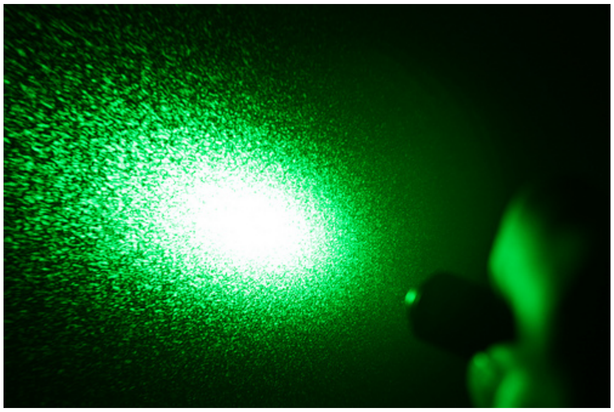

Figure 4.1 | Example of laser speckles produced by laser light reflected by a rough surface.

Speckles are such a widespread phenomenon that lots of physicists run into them, mostly as a trouble, since they introduce undesired noise in the images they deal with and they are usually focused on how to avoid them. In my case, I will take advantage both of the simplicity in producing speckles and of the detailed studies performed about them, to implement *a disordered potential for ultracold atoms*. Thanks to dipole interaction (Sec. 3.1.2), a light pattern shone onto the atoms corresponds to an atomic potential proportional to light intensity. Among all the various possibilities one could think of to produce a random potential, optical speckles offer two main advantages. The first consists in its flexibility on the experimental point of view: it is feasible, and in practice quite easy, to change and control the parameters of the disorder. The second one lies in the possibility of exactly knowing the statistical properties of the potential: they are theoretically well modeled and experimentally measurable.

In this chapter I first introduce some general properties of a speckle potential (Section 4.1). In Section 4.2 I describe the experimental setup I designed to produce it and the *ex-situ* measurements for its characterization. Finally in Section 4.4 I report the *in-situ* calibration performed to test the alignment of the speckle beams on the atoms.

4.1 The speckle field: statistical properties

In order to understand the properties of this disordered pattern of light, let us look at the origin of a speckle field. Consider a laser beam transmitted through a diffuser: take for example a glass plate with a rough surface. The glass plate being rough, the light propagates through a random distribution of depths. The outgoing radiation gains randomly distributed phases along the transverse plane, each grain of the glass surface corresponding to a different optical path for light. All the partial waves produced in this way some up at any spatial position $\mathbf{r}$ after the plate, leading to constructive or destructive interference. This produces a high-contrast pattern of randomly distributed grains of light on every screen placed at any distance from the plate.

Let us make this description a bit more quantitative in order to recover the detailed statistics of the speckle field [49]. This will provide us all the relevant properties of the atomic potential we want to produce. In order to simplify the description, we model the surface of the glass plate as an ensemble of N independent point-like diffusers. The condition for doing this is that the typical transverse size of the grains on the glass surface is much larger than the laser wavelength, $\delta_{glass} \gg \lambda$. Within a region smaller than δ_{glass}, the glass depth does not change significantly and the light diffuses uniformly through it. On the other side, two points on the glass at a distance larger than δ_{glass} give rise to independent scattering events.

The N partial waves arising from the different diffusers have random amplitudes and phases and they interfere, constructively or destructively according to their propagation, in any point of space $\mathbf{r}$. Neglecting possible polarization effects, we consider here what happens to the field amplitude $A(\mathbf{r})$. The field is calculated as the sum of N scattered waves with random amplitudes $a_k/\sqrt{N}$ and phases ϕ_k, i.e.

$$A(\mathbf{r}) = \frac{1}{\sqrt{N}} \sum_{k=1}^{N} a_k e^{i\phi_k}. \tag{4.1}$$

If the roughness of the diffusing surface is such that the scattered partial waves have phases uniformly distributed between 0 and 2π, all the light hitting the surface is diffused and the zero order component cannot be distinguished from all the others. In this situation the speckle field is called *fully developed*. This condition is satisfied in the case of diffusion through a glass plate, if the variance of its depth distribution σ_d is much larger than the laser wavelength: $\sigma_d \gg \lambda$.

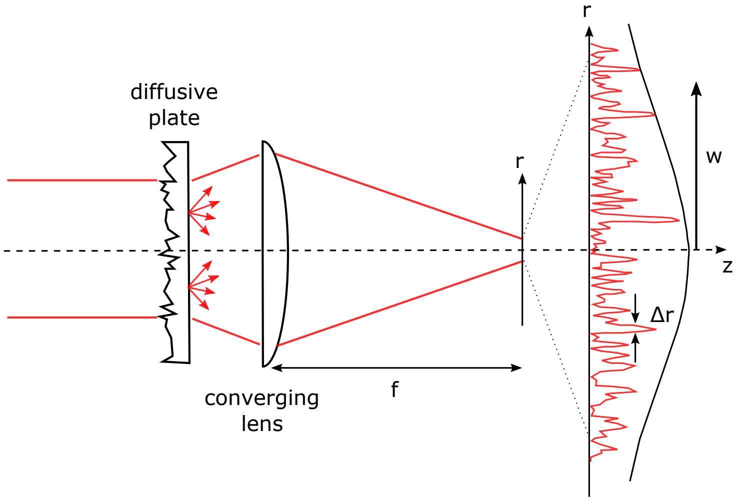

Figure 4.2 | Geometry of the optical system for the production of a focused speckle field. A laser beam transmitted through a diffusive plate is then collected by a converging lens. The speckle pattern that forms on the lens focal plane has width w related to the diffusion angle of the glass plate and correlation length Δr defined by the diffraction limit of the lens.

4.1.1 The intensity probability distribution

Assuming that the phases ϕ_k and the amplitudes a_k in Eq. 4.1 are independent random variables and that the phases ϕ_k are uniformly distributed in the interval $[0, 2\pi]$, the real and the imaginary part of $A(\mathbf{r})$ can be calculated using the Central Limit Theorem. The field amplitude is then the result of a random walk in the complex field, and the amplitude and phase of $A(\mathbf{r})$ are indepedent random variables with a Gaussian probability distribution. From this result we can derive the probability distribution of the field intensity $I = |A|^2$, which has an exponential behavior:

$$P(I) = \frac{1}{\langle I \rangle} e^{-\frac{I}{\langle I \rangle}}. \tag{4.2}$$

From this derives a peculiar property of fully-developed speckle fields: the intensity mean value is equal to its standard deviaton:

$$\sigma_I = \langle I \rangle. \tag{4.3}$$

This implies that the contrast of a speckle field, defined as $C = \sigma_I / \langle I \rangle$ is equal to 1, i.e. maximum.

From Eq. 3.13, we find that the amplitude of the disordered potential V_R is directly related to $\langle I \rangle$ via

$$V_R = \frac{\hbar \Gamma^2}{8\delta} \frac{\langle I \rangle}{I_{sat}} \tag{4.4}$$

where Γ is the linewidth of the atomic resonance, δ is the detuning of the laser from the atomic resonance and I_{sat} is the saturation intensity of the transition.

4.1.2 The spatial properties

Before defining the characteristic length scales of a speckle field, it is necessary to further specify the structure of the optical system we want to study. In the experimental setup we use, we shine a laser beam on a diffusive plate and then focus the scattered light with a converging lens (Fig. 4.2). We are hence interested in the properties of the speckle field produced in the focal plane of the lens. In principle, to reconstruct the final field it would be necessary to study the whole propagation of light, from the diffuser to the lens and then to the focal plane. It is anyway possible to simplify the description, treating the lens pupil itself as the effective scattering source and then studying only the propagation from the lens to its focus. It is proved that the results of this simplified model are equivalent to those for the full propagation [49]. The intensity distribution in the focal plane of the lens is then obtained as the Fourier transform of the laser intensity across the lens.

There are two principal length scales we are interested in: a large one, which is the spatial extension of the whole speckle field, and a fine one, which is the typical size of the light grains in the disordered pattern. Since the field in the focal plane is related to the one on the lens plane by a Fourier transform, the fine details in f are determined by the large scales on the lens, i.e. by the width of the incident beam, while the large scale in f is defined by the fine details on the lens, i.e. by the size of the scattering grains.

The size of "a speckle"

In order to calculate the typical size of the small structures in a speckle field, we define the intensity autocorrelation function

$$\Gamma_I(\delta\mathbf{r}) = \langle I(\mathbf{r}) I(\mathbf{r}+\delta\mathbf{r})\rangle. \tag{4.5}$$

Considering the case of a circular beam of diameter D hitting the scattering surface, it is possible to deduce the expression of $\Gamma_I(\delta\mathbf{r})$ [49]. We decompose the problem on two principal directions, transverse and longitudinal to the light propagation:

$$\Gamma_{I,\perp}(\delta r_\perp) = \langle I\rangle^2 \left| \frac{2\lambda f}{\pi D \delta r_\perp}\, J_1\left(\frac{\pi D \delta r_\perp}{\lambda f}\right)\right|^2 \tag{4.6}$$

$$\Gamma_{I,\|}(\delta z) = \langle I\rangle^2 \,\mathrm{sinc}^2\left(\frac{D^2 \delta z}{8\lambda f^2}\right) \tag{4.7}$$

where $J_1(x)$ is the Bessel function of the first kind.

We define the *correlation length* as the position of the first zero in the autocorrelation function. We obtain:

$$\Delta r_\perp = 1.22\,\frac{\lambda f}{D} \tag{4.8}$$

$$\Delta z = 8\,\frac{\lambda f^2}{D^2} \tag{4.9}$$

It is interesting to note that the transverse size of the speckles corresponds to the diffraction limit of the lens. It is also apparent that the longitudinal size is much larger than the transverse one, each speckle looking like a sort of "tube". We will need to consider this strong anisotropy when designing the experimental setup.

The extension of the speckle field

The width of the speckle field depends on the diffusion angle of the scattering surface. Due to the phenomenon of diffraction, the angle of the light cone emitted by each scattering point depends on the size of the scatterer itself: $\theta \propto \lambda/\delta_{glass}$. The envelope of the speckle field in the focal plane of the lens is hence determined by the diffusion angle of the glass plate and by the numerical aperture of the lens.

4.2 Experimental setup for a 3D disordered potential

When thinking of how to design the experimental setup for the production of the disordered potential, we had to take into account some basic, though crucial, requirements.

- First of all, we want to realize a *three-dimensional* disorder for the atoms. This means that the correlation lengths of the potential along the three axes need to be comparable with the de Broglie wavelength of the atoms, so that they undergo random scattering events in all directions.

  The typical temperature of the atoms in our experiment is of the order of 10 nK, so that the de Broglie wavelength λ_{dB} is of the order of few μm. As shown in Eq. 4.8, the transverse correlation length $\Delta r_\perp$ of the speckle field is determined by the diffraction limit of the converging lens. Given the optical access on the atoms and the laser wavelengths we despose of, a $\Delta r_\perp$ of the order of few μm is easily achievable. As already noticed, the spatial correlations of the speckle field are strongly anisotropic, and the longitudinal correlation length Δz we can experimentally achieve is of the order of few tens of μm, hence $\sim$10 λ_{dB}. We then need to reduce it. To this purpose we decided to implement the same experimental scheme already used in [36], where two coherent speckle fields crossing at 90° are used. Interference fringes cut the speckle tubes on a plane at 45° with respect to the longitudinal axes of the beams. The resulting correlation lengths are of the correct order of magnitude along all directions (see Sec. 4.3.2).

- To achieve Anderson localization we need *strong* disorder.

  Of course we do not know *a priori* the position of the mobility edge, but it is expected to be of the same order of the disorder amplitude V_R. To obtain significant localized fractions we thus need to reach values of V_R that exceed the mean energy of the atoms. The laser wavelength and the maximum intensity we can have on the atoms are such that V_R/k_B can be tuned from 0 to 100 nK.

- The disordered potential has to be *homogeneous* on the whole volume occupied by the atoms, so that we can assume a uniform disorder strength.

  The typical distance on which the atoms propagate during the experiment is of the order of few hundreds of μm. We thus need that the Gaussian envelope of the single speckles has a width of the order of 1 mm, so that the average light intensity is effectively flat on the region occupied by the atoms. This constraint has been taken into account in the choice of the diffusion angle of the glass plates and in the design of the whole optical paths for the two beams.

- *Spurious localization effects* different from Anderson localization have to prevented.

  The main “classical localization” effects that could mask the quantum AL are classical percolation and trivial trapping in single deep potential wells. The probability of localization via classical percolation is strongly reduced by using blue-detuned speckles. In this case the potential is repulsive and the atoms are attracted by the low intensity regions. Thanks to the high probability of low I in a speckle pattern, the percolation threshold is then found around $4 \cdot 10^{-4} V_R$, hence much smaller than the energy scale of the mobility edge [50]. We then tune the wavelength of laser light to the blue side of the transition, namely at $\lambda = 762$ nm. Trivial trapping in the single speckle wells is reduced by suitably tuning the ratio between the disorder amplitude V_R and the correlation energy $E_R = \hbar^2/m\sigma_R^2$, where m is the atomic mass and σ_R is the average correlation length. If $V_R/E_R < 1$, a typical well is to weak to bind a particle. In our experiment we can explore a broad range of V_R, passing from a regime where the spatial correlations of the disorder are not relevant to that where they start to play a role.

The optical system we designed for the production of our 3D disordered potential is reported in Fig. 4.3.

4.3 Ex-situ characterization of the potential

The first characterization of the disordered potential is performed *ex-situ*. We mounted the whole optical system far from the atoms and imaged the intensity distribution in order to measure: 1) the spatial extension of the potential at the position of the atoms; 2) the correlation lengths; 3) the probability distribution of the intensity.

4.3.1 Spatial extension of the disordered potential

We image the single speckle patterns on a plane transverse to their propagation direction by placing a CCD camera in front of the last lens. We also place a glass 4 mm thick between the lens and the camera, so that we can simulate the effect of the glass cell in the experiment. The glass used here is exactly the same kind of glass used for the cell. We use it for all the measurements in this section. The camera is mounted on a micrometric translation stage, so

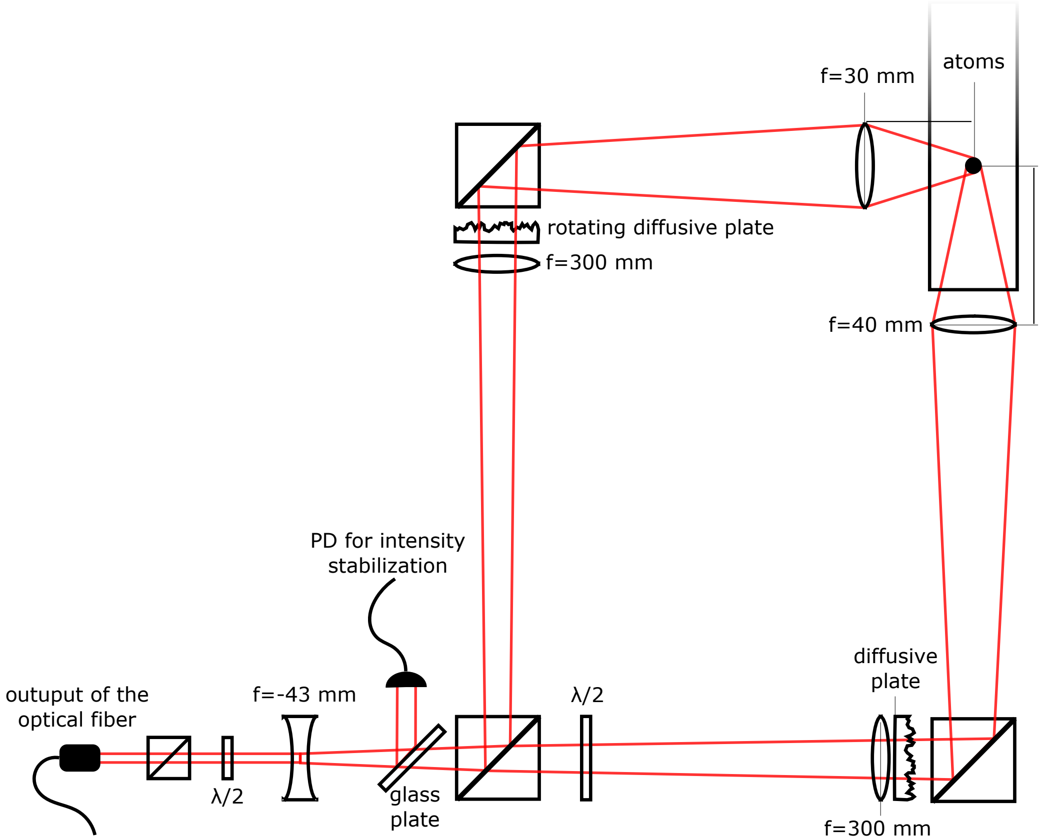

Figure 4.3 | Optical setup for the production of the disordered potential. The light emitted from the Ti-Sa laser (see Sec. 3.3.3) is injected into an optical fiber that brings it on the experiment table. At the output of the fiber a first polarizing beamsplitter cleans the light polarization. A $\lambda/2$ waveplate and the next polarizing cube are used to split the light in two beams of equal intensities. Both of them go through a diffusive plate that originates the speckle pattern. A last polarizing cube for each branch is then used to reflect the speckle light towards the atoms. Along the light path a number of diverging and converging lenses are placed to adjust the beam waists on the two crucial positions, i.e. on the final lenses and on the atoms. The size and the divergence of the beams on the final lenses indeed determine the speckles correlation lengths and the width of the speckle envelope respectively. The optical paths are designed in such a way that the statitical properties in the focus of the two beams are as similar as possible, even if the last lenses have to be placed at different distances from the atoms. A glass plate, placed before the bifurcation of the two beams, sends a small amount of light to a photodiode, which is used for the intensity stabilization of the laser. Note that one of the diffusive plates is mounted on a mechanical rotating stage which allows to change the disorder configuration at every experimental run.

that we can move it along the propagation direction of the beam and look for the position of minimum waist, that is the position where we want to place the atoms in the final configuration. There we record an image of the speckle field, as reported in Fig. 4.4 **b**. We integrate the two-dimensional intensity distribution along the two directions and fit the one-dimensional profiles with a Gaussian. We repeat the same procedure for both beams. We measure the beam waists as the width of the Gaussian at $1/e^2$ and we obtain: $w_1 = 1305(10)\ \mu$m and $w_2 = 1306(10)\ \mu$m.

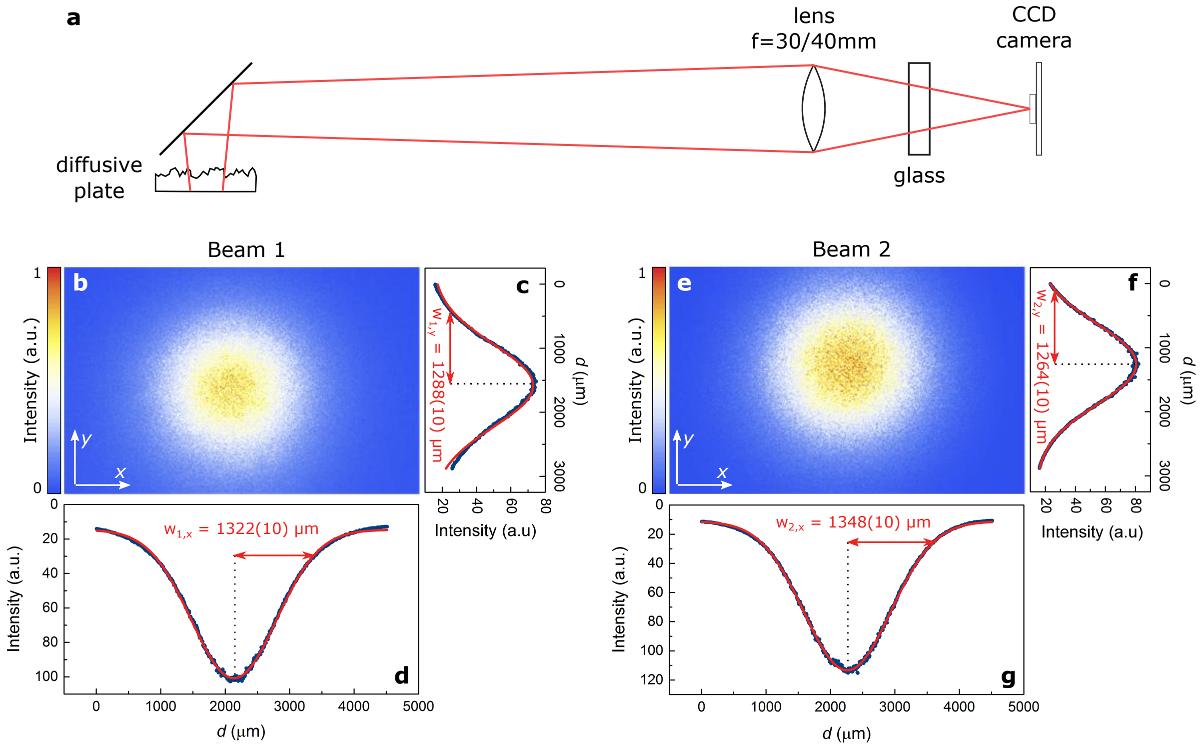

Figure 4.4 | Gaussian envelope of the speckle beams. a) Scheme of the imaging system to measure the spatial extension of the single speckle beams. **b,e)** Image of the speckle patterns in their focus position. In **c,f** and **d,g** are reported the 1D profiles obtained as the integral of the intensity along x and y respectively (blue dots) and the corresponding Gaussian fits (red lines). The widths of the beams along the two directions are extracted from the fit and then averaged to obtain the values of w_1 and w_2 reported in the text.

4.3.2 Correlation lengths

Correlation lengths of the single speckle beams

In order to detect the fine structure of the speckles, we need to use a different imaging system with a higher resolution. To this purpose, we use a telescope made of a microscope objective with a working distance of 17 mm and a converging lens with focal length $f = 150$ mm. The magnification we obtain is 35x. We place the microscope objective a working distance away from the focus of the speckle beam, so that we can study the fine structure of the speckle pattern at that position. In Fig. 4.5 we report a typical image of the speckles recorded with this optical setup. From these images we calculate the spatial autocorrelation function of the intensity, as reported in Fig. 4.5 **c,d**. We fit it with the theoretical profile $\Gamma_I(\delta r_\perp) = A\big[\frac{\xi}{\pi}\frac{1}{\delta r_\perp}J_1(\frac{\pi}{\xi}\delta r_\perp)\big]^2$, where the amplitude A and the width ξ are free parameters and $J_1(x)$ is the Bessel function of the first kind. From the position of the first zero in the autocorrelation functions $\Delta r_{\perp 1}$ and $\Delta r_{\perp 2}$ we deduce the transverse correlation lengths of the two speckles $\sigma_{\perp 1} = \Delta r_{\perp 1}/\pi = 0.73$ μm and $\sigma_{\perp 2} = \Delta r_{\perp 2}/\pi = 0.8$ μm.

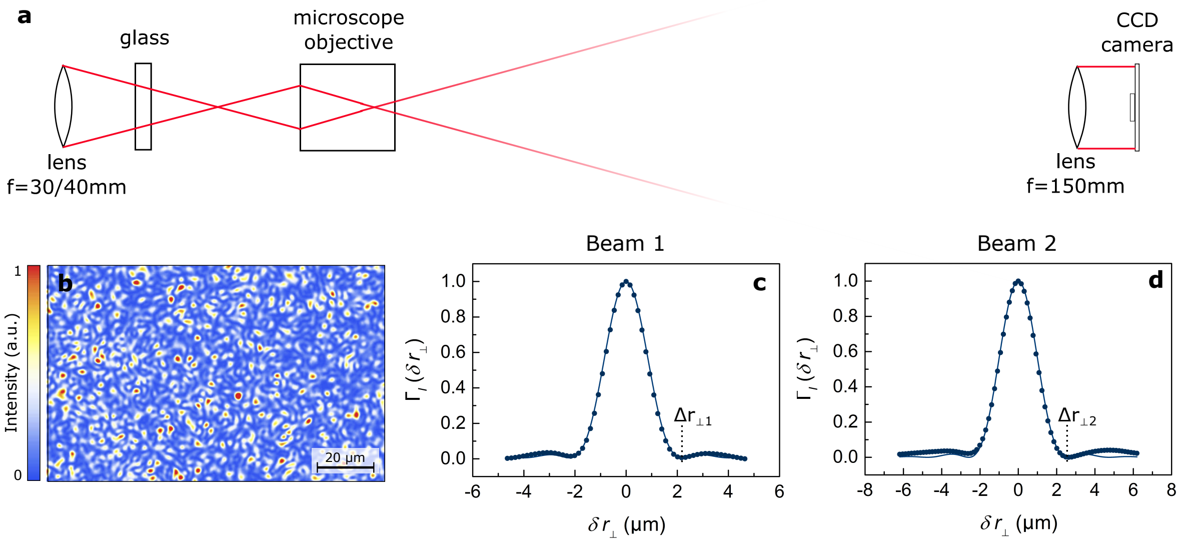

Figure 4.5 | **Autocorrelation function of the speckles. a)** Scheme of the imaging system to measure the small details in the speckle pattern. **b)** Example of a picture of the speckle pattern taken with the high resolution imaging system. **c, d)** The measured autocorrelation functions for the two speckle beams (blue dots) are fitted with the theoretical profile (blue lines).

Correlation lengths of two interfering speckles

After characterizing the properties of the single speckles, we want to study the behavior of two interfering speckle patterns. We let the two speckle beams cross at an angle $\theta = 50°$ and we place the microscope objective parallel to the interference fringes, i.e. along the y axis (as showed in Fig.4.6 **a**). In this way we record images as the one reported in Fig.4.6**b**, where one can clearly see how interference effectively reduces the size of the grains in the disordered pattern. Although the angle used here is different from the one we chose for the final configuration on the atoms, this measurement allows us to verify that the autocorrelation function along the x direction has the expected profile. We could not do the measurement with the correct angle of 90° because of the limited numerical aperture of the microscope objective we use. In Fig.4.6**c** we report the measured autocorrelation of the intensity along the x direction and the fit with $\Gamma_I(\delta y) = A\big[\frac{\xi}{\pi}\frac{1}{\delta y}J_1(\frac{\pi}{\xi}\delta y)\cos(\frac{4\pi\delta y}{d})\big]^2$, where the amplitude A, the width of the Bessel function ξ and the periodicity of the interference fringes d are free parameters. From the fit we measure $d = 1.1(1)$ μm, which is in agreement with the calculated distance between two interference minima $d = \lambda_{laser}/2\sin(\theta/2) = 1.0$ μm (the laser wavelength during this characterization stage is $\lambda_{laser} = 810$ nm). The agreement observed allows us to deduce the correlation length of our potential along the x direction from the theoretical interference pattern at the correct angle of 90°.

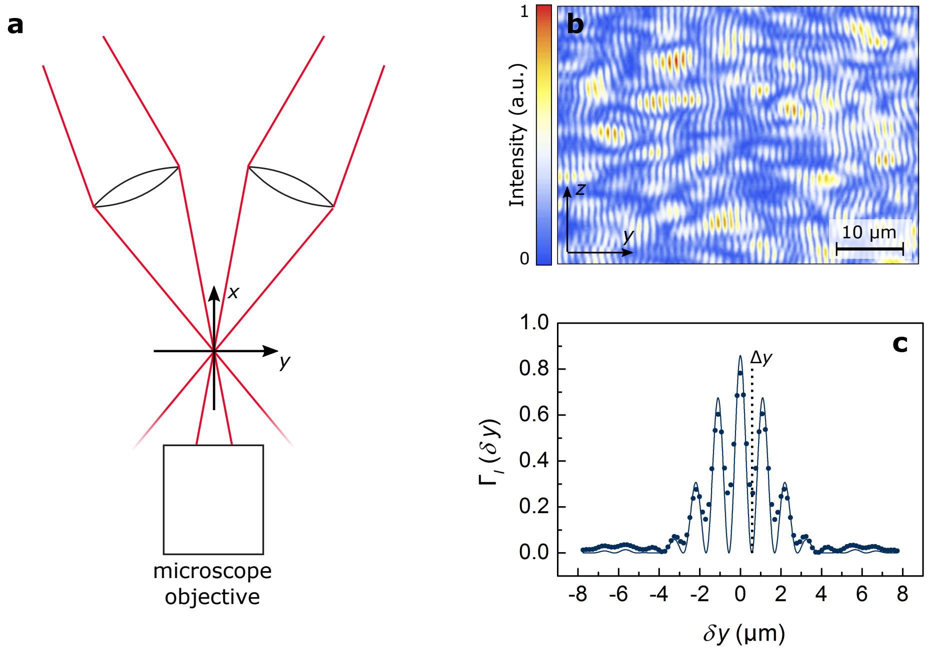

Figure 4.6 | **Interfering speckles. a)** Scheme of the optical system used to measure the correlation length of two interfering speckles. **b)** Image of the interfering speckles on the y, z plane. **c)** The measured intensity autocorrelation $\Gamma_I(\delta y)$ (blue dots) is fitted with the theoretical profile (blue solid line).

Resulting correlation lengths of the 3D potential

Given the results of the measurements reported above, we can deduce the correlation lengths of the disordered potential generated with the optical scheme of Fig. 4.7. The principal axes of the problem are taken as showed in Fig.4.7**a**. In the y direction, where interference fringes split the speckles into smaller substructures, the first zero in the correlation function Δ_y is given by half the distance between two interference minima, so that $\sigma_y = \Delta y/\pi = \lambda/(2\sqrt{2}\pi) = 0.09$ μm. Along z we calculate the average of the transverse correlation lengths of the two speckles $\sigma_z = (\sigma_{\perp 1} + \sigma_{\perp 2})/2 = 0.76$ μm, while σ_x is the projection at 45° of the same average: $\sigma_x = \sigma_z\sqrt{2} = 1.08$ μm. From the geometric average on the three directions we get $\sigma_R = 0.41$ μm.

4.3.3 Intensity distribution

In order to measure the probability distribution of the intensities in the single speckle patterns, we use the same optical setup as in Fig. 4.5 **a**, i.e. the one with the higher resolution. From the images as in Fig. 4.5 **b** we measure the probability distribution as reported in Fig. 4.8. We find the expected exponential decay as in Eq. 4.2. The deviation from the exponential fit at low intensities is due to the finite resolution of the imaging system.

As for the two interfering speckles, $P(I)$ is predicted to preserve the same exponential distribution with $\langle I_{tot}\rangle = \langle I_1\rangle + \langle I_2\rangle$, where $\langle I_{1,2}\rangle$ are the average intensities of the single speckles

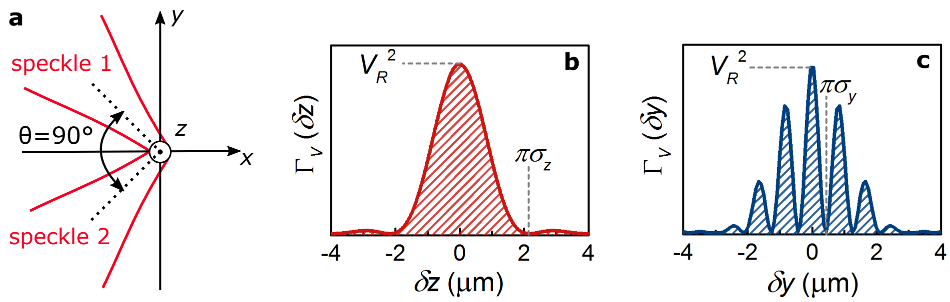

Figure 4.7 | **Spatial correlations of the 3D speckle potential. a)** Geometry of the 3D speckle potential. The two speckle beams cross at the atoms position with an angle θ =90°. Interference fringes are parallel to the x axis. We report here the calculated autocorrelation function along two axes. **b)** Autocorrelation function along the z axis: it has the typical profile of the single speckle correlation function on its transverse plane. The correlation length σ_z results from the average of the transverse correlation lengths of the two speckles. The autocorrelation function along the x axis follows the same profile, but it has a larger correlation length σ_x resulting from a projection at 45° of σ_z. **c)** Autocorrelation function along the y axis: interference fringes add up to the usual Bessel type profile and reduce the resulting correlation length σ_y, calculated as half the distance between two interfering minima.

[49]. An angle $\Delta\theta$ between the polarizations of the two speckles would reduce the contrast in the interference and hence modify $P(I)$ at low I. Considering the geometry of our experimental setup, we estimate $\Delta\theta < 5°$. For small $\Delta\theta$, the position of the maximum in $P(I)$ is expected to move to $\Delta\theta^2/4\ \ln(4/\Delta\theta^2)\langle I_{tot}\rangle$, which in our case corresponds to $\sim 0.01\langle I_{tot}\rangle$. Such a small modification is not expected to affect the localization properties of the system, since the typical energies in the experiment range from $V_R/2$ to V_R, hence far from this low I region.

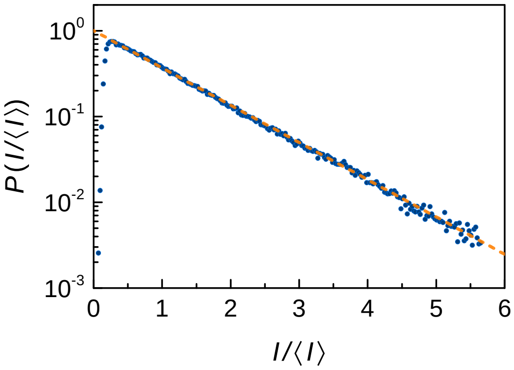

Figure 4.8 | **Measured intensity distribution of a speckle pattern.** Blue dots represent the measured $P(I)$ in a single speckle field imaged on its transverse plane at the focus position. Data are fitted with an exponential function (orange dashed line).

4.4 In-situ calibration of V_R

The mean amplitude of the disordered potential V_R is first computed from the light intensity of the speckles, obtained from the measurement of the spatial envelope of the individual speckles (as reported in Sec. 4.3.1) and of their total optical power. For this optical calibration V_R^{opt} we estimate a relative uncertainty of 10%. After placing the optical system for the production of the speckles on the experiment table, we wanted to perform an *in-situ* calibration of V_R. Whatever misalignment of the speckles light on the atoms would indeed produce a deviation of V_R with respect to the expected value V_R^{opt}. The *in-situ* calibration is deduced from a study of the dynamics of the atoms. Since our 3D disorder is the superposition of two separate speckle patterns, we calibrate them independently. We apply a short pulse of the speckle potential to a non-interacting condensate in free expansion, and we measure its final momentum distribution. Using a single speckle beam at a time, the problem is effectively 2D, being the longitudinal correlation length much longer than the atomic displacement on the short time scale we consider (see Sec. 4.1.2). We observe the formation of a bimodal momentum distribtion (Fig. 4.9), meaning that only a fraction of the atoms gets accelerated by the pulse. From a 2D numerical simulation we indeed observe that the momentum distribution should develop a high-energy component , with a mean kinetic energy transferred by the speckle pulse $\Delta E_{kin} = 0.19(2) V_R$. The behavior we observe in the experiment is in agreement with the simulations. The evolution of E_{kin} of the excited part is approximately linear with V_R^{opt}, with a slope within 17% of the theoretical one. This confirms the validity of the optical calibration. The values of V_R I report from this point on will always correspond to the calculated V_R^{opt}.

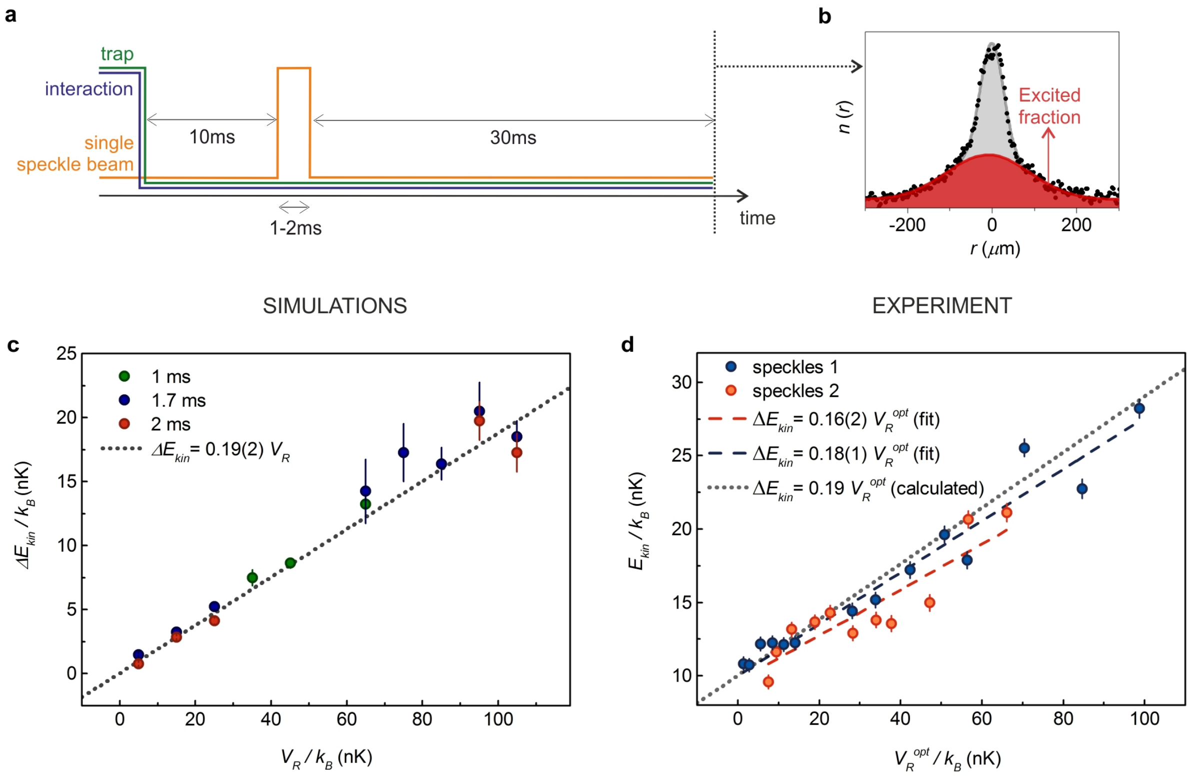

Figure 4.9 | **Calibration of V_R. a)** Scheme of the experimental sequence used for the calibration measurements. We switch off the dipole trap and reduce the interaction strength to zero, we let the atoms expand for 10 ms in free space and then we pulse the light of a single speckle beam for 1 or 2 ms. We let the atoms expand for another 30 ms and finally we image the cloud. A typical 1D profile of the atomic density is reported in **b)**. In the bimodal profile we can distinguish a central unpertubed fraction of atoms (grey) and an excited one (red). In **c** are reported the kinetic energies gained by the excited fraction as a function of the disoder amplitude, as obtained in the simulations. Different colors correspond to different durations of the speckle pulse. All the data are on the same line which corresponds to $\Delta E_{kin} = 0.19(2) V_R$. In **d** I show the measured kinetic energy of the excited fraction for the two speckle beams (blue and orange circles). The dashed orange and blue lines correspond to the linear fits of the two datasets. The grey dotted line is the one obtained from simulations. The fitted lines are compatible with the simulated one within the 17%.

Chapter

5

3D Anderson localization and measurement of the mobility edge

In Chapters 3 and 4 I introduced the two main characters of this experiment, which are the *non-interacting matter waves* and the *disordered optical potential*. We are now ready to get to the heart of our topic and observe how the atoms behave when moving in a disordered environment. The main results is this chapter are published in [51].

As I introduced in Chapter 2, in order to perform a study about Anderson localization, the crucial issue lies in the ability to control and measure the energy distributions both of the disordered potential and of the atoms. In the present Chapter I will present the results concerning the measurement of the mobility edge, first introducing step by step the strategy employed to achieve the goal. In Section 5.1 I describe the procedure we designed to load the atoms in the low-energy states of the disordered Hamiltonian. In Section 5.2 I describe the measurements we performed to detect the onset of localization and provide a characterization of it. In Sections 5.3 and 5.4 I report the strategy we implemented to determine the energy distribution of the atoms and the spectroscopic technique used to locate the threshold for localization. In Section 5.5 I present the results about the mobility edge and compare them with available theoretical predictions. Finally, in Section 5.6 I report some preliminary results about the effects of finite interactions on the localization problem.

5.1 Preparation of low-energy states

The first crucial step in an experiment about AL concerns the preparation of the atomic sample inside the disorder. AL affects the atoms in the low-energy eigenstates of the disordered Hamiltonian. The main requirement to observe the phenomenon is then the ability to populate the lowest states of the energy spectrum, which is far from trivial.

In order to transfer the atoms in the disorder, we have to change the external potential from the harmonic confinement of the dipole trap where we produce the BEC (Sec. 3.4) to the speckle potential. A proper adiabatic process that transfers the atoms from the initial to the final ground state cannot be realized. This is somehow inevitable when dealing with disordered systems, since the ground state of the disordered Hamiltonian could be placed far away from the initial position of the atoms, so that they cannot reach it in a finite time. Although it is not possible to load the atoms in the lowest energy states for every possible configuration of the speckles, we have studied how to perform a *quasi-adiabatic* process that minimizes the final energy of the atoms. This can be done by exploiting the tunability of the interactions. The idea is to use a finite repulsive interaction while changing the external potential, so that the coupling between the initial and the final eigenstates is increased and the atoms can explore a larger region of the phase-space. In particular we slowly switch on the speckle potential while we ramp down the dipole trap and reduce the interaction strength to zero. In order to optimize this loading procedure we measure the final kinetic energy of the cloud and try to minimize it. The resulting sequence consists in a linear increase of V_R in 100 ms, a linear decrease of the trap strength to zero in 200 ms and a decrease of the interaction strength proportional to $1/t$ down to a scattering length $|a| \leqslant 0.2\ a_0$ in 200 ms, all the three ramps starting at the same time (see Fig. 5.1).

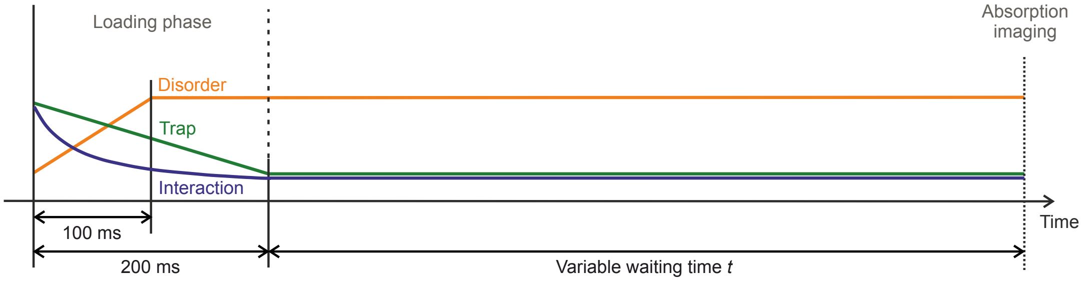

Figure 5.1 | Experimental sequence to load the atoms in disorder and detect the onset of localization. The loading phase consists of two linear ramps to switch on the speckle potential and switch off the trapping beams, and a $1/t$ ramp to reduce the scattering length to zero. In the following variable waiting time the atoms are free to move in the disordered potential. After that we perform absorption imaging to detect the intensity distribution $n(r,t)$.

5.2 Evidence of localization

5.2.1 Expansion in the disordered potential

At the end of the loading sequence, the harmonic potential is off and the atoms are free to expand in the disordered environment realized by the speckles. To investigate their transport properties, we record the atomic density distribution after a variable waiting time t via absorption imaging. We can image the cloud along two orthogonal directions as described in Sec. 3.5, which allows to reconstruct the dynamics along the three orthogonal axes of Fig. 4.7. In order to simplify the discussion, I will first present the results relative to the expansion along a single axis, namely x, and then discuss the behavior along the other two.

We consider the images taken from the vertical imaging direction, i.e. along z, and we reconstruct the one-dimensional profile $n(x)$ from the integration along y. We measure the second moment of the distribution $\langle x^2 \rangle = \int x^2 \; n(x) \; dx$. The time evolution of $\langle x^2 \rangle$ is reported in Fig. 5.2 for some typical values of V_R. The measurements reported there are averaged over different realizations of the disorder, obtained by rotating in steps one of the diffusive plates creating the speckles (see Fig. 4.3). We found that 5 realizations are typically enough to obtain stationary results, presumably because each sample contains a relatively large number of states, resulting in a self-average. By increasing the disorder strength V_R, we observe the transition between two extreme transport regimes. For the smallest values of V_R the second moment of the distribution scales linearly with time, which is a signature of diffusive behavior (see Sec. 2.2.3). The data for $V_R/k_B \leq 8$ nK are hence fitted with $\Delta\langle x^2(t)\rangle = \langle x^2(t)\rangle - \langle x^2(0)\rangle = 2Dt$, where D is the diffusion coefficient. The opposite situation occurs for the largest $V_R/k_B = 94(9)$ nK, where, after a small initial increase, $\Delta\langle x^2(t)\rangle$ saturates to a fixed value, indicating that the sample is fully localized. For intermediate values of V_R there is an apparent deviation from the pure diffusive behavior, but no clear saturation of $\langle x^2 \rangle$ is detected. This suggests that the atoms occupy the spectrum of the disordered Hamiltonian with a finite energy distribution: some of them lie below the mobility edge and, after a variable transient time, they reach a steady configuration, not contributing to any further increase of $\langle x^2 \rangle$; another fraction of the atoms is instead above the mobility edge and keeps on expanding, though very slowly.

This first qualitative discussion about the results reported in Fig. 5.2 allows to draw some first conclusions:

- The experimental setup and the loading procedure we implemented are able to achieve 3D Anderson localization of ultracold atoms.
- By increasing the disorder strength V_R, we are able to move the position of the mobility edge with respect to the energy distribution of the atoms, allowing to pass from diffusion to full localization.

Let me briefly note that these first results represent one of the crucial improvements with respect to previous experiments about 3D AL with ultracold atoms [35, 36]. The implementation

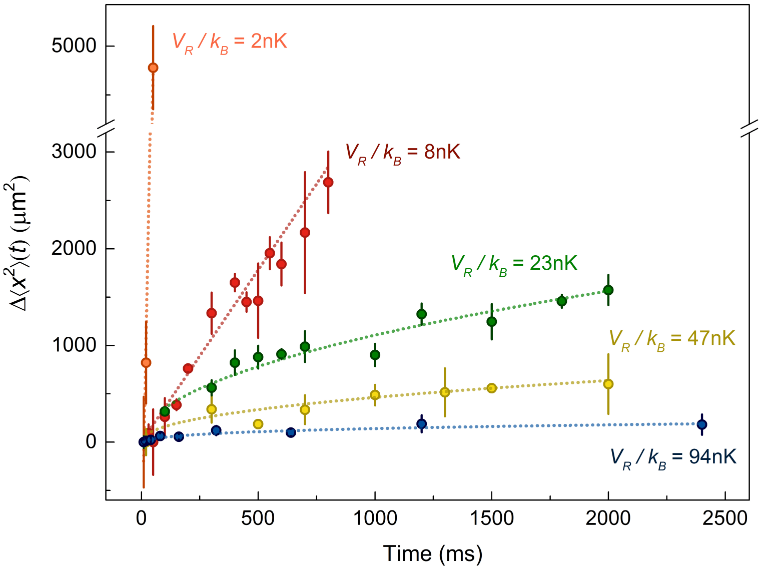

Figure 5.2 | Expansion in the disordered potential. The time evolution of $\Delta\langle x^2\rangle$ is reported for different disorder strengths. The error bars represent the statistical uncertainty and correspond to one standard deviation. Dotted lines correspond to a linear fit for $V_R/k_B = 2$, 8 nK and are a guide to the eye for the largest V_R.

of a quasi-abiabatic switching on of disorder allows to control much better the energy distribution of the atoms and to obtain large localized fractions, in contrast for example with the situation of [36], where the speckle potential had to be instantaneously switched on. The main difference lies in the possibility of tuning the atomic interactions, provided by the optimum scattering properties of ^{39}K.

5.2.2 Onset of a quantum transport regime

A quantitative analysis of the short-time dynamics in Fig. 5.2 provides a further proof of the onset of localization. We perform a linear fit of the evolution of $\langle x^2\rangle$ on the first 300 ms and we extract an initial diffusion coefficient D. The results are reported in Fig. 5.3. The breakdown of the linear diffusive behavior observed for $V_R/k_B > 8$ nK corresponds to an abrupt reduction of D below $\hbar/3m$, which is the transport regime where quantum interference is predicted to suppress diffusion and lead to localization [50].

5.2.3 Time evolution of the density profiles

The physical quantities discussed so far, i.e. $\langle x^2(t)\rangle$ and D, provide information about the behavior of the system necessarily averaged over the whole energy distribution. It is then interesting to give a closer look to the time evolution of the density profiles $n(x)$, since it allows to distinguish different transport regimes inside the same atomic sample. We take as an exemplary case the evolution for V_R/k_B =47(5) nK, which is reported in Fig.5.4. The central part of the cloud is

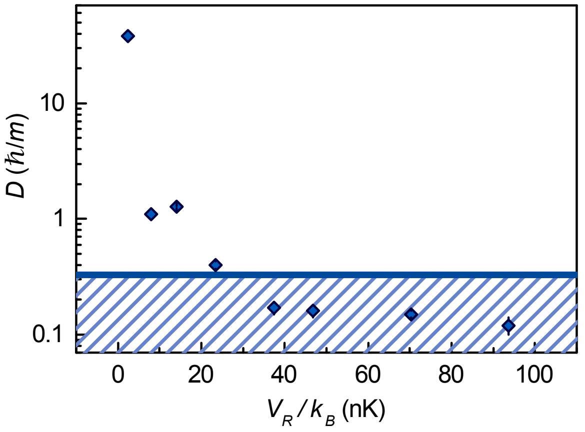

Figure 5.3 | Initial diffusion coefficient. The values of D reported here are obtained from a linear fit of $\Delta\langle x^2\rangle(t)$ in the first 300 ms. The blue region corresponds to the limit of quantum transport, achieved when $D \leq \hbar/3m$. The onset of the quantum regime at $V_R/k_B \sim 20$ nK correponds to the breaking of diffusive transport in Fig. 5.2.

essentially stationary, while the tails expand in the first one second and then reach a steady configuration. The localization length being a function of the energy, the different energy states in the cloud spread on different length scales and the localization time scales accordingly. This observation confirms the coexistence of many energy states at different distances from the mobility edge and it allows to better understand the evolution of $\langle x^2\rangle$ in the region of intermediate disorder.

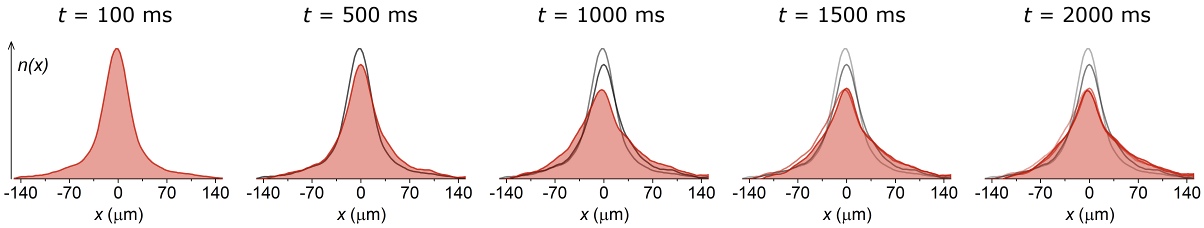

Figure 5.4 | Time evolution of the density profiles. The atomic density $n(x,t)$ at $V_R/k_B = 47(5)$ nK is reported. Grey lines on the background correspond to the profile at earlier times.

5.2.4 Localization lengths

The coexistence of a large number of energy states makes it quite difficult to measure localization lengths, since they are properly defined only for the single energy states. It is anyway interesting to estimate the order of magnitude of the localization lengths in our sample by fitting the tails of the distribution $n(x)$ at large time. Since the predicted profile for an Anderson localized state is an exponential (see Sec. 2.2.3), we fit the one-dimensional profiles with the integral along two directions of a 3D exponential function with localization length l: $n(x) = 2\pi l^2\ \Gamma(2, |x|/l)$, where

$\Gamma(n,x)$ is the incomplete gamma function of order n. We consider the same example of Fig.5.4 for $V_R/k_B = 47(5)$ nK and we fit the tails of the profile at $t = 1000$ ms. By fitting separately the left and the right tails of the distribution we obtain $l_R = 32(1)$ μm and $l_L = 28(1)$ μm (see Fig. 5.5).

Notice that this estimation of l might be affected by the presence of rather long tails even in the initial spatial distribution (see the profile at t=100 ms), which are probably due to the quasi-adiabatic loading procedure we use: during the slow ramps we use to switch from the harmonic trap to the speckle potential, the most energetic atoms start expanding and occupy the large tails of the spatial distribution visible in Fig. 5.4. This means that the values of l we obtained should be considered more appropriately as an upper bound to the effective localization length. Anyway, we are simply interested in using this result as a basis for rough comparison with theory. In Ref. [52], self-consistent theory is applied to a disordered potential similar to ours, created by two interfering laser speckles. The localization legth is predicted to change from about $l \sim \sigma_\perp$ around $E_c/3$ to $l \sim 100\sigma_\perp$ above $5/6$ E_c, where $\sigma_\perp$ is the transverse correlation length of the individual speckle patterns and E_c is the mobility edge. The localization lengths we measured correspond in our case to $l \sim 30\sigma_\perp$. This seems to be the right order of magnitude, since for this value of V_R we observe an initial evolution of the cloud at short times and a very slow increase of its size for longer times, which might be justified by a finite, though small, energy distribution close to E_c.

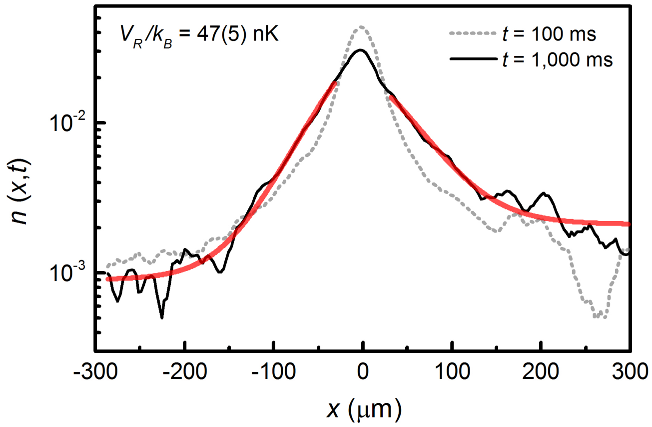

Figure 5.5 | Estimation of the localization length. The black solid line corresponds to the density profile at $V_R/k_B = 47(5)$ nK after 1 s, while the grey dotted profile is the initial one at 100 ms. The red lines correspond to the independent fits performed on the left and right tails of the distribution at the longer time.

5.2.5 Expansion along three spatial directions

Due to the anisotropy in the spatial correlations of the speckle potential (Sec. 4.3.2), we expect to see a difference in the dynamics of the atoms along the three spatial directions. To estimate this effect, we look at the time evolution of the squared width of $n(\mathbf{r})$ along the three axes for an intermediate value of the disorder amplitude, where the dynamics is still clearly visible. We choose $V_R/k_B = 23(2)$ nK (see Fig. 5.6). At short times the system expands both along x and z, eventually reaching a larger size along x, where the disorder correlation length is a factor $\sqrt{2}$ larger than along z. Along y we observe just a slight increase of the width. This is consistent with the fact that the cloud is initially larger along this direction, due to the anisotropy of the dipole trap, and the correlation length of the speckles is much smaller. The behavior we observe is then justified by the fact that shorter correlation lengths correspond to stronger disorder, thus to shorter localization lengths and slower dynamics.

In order to have the highest sensitivity to changes in the diffusion/localization evolution, we consider for simplicity the behavior along x, where the dynamics is more prominent, knowing that the behavior on the other directions is equivalent to the first except for a scaling factor.

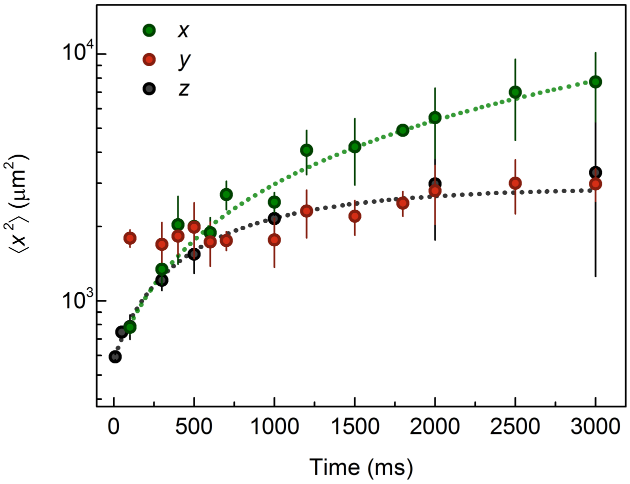

Figure 5.6 | Expansion along three directions. The time evolution of $\langle x^2 \rangle$ (green), $\langle y^2 \rangle$ (red) and $\langle z^2 \rangle$ (black) is reported for $V_R/k_B = 23(2)$ nK. The error bars represent the statistical uncertainty and correspond to one standard deviation. Dotted lines are guides to the eye.

5.3 Energy distribution of localized samples

Studying the evolution of the atomic cloud in the disordered potential has demonstrated the occurrence of partial or full localization in a certain range of V_R. To reach the goal of measuring the mobility edge, we need to determine the energy of the atoms, so as to infer the relation between the energy distributions and the localized/diffusive behavior observed. In cold atoms experiments it is possible to measure the kinetic energy of the atoms, but determining their potential energy is a more difficult task. The potential term is indeed usually calculated from the knowledge of the external potential applied to the atoms, as it can be easily done in the case of harmonic traps. Dealing with disordered potentials makes it impossible to follow the same procedure, since we have no direct access to the exact properties of the light pattern seen by the atoms for each configuration of the disorder. On the other hand it is the total energy of the atoms, i.e. the sum of the kinetic and potential terms, that is relevant for the determination of the mobility edge. We hence designed a novel technique for the determination of the energy distribution, which combines experimental measurements and numerical calculations to reach the purpose. The idea is the following. We measure the momentum distribution of the atoms $n(k)$ through the standard time-of-flight imaging technique. We perform a numerical study of the low-energy eigenstates of our disordered Hamiltonian to calculate the spectral function $\rho(E,k)$, which represents the probability for a state at energy E to have momentum k. Finally we combine this two quantities to deduce the average occupation probability of the energy states $f(E)$, since they are related to each other by $\int \rho(E,k) f(E)\ dE = n(k)$. The energy distribution is then determined as $n(E) = \int \rho(E,k) f(E)\ dk$, i.e. by multiplying the occupation probability $f(E)$ by the density of states $\int \rho(E,k)\ dk$. In the rest of this Section I go through the method outlined here, presenting it step by step.

5.3.1 Measurement of the momentum distribution

The experimental measurement of the momentum distribution is performed with the standard technique of recording the atomic density of the atoms in time of flight, i.e. as they expand in free space. The study of their expansion when released from every external potential indeed allows to determine their initial momenta. In our case, we load the atoms in the disordered potential with the same procedure depected above (Sec. 5.1) and then we switch off the speckles and perform absorption imaging at two different times of flight t_1 and t_2. In Fig.5.7 **a** I report the 1D profiles of the cloud for V_R/k_B=47(5) nK. The momentum distribution is deduced from the two density distributions using a deconvolution procedure. The spatial density at the longer time t_2, integrated along y and z, is given by $n(x,t_2) = \int dk\ dx_1\ n(x_1,t_1)\ n(k)\ \delta(x - x_1 - \frac{\hbar k}{m}(t_2 - t_1))$, where $k = k_x$ and $n(k)$ is the momentum distribution integrated along k_y and k_x. We have assumed the momentum and spatial distributions to be factorizable, since the system occupies a large number of states and we can reasonably assume that there are no relevant correlations in the average distributions. We found that using a Gaussian form for $n(k)$ well reproduces the data. We then substitute $n(k) \propto \exp(-k^2/(2\sigma^2))$ in the previous formula and we get

$$n(x,t_2) = \int dx_1\ n(x_1,t_1) \exp\Big[-\frac{1}{2}\Big(\frac{m(x-x_1)}{\sigma(t_2-t_1)}\Big)^2 \Big]. \tag{5.1}$$

Including the experimental $n(x_1,t_1)$ in the integral we obtain a fitting function for the density distribution at t_2, where the width of the Gaussian σ is the only free parameter. The result of the deconvolution procedure is the momentum distribution reported in Fig.5.7 **b**.

From the measured value of $\sigma^2 = \langle k \rangle^2$ we can calculate the mean kinetic energy as $E_{kin} = 3(\hbar^2\langle k^2\rangle/2m)$, which for the dataset used here as example is 16.5 nK.

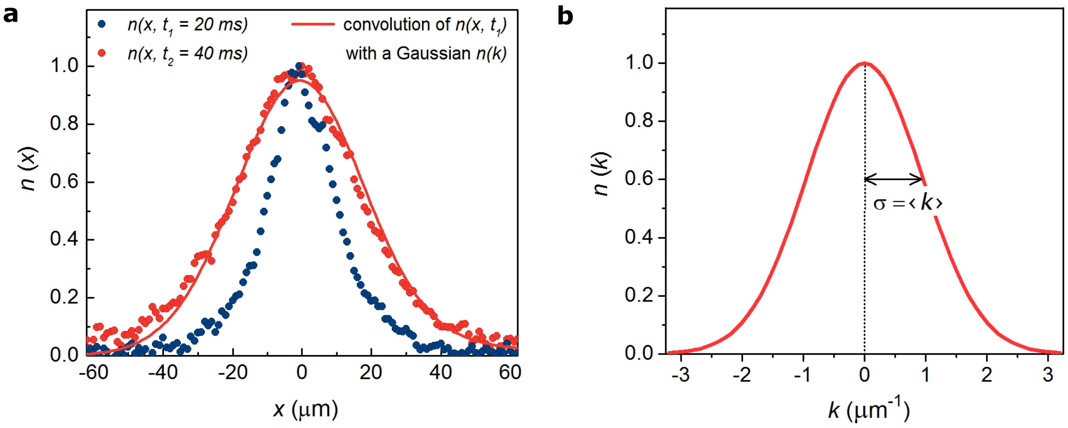

Figure 5.7 | **Measurement of the momentum distribution.** In **a** are reported the time-of-flight density profiles at 20 (blue) and 40 (red) ms of expansion. The red solid line is a fit of the experimental data at t_2 using the convolution of $n(x, t_1)$ with a Gaussian $n(k)$. The momentum distribution obtained from the fit is reported in **b**.

5.3.2 Calculation of the spectral function

It is well known that performing numerical calculations for energies close to the mobilty edge is very hard. The reason for this is the divergence of the localization length when approaching the mobility edge, which comes up against the finite spatial size in the simulations. Nevertheless, we found that performing calculations on a box with side length of about $10\pi\sigma_R$ could give reliable results in the low-energy region of the spectrum, where localization lengths are smaller. This means that we cannot reconstruct the energy distribution for all the samples studied in Sec. 5.2, but we can reliaby deduce it for all the cases where a consistent fraction of the atoms lies well below the mobility edge. We hence take into consideration the range of disorder strengths $V_R/k_B \geq 18$ nK.

We solve the single-particle Schrödinger equation by exact diagonalization of the system. The Hamiltonian is $H = \mathbf{p}^2/(2m) + V_{speckle}(\mathbf{r})$, where $V_{speckle}(\mathbf{r})$ is a 3D potential generated by the interference of two synthetic speckles with transverse correlation length $\pi\sigma_R = 2.4$ μm, corresponding to the average of the experimental ones (see Sec. 4.3.2). We neglect the longitudinal evolution of each speckle field, which is on a much longer length scale. The typical system is a cubic box with side length $L = 12.5$ μm and a discretization length of 0.25 μm. The axes of the cube are along the three principal axes of the crossed speckle field as in Fig. 4.7. All results are averaged over at least 50 different realizations of the disorder.

We evaluate the momentum distribution of each single eigenstate $\psi(E_i, \mathbf{r})$ by Fourier transform. We integrate it along two spatial directions as in the experiment to obtain $|\psi(E_i, k)|^2$. The disorder-averaged collection of all $|\psi(E_i, k)|^2$ is, besides a normalization constant, the spectral function $\rho(E, k)$.

The average density of states $g(E) = \int \rho(E, k)\ dk$ shows a power-law scaling for energies larger than a certain minimum energy E_0: $g(E) \propto |E - E_0|^\alpha$. The typical exponents for $g(E)$

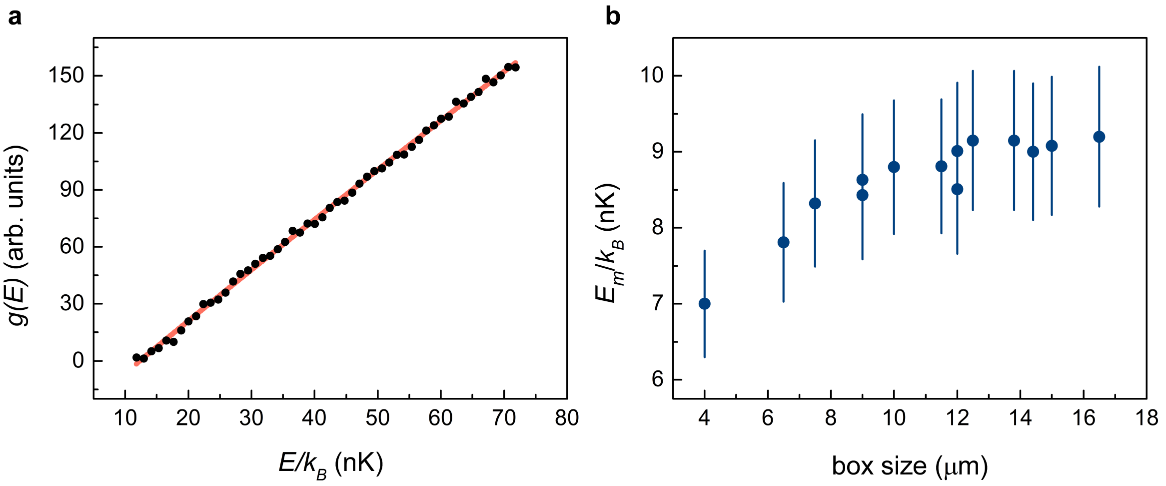

Figure 5.8 | Numerical simulation of low-energy states. In **a** I report the average density of states obtained from the simulated spectral function $\rho(E,k)$ for $V_R/k_B = 47(5)$ nK. The red line corresponds to a power-law fit $g(E) \propto |E - E_0|^\alpha$. An exponent $\alpha = 1$ is obtained for this specific disorder amplitude. The plot in **b** represents a test of the validity of our numerical results. I plot the estimated value of E_m (see Fig. 5.9) obtained from the spectral function calculated with different sizes of the simulated system. The saturation observed above 10 μm confirms that the finite size available in simulations is not affecting our results.

are between 1 and 2, and they grow with V_R. In the example reported in Fig.5.8 **a** for $V_R/k_B = 47$ nK, we find $\alpha \simeq 1$.

5.3.3 Reconstruction of the energy distribution

Now that we dispose of the information about the momentum distribution and the spectral function, we can proceed to reconstruct the average occupation probability of the energy states using the realtion $\int \rho(E,k) f(E)\, d(E) = n(k)$. We thus search for the $f(E)$ that, weighted by the spectral function and integrated over the energies, best reproduces the experimental $n(k)$. We find a very good agreement with data by using an exponential form $f(E) \propto \exp(-E/E_m)$. The parameter E_m, which can be seen as an effective temperature of the system, is found by fitting the integral form for $n(k)$ to the experimental one, as shown in Fig. 5.9 **a**. The energy distribution is then found as $n(E) = \int \rho(E,k) f(E)\, dE = g(E) f(E)$. Fig. 5.9 **b** shows the measured $n(E)$ for a relatively strong disorder, i.e. $V_R/k_B = 47(5)$ nK. According to the scaling of $g(E)$ found in the simulations and already discussed above, we fit the measured energy distributions with $n(E) = g(E)f(E) = (E - E_0)^\alpha \exp(-(E - E_0)/E_m)$. The parameter E_m was deduced in the reconstruction process of Fig. 5.9 **a** and the free parameters are E_0 and α.

Note that the profile of $n(E)$ we obtain is compatible with the observations relative to the expansion in the disorder (Fig. 5.2). For $V_R/k_B = 47(5)$ nK we indeed observed a long-time behavior compatible with a plateau and we find here that the corresponding $n(E)$ is narrow and peaked at an energy E_p not far from the lowest significant energy E_0. Assuming $E_c \approx V_R$, as predicted by theory, this energy distribution is consistent with a large localized fraction, as

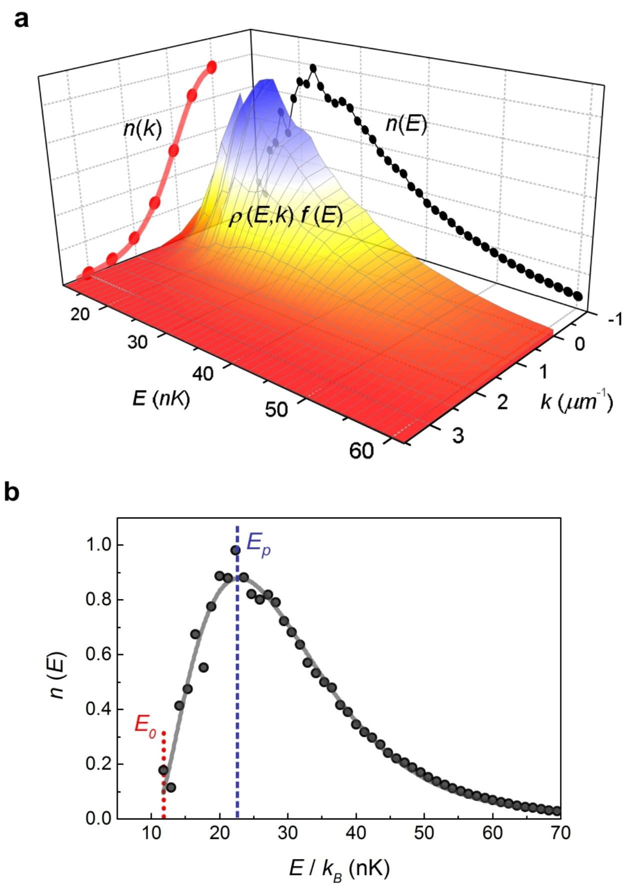

Figure 5.9 | **Reconstruction of the energy distribution.** **a**) Schematic of the reconstruction process of $n(E)$ for $V_R/k_B = 47(5)$ nK: the occupation probability $f(E)$ is found so that the values of $\int \rho(E,k)f(E)dE$ (red dots) from the calculated $\rho(E,k)$ match with the experimental $n(k)$ (red line). The calculations are performed on a discrete grid with spacing of 0.5 μm^{-1} and 2 nK in momentum and energy, respectively. **b**) Expanded view of the reconstructed $n(E)$. The data (dots) are fitted with the model described in the text (line).

suggested by the measurement of $\Delta\langle x^2\rangle(t)$.

5.3.4 *A posteriori* check of the numerical results

In order to estimate finite size effects on our numerical results, we have performed the simulations for various box sizes L and then we have studied how the calculated quantities in momentum space evolve with L. In Fig. 5.8 **b** we report for example the values of E_m obtained from the fit of $n(E)$ as a function of the box size. The disorder strength is $V_R/k_B = 47$ nK and the discretization lengths are in the range (0.2-0.3) μm. For small box sizes E_m shows a clear evolution with the size, while for the larger sizes it tends to saturate. This indicates that boxes of (12-16) μm are large enough to correctly describe the evolution in momentum space of the eigenstates in the energy range of our interest.

We note that if we perform a similar analysis in real space, for example by evaluating the one-dimensional participation ratio $1/\int(\int\psi(x,y,z)^2\,dydz)^2\,dx$, which is a measure of the characteristic length of the eigenfunctions, we find instead that our typical box of 12 μm gives reliable results in real space only up to energies of the order of $V_R/3$.

We thus conclude that, even if our finite-size simulations allow to properly describe only the lowest states in the energy spectrum, their computing capability is sufficient to catch the information relevant to our purpose. Data reported in Fig. 5.8 **b** indeed demonstrate that the typical energy content of our system is well reproduced.

5.4 Spectroscopic technique to measure the mobility edge

Let us briefly summarize the steps made so far. We first implemented a loading procedure able to populate the low-energy states of the disordered Hamiltonian. This allows to reconstruct the energy distribution of the atoms, combining the experimental measurement of the momentum distribution and the numerical calculation of the spectral function, the last giving reliable results only in the low-energy part of the spectrum. In order to measure the position of the mobility edge, there is only one step missing, which is the subject of the present section.

5.4.1 Perturbation scheme

The idea (sketched in Fig. 5.10) is to start from an atomic sample which is mostly localized and with a known energy distribution and to excite a fraction of it with controlled energy. Studying the energy needed to promote the excited fraction to diffusive states, we can determine the position of the mobility edge.

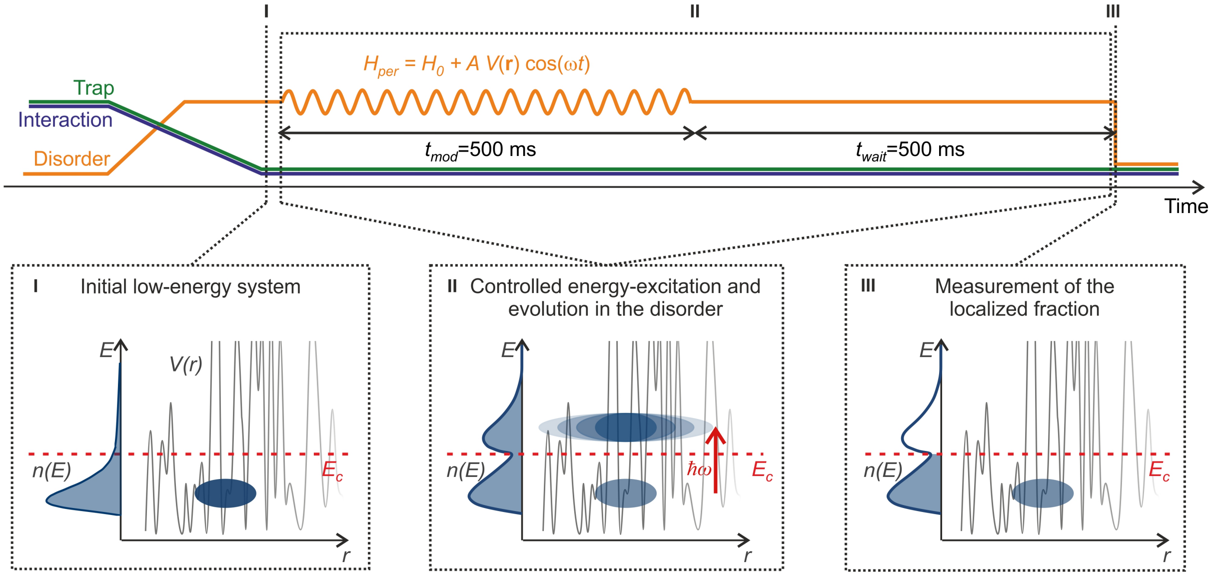

Figure 5.10 | Scheme of the spectroscopic technique.

Controlled energy excitations can be produced by applying a time-dependent perturbation to the external disordered potential. In particular, we load the atoms in the disorder with the desired amplitude V_R, and then we apply a weak sinusoidal modulation $V_R(t) = V_R(1+A\cos(\omega t))$, with $A \simeq 0.2$ and variable modulation frequency ω. In the limit of weak perturbations, we can apply the well-known Fermi golden rule to calculate the excitation probability, which results to be

$$p(E,\omega) = A^2 \sum_{i,f} |\langle f|V(\mathbf{r})|i\rangle|^2 \; \delta(E_i - E) \; \delta(E_f - (E + \hbar\omega)), \tag{5.2}$$

where E is the initial energy of the atoms and i,f are the labels for the initial and final states which span over the whole energy spectrum. The excitation probability p is then in principle depending both on the initial energy E and on the modulation frequency ω via the matrix element $|\langle f|V(\mathbf{r})|i\rangle|$. We estimated through numerical simulations that in the relevant range of energies this dependence is sufficiently weak to allow the assumption that p is constant. I will take over this point later and discuss the legitimacy of this assumption, also estimating its effect on our results. The excited energy distribution is given by

$$n'(E,\hbar\omega) = (1-p)\; n(E) + p\; n(E - \hbar\omega), \tag{5.3}$$

where $n(E)$ is the initial energy distribution.

We apply the sinusoidal modulation to the speckles for 500 ms, then we leave the potential at the fixed value V_R and let the atoms expand into it. After a sufficiently long waiting time, the atoms trasferred to diffusive states have spread enough to be effectively not visible to our imaging system. The transfer to diffusive states is then detected as atom losses. We fix the waiting time at $t_{wait} = 500$ ms, on the basis of the dynamics observed in Fig. 5.2. The diffusion coefficients from 500 ms up to the largest times are well below the diffusion quantum limit $\hbar/3m$. This means that the residual dynamics we observe in this time interval can be associated both to diffusive atoms very close in energy to the mobility edge and to localized atoms with long localization lengths that are still adapting to their equilibrium configuration. Also after the excitation process, we expect that if some diffusive component is still detectable on this timescale, it can only induce a small shift in the estimation of E_c. In order to estimate a possible systematic shift, we will perform the same measurement with a doubled waiting time and compare the results (see Sec. 5.4.3).

5.4.2 Excitation spectra

We measure the final atom number as a function of the modulation frequency ω and we find the results showed in Fig. 5.11 for $V_R/k_B = 47(5)$ nK. These data are used to deduce the position of E_c by fitting them with

$$N_{loc}(\omega) = \int_0^{E_c} n'(E,\hbar\omega)\; dE = \int_0^{E_c} (1-p)\; n(E) + p\; n(E - \hbar\omega), \tag{5.4}$$

where $n(E)$ is the unperturbed energy distribution found in Fig. 5.9, while p and E_c are free parameters. For the dataset reported in Fig. 5.11 the value of E_c obtained from the fit is $E_c/k_B = 50(6)$ nK.

We find a very good agreement between the data and the model until a large-ω regime, where we observe an unexpected increase of N. This behavior can be justified by considering the reduced overlap in momentum space between deeply localized states and the essentially free states high in the continuum, which reduces the excitation probability p. In the absence of a precise model, we exclude the data at high frequency from the fit.

Let us take a closer look at the excitation spectrum in Fig. 5.11. The initial decrease of $N(\omega)$ from 1 to 0.5 corresponds to shifting the excited fraction from the unperturbed one until the minimum energy E_0 is brought to E_c. In a sense E_c could be simply deduced from the onset of the plateau $\hbar\omega_2$ in $N(\omega)$ as $E_c = \hbar\omega_2 - E_0$.

A further check of the consistency of the model used to interpret $N(\omega)$ is found in the behavior of two additional observables: the system size and the kinetic energy, both measured at the end of the excitation process, like $N(\omega)$. The data are reported in Fig. 5.11 **c**,**d**. We observe that they have a maximum value around the same excitation energy $\hbar\omega_1$. This excitation energy perfectly matches with the energy needed to bring the peak of $n(E)$ just below the position of the mobility edge obtained from the fit of $N(\omega)$ in Fig. 5.11. This is indeed the condition to have the largest fraction of atoms close to E_c, thus with the largest localization lengths and the maximum energy. Furthermore, the maximum size reached after the modulation leads to an estimation of an effective diffusion coefficient $D = \Delta\langle x^2\rangle/2\Delta t \simeq \hbar/2m$. This value of D is comparable to the one we measure for systems that have a peak energy E_p close to the mobility edge from the very beginning, as for example the sample at $V_R/k_B = 23(2)$ nK in Fig. 5.3, confirming that at $\hbar\omega_1$ we realize an optimum transfer of atoms at the mobility edge.

5.4.3 Test of the main assumptions in the model

At the end of this section we want to verify the validity of the the main assumptions used in the model of the excitation process, i.e. that we work in the weak perturbation limit and hence in the framework of the Fermi's golden rule, that the excitation probability can be considered constant in the relevant range of energies and finally that the waiting time we used is sufficient to lose diffusive atoms.

Linear response regime

To test the validity of the perturbative approach, we verify that the atom number at the end of the excitation sequence, which is proportional to $1-p(E,\omega)$, scales linearly with A^2, as expected from Eq. 5.2. The measurements shown in Fig. 5.12 are taken for two different values of ω at V_R/k_B= 47(5) nK: the linear scaling we observe confirms that we are in the linear response regime, hence the validity of Eq. 5.2.

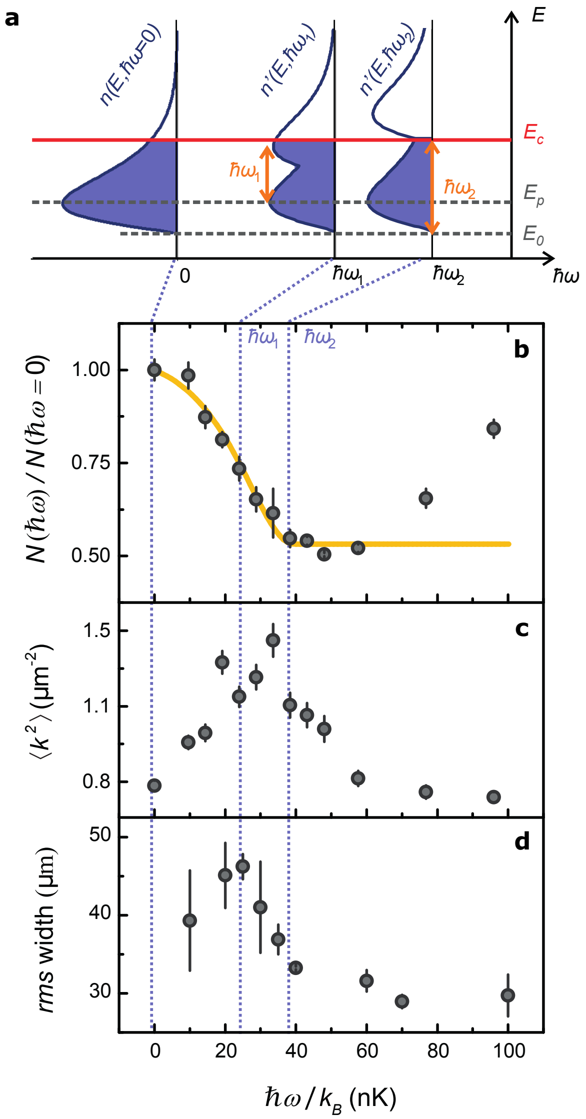

Figure 5.11 | **Excitation spectra.** **a**) During the time modulation of the disordered potential, a fraction of the initial energy distribution gets shifted to higher energies by $\hbar\omega$, where ω is the modulation frequency. For sufficiently high ω, part of $n(E)$ is excited above E_c and then diffuses away during the following waiting time. **b–d**) At the end of t_{wait} we record the atom number (**b**), the kinetic energy (**c**) and the spatial size (**d**) of the cloud as a function of ω. The data reported here are for $V_R/k_B = 47(5)$ nK. The error bars represent statistical uncertainties and correspond to one standard deviation. A fit of the atom number with the excitation model described in the text (yellow line) gives the mobility edge at $E_c/k_B = 50(6)$ nK. Placing this threshold on the energy distributions in **b** one can realize that the positions of the maximum size and kinetic energy (at $\hbar\omega_1$) and of the minimum atom number (at $\hbar\omega_2$) in the spectra are consistent with the features of the corresponding $n(E, \hbar\omega_{1,2})$ as explained in the text.

Constant excitation probability

We use numerical simulations to estimate the dependence of the excitation probability p on the initial energy E. In order to stay in the low-energy regime where simulations are reliable (see Sec. 5.3.4) we consider low modulation frequencies. We find a typical linear scaling $p(E) = p_0 + cE$

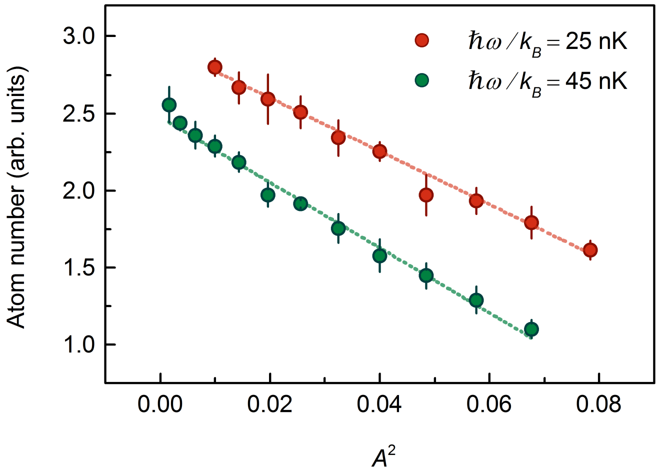

Figure 5.12 | Validity of the perturbative approach. The atom number at the end of the excitation sequence is measured for different values of the modulation amplitude A. The linear scaling with A^2 confirms the linear response regime and then the validity of the perturbative approach we used.

with $p_0 \simeq 0.5$ and $c \simeq 0.2$ nK^{-1}. If we consider this dependence in the calculation of $n'(E, \hbar\omega)$ and hence in the fitting function for $N(\omega)$ (Eq. 5.4), we find a very small shift of E_c with respect to the one obtained in the assumption of constant p. Actually, even a 3 times larger slope c than the one we get in the simulations would not change E_c by more than 2 nK. This very weak dependence of E_c on the actual form of p is probably due to the fact that the shape of the excitation spectrum $N(\omega)$, and hence the result of the fit, are mainly determined by the low-energy part of $n(E)$, namely between E_0 and E_p. This means that the method used to determine E_c is only sensitive to the value of p in a small range of energy, thus insensitive to its changing on a larger scale.

We therefore conclude that the approximation $p(E, \omega) =$ const provides reliable results for the mobility edge and that a possible reduction of the excitation probability at high frequencies does not affect the estimation of E_c.

Finite waiting time

In order to estimate the effect of the finite waiting time after the excitation sequence, we repeat the measurement of the final atom number with a doubled waiting time $t_{wait} = 1$ s. The data for the two different t_{wait} are reported in Fig. 5.13. We observe a small shift in the position of the minimum atom number, then we build a simple model to estimate the asymptotic value of E_c for an infinite waiting time. We start from the hypothesis that we are overestimating the position of the mobility edge because of the presence of slow diffusive atoms still visible in the imaging field of view, as suggested by the shift of the minimum atom number to lower energy for longer t_{wait}. We suppose that the value of $E_c(t_{wait})$ measured after a finite waiting time is shifted with respect to the true value $E_c(t_{wait} \to \infty)$ by an amount that decreases exponentially with time: $E_c(t_{wait}) = E_c(t_{wait} \to \infty) + C\exp(-t_{wait}/\tau)$. We plug this into the expression of Eq. 5.4, which becomes a two-variable function: $N_{loc}(t_{wait}, \hbar\omega) = \int_0^{E_c(t_{wait})} n'(E, \hbar\omega)\, dE$. We use this formula to perform a simultaneous fit of the two datasets, with $E_c(t_{wait} \to \infty)$, τ and C as free parameters. The black and red lines in Fig. 5.13 represent the result of the fit at 500 ms and 1 s respectively. We find $E_c(t_{wait} \to \infty) = 44(3)$ nK, $C = 0.5(1)$ nK and $\tau = 0.3(1)$ s. This implies a shift of the mobility edge with respect to the one measured at $t_{wait} = 500$ ms of 6 nK. Since we cannot support the model for $E_c(t_{wait})$ with a complete set of data as a function of time, we think it is more appropriate to use this result as a systematic error rather than as a proper determination of the asymptotic value. A systematic error of -6 nK is then added to the statistical uncertainties in the results for E_c (see Fig. 5.14).

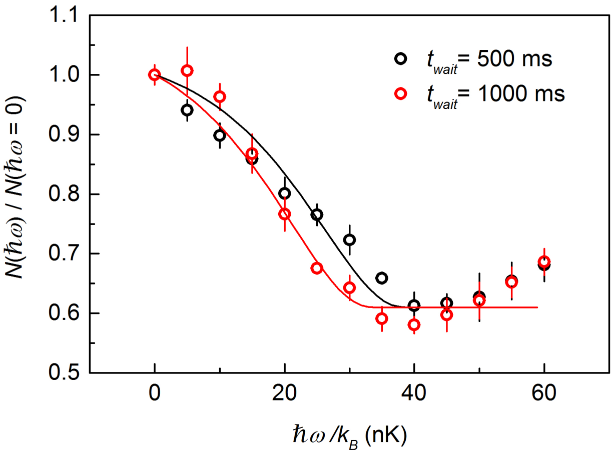

Figure 5.13 | Effect of the finite waiting time. The same excitation spectra of Fig. 5.11 is measured for two different waiting times. The two are fitted with the model explained in the text to estimate a possible shift of the asymptotic mobility edge at infinite waiting time. Solid lines represent the fitted curves.

5.5 Mobility edge vs Disorder strength

Repeating the excitation procedure for several disorder strengths, we obtain the trajectory of the mobility edge in the disorder-energy plane reported in Fig. 5.14. The range of disorder strengths we could investigate allowed us to explore two different regimes and the crossover between them. The most interesting regime for Anderson localization has always been considered that with $V_R < E_R$, since in this case there is a very small probability that the atoms are trapped in the single deep wells of the disordered potential, so that any localization effect can definitely be attributed to quantum interference between multiple scattered waves, i.e. to pure Anderson localization (see the discussion about this in Sec. 4.2). In this regime the spatial correlations of the disorder should not have a dominant role, because E_c is smaller than the correlation energy E_R. When $V_R \gtrsim E_R$ the spatial correlations of the potential start to play a role and the localization mechanism gets more intricate and related to the specific statistics of the random potential we are using.

We observe that in the range of small V_R, i.e. up to V_R/k_B= 47(5) nK our data are consistent with a linear scaling of E_c with V_R. When V_R is increased above E_R there is a clear reduction of the slope of E_c.

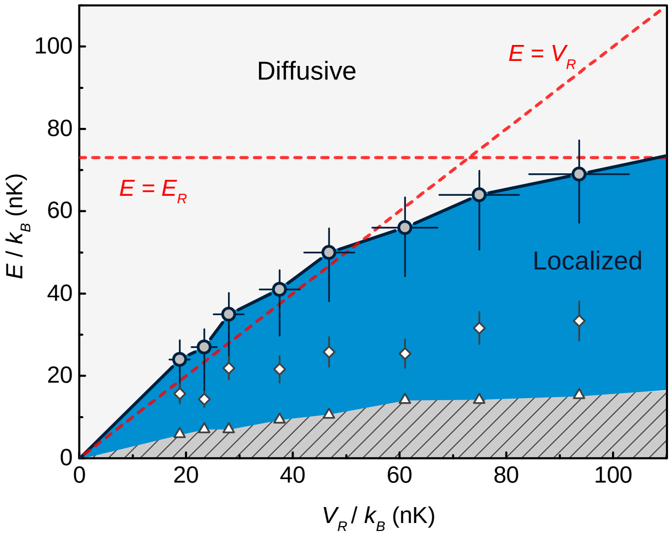

Figure 5.14 | Measured mobility edge versus disorder strength. Trajectroy of E_c (circles) separating localized from diffusive states. White diamonds are the peak energies E_p of $n(E)$ and white triangles are the lowest energies E_0. The error bars for E_p represent the statistical uncertainty in the determination of $n(E)$. The vertical error bars for E_c contain the statistical uncertainties in the determination of $n(E)$ and in the fit of $N(\omega)$, and also the systematic uncertainty from the finite waiting time; the horizontal ones represent the 10% uncertainty in the determination of V_R (Sec. 4.4). All error bars correspond to one standard deviation.

5.5.1 Comparison with analytical and numerical results

Being our results the first experimental measurement of the mobility edge with ultracold atoms, it worth carry out a detailed comparison with the available theoretical results. There are mainly two class of theoretical works we can compare to: analytical results from self-consistent theories and numerical simulations. I briefly describe the methods they use and their main outcomes and then I compare them with our results.

Self-consistent theories

A first naive application of the self-consistent theory (Sec. 2.2.3) to ultracold atoms in speckle potentials was developed in [53]. This early version was based on quite strong assumptions that turned out to be significantly misleading: the scattering amplitude is evaluated at the lowest order in the Born approximation and the spectral function and density of states are assumed to be unaffected by the disorder (so-called "on-shell" approximation). The mobility edge was predicted to be larger than the disorder strength and scaling as V_R^2.

A first strategy to refine this initial formulation has been performed in [54] and [55]. In particular, they go beyond the "on-shell" approximation by taking into account the real part of the self-energy in the calculation of the spectral function. This has a dramatic effect on the location of the mobility edge, which is now predicted to be below V_R, with a dependence on it which varies for large V_R, as the correlation energy starts to play a role. Anyway, these approaches are still limited to the lowest approximation order, so that their validity is confined to a narrow range of small disorder strengths.

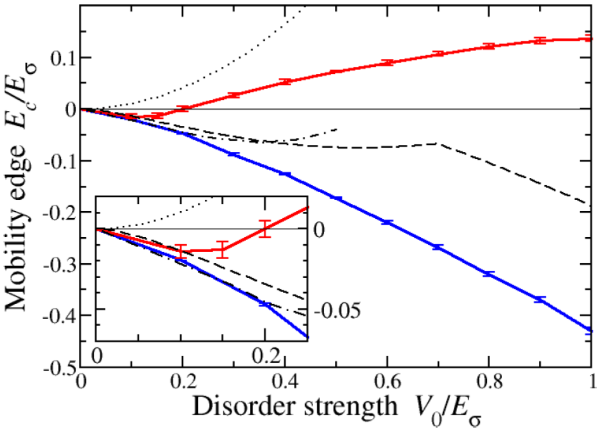

Figure 5.15 | Mobility edge from numerical calculations. Numerical calculations of the mobility edge for cold atoms in 3D speckle potential. The thresholds for both blue-detuned (blue) and red-detuned (red) configurations are measured. The results are compared with the predictions of the available self-consistent theories: [53] (dotted line), [55] (dashed line) and [54] (dash-dotted line). Figure from [56].

Numerical results

In a recent theoretical work [56] D. Delande and G. Orso applied the transfer matrix method, already used to simulate the Anderson model, to the problem of atoms in optical speckles. They consider isotropic speckles and predict the behavior of the mobility edge on a range of disorder strengths from zero to E_R. They find that for blue-detuned speckles the mobility edge is well below V_R and deviates significantly from the predictions of the most recent self-consistent theories [54, 55]. In particular they find that these approximate theories are able to reproduce the numerical results for very low V_R, namely $V_R < 0.2E_R$, but overestimate the threshold for larger V_R. They study also the case of red-detuned speckles and find a very different result: E_c is initially very close to V_R and below it, but for increasing disorder strengths it becomes larger than V_R and keeps on increasing. These results are reported in Fig. 5.15 in comparison with the estimates from SC theory.

In [57] E. Fratini and S. Pilati apply a different computational method, drawn from quantum-chaos theory, to estimate the position of the mobility edge, taking into account the effects of anisotropy in the disorder correlation function. Their method is able to reproduce the same results of [56] for the case of isotropic speckles, but it is also applied to realistic experimental conditions, which typically display anisotropic correlation lengths. They find that in the case of "elongated" speckles, e.g. for a single speckle beam, the mobility edge is slightly reduced with respect to the isotropic case. In the opposite case, when the speckles are "squeezed", e.g. with two interfering speckles, the mobility edge significantly increases with respect to the isotropic value, always staying below V_R. These two opposite behaviors are reported in Fig. 5.16 for a specific value of the disorder strength, $V_R = E_\sigma$, where E_σ is the correlation energy relative to the transverse correlation length.

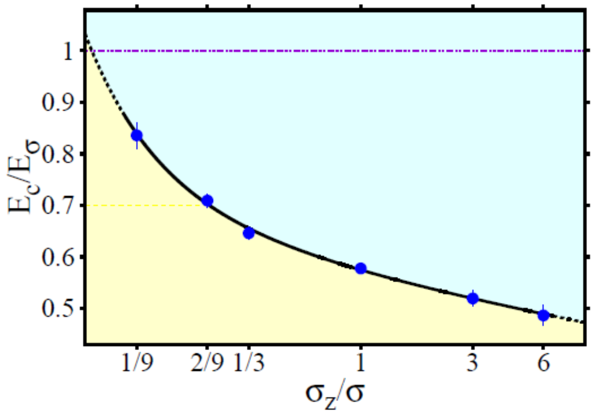

Figure 5.16 | **Mobility edge as a function of the anisotropy parameter**. Figure from [57]. σ_z and σ are the axial and the radial correlation lengths, respectively. $\sigma_z/\sigma > 1$ represents the case of elongated speckles, while $\sigma_z/\sigma < 1$ is the "squeezed" case, which also approximately describes the situation of interfering speckles as in our experiment.

Let us compare the results in Fig. 5.14 with these numerical estimates. Our results are typically $\sim 40\%$ larger than the values predicted for isotropic speckles in [56]. Anyway, the results of [57] clearly show the influence of anisotropy on the position of E_c and also predict a shift of the mobility edge in the same direction of our data. Considering the specific correlation lengths in our experiment, the predicted shift with respect to the isotropic case should be the same as for the point at $\sigma_z/\sigma = 2/9$ in Fig. 5.16. The mobility edge should then be found at $E_c \approx 0.7E_\sigma$. This is still $\sim 30\%$ smaller than our results in the same range of disorder strengths. This discrepancy certainly requires further investigations. As the authors state in the conclusions of [57], the computational technique they developed should be applied to the specific parameters of our disordered potential to allow a detailed comparison. As they show in the plot of Fig. 5.16, there is a quite steep increase of the mobility edge on the left side of the isotropic case, so that the correct anisotropy should be taken into account to provide a significant prediction for our experimental setup.

Note that the results of [57] are in sharp contrast with the experimental estimations provided in [35], since in the "elongated" speckle case they predict a mobility edge even smaller than the one for isotropic correlations, while the measured value is approximately three times larger. This proves that the assumptions used for that experimental measurement, in particular those concerning the energy distributions, are not reliable and provide a mobility edge much larger than the expected one. This fact highlights the importance of the novel technique we designed to determine the energy distributions from experimental measurements and well controlled numerical estimations, since not careful assumptions about the energy have proved to be highly misleading.

Now that reliable numerical estimations are available, a close experiment-theory interaction could allow a final assessment of the problem of the mobility edge for correlated disordered potentials.

5.6 Outlook: effects of weak interactions

Most of the work of my PhD has been devoted to the study of non-interacting particles. In what I presented so far, I showed that even the single-particle localization problem, which is conceptually very simple, is hard to study in a quantitative way. The experimental techniques developed in the past few years finally allowed us to measure the mobility edge, a property of disordered systems first predicted by Anderson more than fifty years ago. The most natural outlook is now the study of how finite interactions affect the behavior of disordered systems. The problem becomes certainly much harder and the open questions concern even the basic understanding of the phase diagram arising from the interplay of disorder and nonlinearities.

Inter-particle interactions certainly break the orthogonality of the single-particle states and tend to couple them, but it is not clear at all if this process should result in a complete breakdown of Anderson localization or not. There are examples in nature and theoretical models of disordered systems where the interaction between particles destroys the localization effect and gives rise to metallic phases, glassy phases or even to superconducting phases [58, 59, 60, 61, 62, 63, 64, 65]. However, the existence of an insulating regime in presence of interactions is not excluded and there are theories predicting the so-called *many-body localization* (MBL) phenomenon [66].

The problem is very difficult and the experimental studies are still scarse. In this context, ultracold atoms could once again provide an optimum investigation tool. So far the interplay of disorder and interactions has been studied with atoms only in 1D [67, 58, 68, 69, 70, 71, 72, 73] and 2D [74, 75]. Our experimental setup offers the opportunity of investigating the 3D problem for the first time, in a system with a well characterized single-particle mobility edge. Using the same approach as in the experiments of this chapter, we can study out of equilibrium properties, i.e. the expansion dynamics of an interacting sample in disorder, which allows to detect whether the system is localized or not.

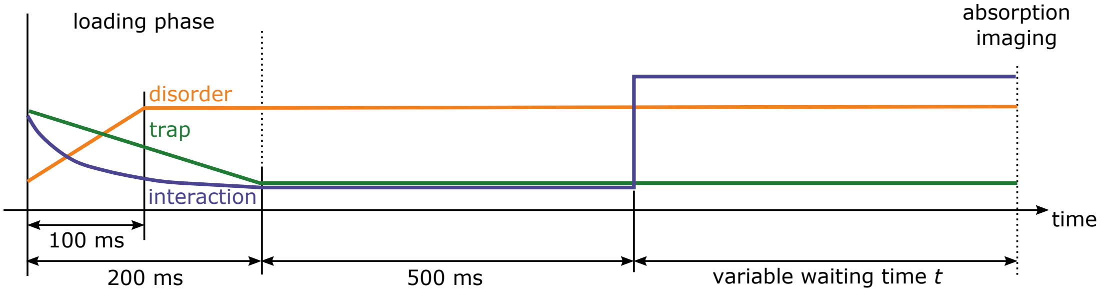

Figure 5.17 | Experimental sequence to probe the effects of weak interactions. We perform the same quasi-adiabatic loading procedure used in Sec. 5.1 to prepare low-energy localized states. After that, we let the system evolve for 500 ms so that the atoms reach their equilibrium localized configuration. At the end of this localization time, we abruptly change the value of the scattering length from zero to a finite value a. After a variable waiting time we image the atoms to investigate their transport properties.

The simplest experiment we can think of consists in preparing a non-interacting localized sample, whose properties are now well characterized, and suddenly change the interaction strength to some finite repulsive value. In order to do this, we follow the same loading procedure described in Fig. 5.1 and then we instantaneously change the scattering length to a desired value a. We let the system evolve in the disordered potential and we finally image the atomic cloud after a variable expansion time (the sequence is depicted in Fig. 5.17).

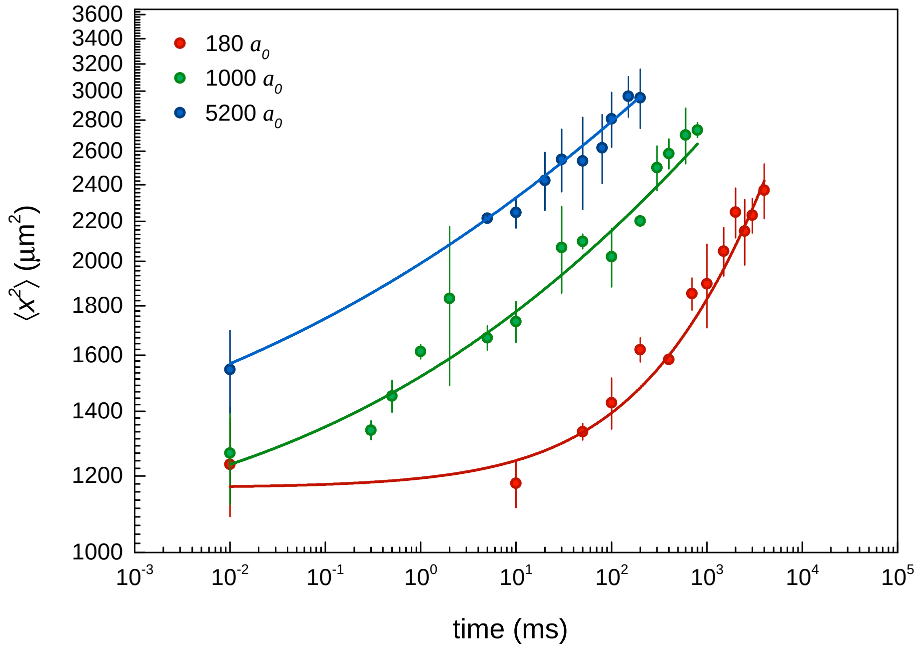

Figure 5.18 | Expansion in presence of weak repulsive interactions. We measure the second moment of the atomic distribution $\langle x^2\rangle(t)$ as a function of the expansion time t for $V_R/k_B = 74$ nK and different values of the scattering length a: 180 a_0 (red), 1000 a_0 (green), 5200 a_0 (blue). The data are fitted with $\langle x^2\rangle(t) = \langle x^2\rangle(t=0) + Dt^{\alpha}$ (solid lines).

Exactly as in the non-interacting case, we measure the second moment of the one-dimensional density distribution $\langle x^2\rangle(t) = \int x^2\ n(x,t)\ dx$ to probe the time evolution of the cloud. In Fig. 5.18 I report the data corresponding to a large disorder amplitude $V_R/k_B = 74$ nK and to three different interaction strengths. We clearly see that the system starts expanding, indicating that the interaction term triggers transport through the sample. The first qualitative conclusion is that Anderson localization is broken and the system enters a conducting regime. By giving a closer look to the kind of evolution we observe, we notice that it is not diffusive, since the squared width does not grow linearly with time. We find instead a subdiffusive behavior [76, 77], where the cloud evolves according to $\langle x^2\rangle(t) \propto t^{\alpha}$, with α smaller than one. A similar behavior has already been observed for atoms in 1D [69].

It is interesting to try and reconstruct an intuitive explanation of the expansion we observe. From a theoretical point of view, a proper description of the interacting system requires introducing a many-body Hamiltonian. In the limit of weak interactions, one can attempt a perturbative approach. If the interaction energy $E_{int} = gn$, where g is the coupling constant

$g = 4\pi\hbar^2 a/m$ and n is the atomic density, can be considered a perturbation with respect to the disorder energy scale, the single-particle eigenstates are only weakly modified by interactions. If $E_{int} > \delta E$, where δE is the typical energy distance between single-particle states in a unit volume, the interaction term couples neighbouring states, i.e. those within a localization length. The expansion can therefore be interpreted as the progressive coupling of the initially occupied states to empty states in the periphery of the sample. As the atoms move away from the intial position, the density decreases and therefore also the interaction energy decreases, thus reducing the coupling rate. At an intuitive level, this justifies the subdiffusive behavior, since the instantaneous diffusion coefficient decreases with time. This explanation perfectly fits with our experimental conditions, since the typical interaction energies we introduce are sufficient to achieve a good coupling between localized states. The energy separation between the single-particle eigenstates in the speckle potential is indeed of the order of $\delta E/k_B \sim 1$ nK. Taking into account the typical densities in our non-interacting localized samples and the scattering lengths of Fig. 5.18, we find that the initial interaction energy ranges from 1 to 10 nK$\times k_B$. This means that the interaction energy is sufficient to couple a significant number of localized single-particle states, so as to trigger the expansion dynamics.

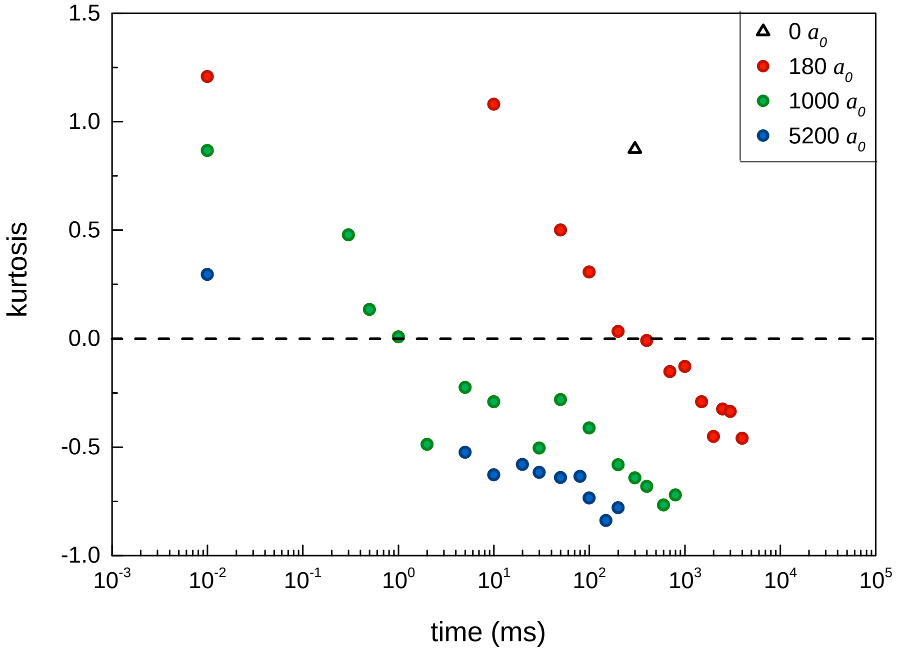

Figure 5.19 | **Evolution of the kurtosis.** The kurtosis $k = \langle x^4\rangle/\langle x^2\rangle^2 - 3$ is plotted versus time for $V_R/k_B = 74$ nK and different scattering lengths: 180 a_0 (red), 1000 a_0 (green), 5200 a_0 (blue). A data relative to the non interacting case (triangle) is reported for comparison. The horizontal dashed line corresponds to the Gaussian profile, separating the peaked distributions (above it) from the flat-top ones (below). At long time all the interacting datasets end up in the flat-top region.

A further confirmation of the consistency of our observation with a subdiffusive model is provided by the time evolution of the shape of the cloud. It was indeed observed in the experiment on 1D systems [70] that the subdiffusive expansion was related to a change in the profile of the atomic distribution, which turned from Gaussian to flat-top profiles at long time. The coupling between single-particle states is indeed stronger at the center of the cloud where the density, and thus the interaction energy, are higher. This implies that the atoms at the center move faster than those on the tails of the distribution, leading to a progressive change in the overall shape. This effect is even more prominent in our case, since the atomic distribution is distinctly peaked in the initial localized configuration and then develops a flat-top profile. A quantitative estimation of this change is provided by the measurement of the kurtosis, which is derived from the fourth moment of the density distribution as $k = \langle x^4 \rangle / \langle x^2 \rangle^2 - 3$. The kurtosis is defined in such a way that $k = 0$ in a Gaussian distribution, while $k > 0$ indicates a peaked profile and $k < 0$ a flat-top. In Fig. 5.19 I report the evolution of the kurtosis during the expansion of the cloud for the same values of V_R and a of Fig. 5.18. It is clear that for all the cases reported there the atomic profile goes to negative values of the kurtosis at a certain time, while the data relative to the non-interacting case is close to $k \sim 1$ even at long time.

So far we have presented data relative to the expansion in presence of repulsive interactions. What happens if the interaction is tuned to some finite but attractive value? We repeated the same measurement as before for a small negative scattering length $a = -14\ a_0$. In Fig. 5.20 I report the behavior of both the second moment of the distribution $\langle x^2 \rangle(t)$ and of the kurtosis. The system behaves very similarly to the repulsive case, showing the symmetry of the phenomenon we are observing. This is indeed what one would expect by considering the initial "thermal" distribution of atoms in the non-interacting spectrum.

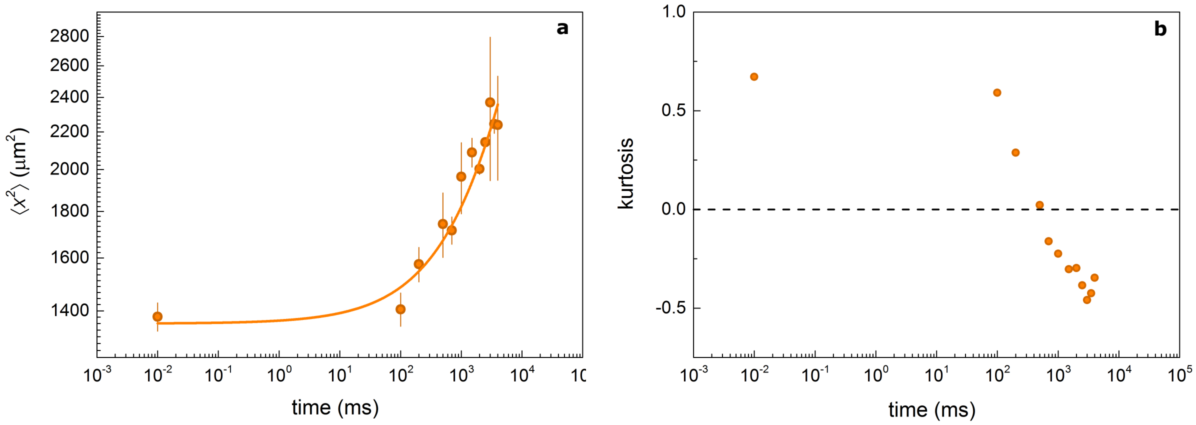

Figure 5.20 | Expansion in presence of weak attractive interactions. We measure the second moment (**a**) and the kurtosis (**b**) of the atomic distribution as a function of the expansion time t for $V_R/k_B = 74$ nK and $a = -14\ a_0$. The solid line in **a** is the fit with the subdiffusive model reported in the text.

The observations reported so far have proved that the localized regime detected in the non-interacting case is broken when adding finite repulsive or attractive interactions that couple a large number of single-particle states. In particular, the dynamics observed is compatible with subdiffusion, which is the expected behavior for a disordered interacting system out of equilibrium. Although the qualitative behavior is well understood by the simple intuitive picture I presented above, a quantitative description of subdiffusive dynamics is not an easy task. There are theories [78, 79] predicting the value of subdiffusion exponents in different dimensionalities, which are based on the estimation of the statistical distribution of states coupled by interaction. For the 3D case, they predict an exponent $\alpha = 1/7$. Nonetheless, these theories only partially account for the specific nature of disordered interacting systems. They do not consider, for example, the presence of the single-particle mobility edge, thus supposing that the atoms only move through the sample by transfer between localized states. It is instead possible that the initially localized atoms couple to extended states above the threshold, which would certainly increase the expansion velocity. Furthermore, the interaction term is treated in a mean field approximation, that do not account for many-body localization effects. In the weak coupling regime, i.e. when the interaction energy is smaller than the energy spacing between the single-particle states, one can expect that the system remains in a localized regime, different from the Anderson one, which would be classified as MBL. Such an effect would probably reduce the asymptotic subdiffusion exponents, which could be a smoking gun for the occurrence of MBL. This basic considerations prove that even an apparently simple phenomenon as subdiffusion needs a careful consideration to be properly described!

We perform a preliminary comparison of our data with the theoretical expectations of [78, 79]. We fit the data in Fig. 5.18 and 5.20a with the subdiffusive model $\langle x^2\rangle(t) = \langle x^2\rangle(0) + Dt^{\alpha}$ and we find the exponents α reported in Fig. 5.21. The results we get are somewhat surprising, since we observe that α decreases with the interaction energy. This is a counterintuitive behavior, since one would expect that the dynamics gets faster as the interaction energy is increased. This is also in contrast with the results obtained in 1D [69], where the exponent was slightly increasing with E_{int}. Our results are close to the value predicted in [78] (dashed line) only for the largest scattering lengths. Anyway, in order to perform a serious comparison with any theoretical prediction, a more careful consideration of some experimental issues is required. One should for example consider if the expansion times probed so far are sufficient to determine the asymptotic behavior of the system, which is essential to properly measure the subdiffusion exponent. In addition to this, we will need to consider the effect of atom losses. When strong interactions come into play, one has to pay attention to three-body losses, which would contribute to an additional decrease of the atomic density with time. Another major issue that manifests as atom losses is instead related to a detection problem. When the cloud expands beyond a certain size, the atomic density is so low that our imaging system cannot distinguish the signal from noise. This is clear if one plots the recorded atom number versus the squared width of the cloud (Fig. 5.22). There we see that the atom number depends on the size of the system, which means that for the largest clouds we are probably losing signal on the tails of the distribution, thus effectively underestimating the width. These considerations let us conclude that the measurements performed so far provide a first clear evidence of the delocalizing effect of finite interactions on a single-particle localized system, but a quantitative description of the dynamics we observe will require further detailed analysis.

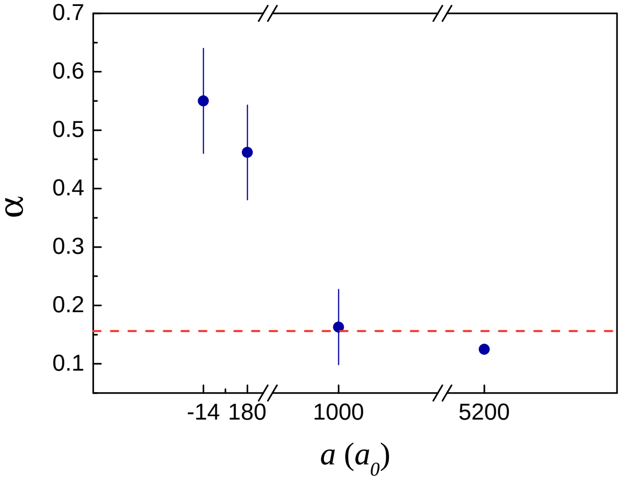

Figure 5.21 | Expansion parameters vs scattering length. Fitted parameter α for the expansion reported in Fig. 5.18 and 5.20**a**, for $V_R/k_B = 74$ nK and different values of the scattering length a. The dashed red line corresponds to the theoretical value predicted in [78].

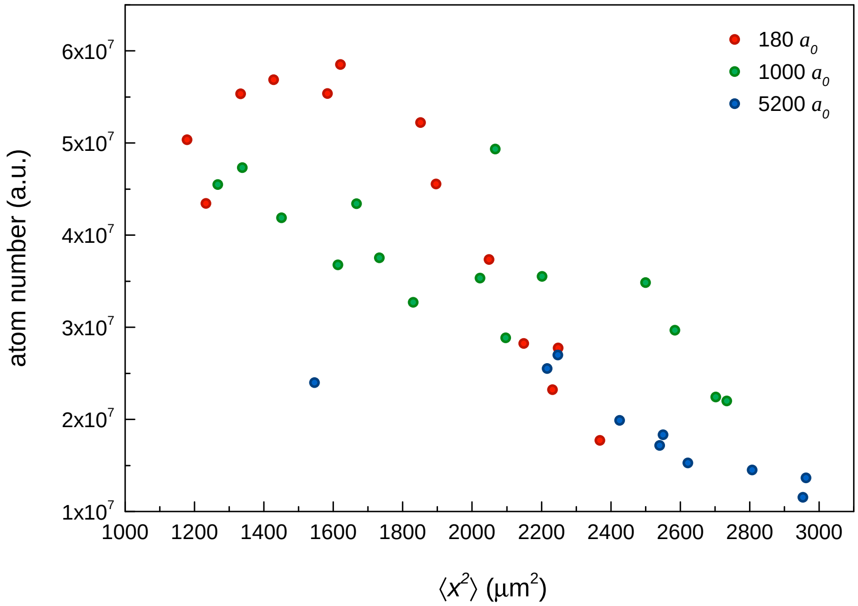

Figure 5.22 | Detection issues for large clouds. We report the measured atom number against the second moment of the distribution. We clearly see that the signal decreases for increasing widths, which means that we are probably losing signal on tails of the distribution. The effect does not seem to depend strongly on the interaction strength.

The preliminary study reported here has certainly remarked the difficulty in exploring the complex phenomena arising from the interplay of disorder and interactions, but it also showed that the experimental setup we used is a promising tool for further investigations, due to the possibility of tuning both parameters and probe different regimes.

Chapter

6

Conclusions and outlook

In this thesis I first provided a background on the studies about Anderson localization, describing the emergence of the phenomenon in the context of condensed matter physics and introducing its relevance in understanding the conduction properties of certain materials. In particular I tried to highlight how the quantum phase transition related to AL is an aspect of primary importance. The identification of the critical parameters for the occurrence of localization could indeed clarify some aspects of metal-insulator transitions occurring in solids, a problem which is as old as still eluding a complete understanding. Furthermore, the study of the Anderson transition is of fundamental interest: it is sufficient to leaf through the book "50 years of Anderson localization" [2] to recognize that there are a number of peculiar features concerning with AL that justify the huge interest arisen around it in the past few decades.

I have then retraced the milestones of the study of the Anderson transition. On one side I recalled the main results concerning with a theoretical comprehension of it: from the general picture provided by scaling theory, to the microscopic analysis of self-consistent approaches and the crucial contribution of numerical simulations. On the other hand I presented the efforts performed to detect and characterize it in experiments: from the evidence of localization in electronic systems, masked by interaction effects, to the observation of the pure Anderson transition in classical waves and atomic kicked rotors. This path allowed to gain a broad view on the present understanding of the phenomenon and on the fundamental open questions.

I have then presented the experimental setup we used to try and answer some of these basic questions. The ultracold gas of ^{39}K atoms provides an ideal tool for the investigation of disorder-related phenomena, due to the tunability of atomic interactions, which allows to switch from the perfect non-interacting to the weakly-interacting regime. The random potential needed to observe AL was then provided by using laser speckles, which have already proved to be a versatile tool to this purpose.

In this experimental context, we designed a novel experimental technique to study the occurrence of the Anderson transition in a system where the energy distributions are well controlled and measured. The loading procedure into disorder, together with the spectroscopic strategy to probe the mobility edge, have thus allowed us to measure the localization threshold in a broad range of disorder strengths, within a model based on well controlled assumptions.

Recent numerical estimations, obtained in the same period of our experiment, have now provided the first reliable predictions about the position of the mobility edge in a correlated disordered potential. There is still not a perfect agreement with our results, since the expected threshold is typically smaller than the one we measured. Anyway, a strict comparison with theories is still not possible, since the detailed features of our experimental potential have never been simulated so far. In fact, a recent work proved the crucial influence of anisotropy in the spatial correlations of disorder on the position of the mobility edge, which has then to be treated carefully. The latest improvements in numerical computations, together with the energy-control technique we designed, are then promising for an early conclusive assessment of the mobility edge in this kind of systems, i.e. non-interacting matter waves in correlated 3D disorder.

A further characterization of the transition would then imply a measurement of the critical exponents. This could be realized by trying to get narrower energy distributions so as to improve the energy resolution when probing the critical point. Another relavant issue to be explored would be the emergence of the Anderson transition when increasing the dimensionality from the critical value $d = 2$, where no transition occurs, to $d = 3$. This could be implemented by using a one-dimensional lattice, to confine the atoms in 2D disks, and then varying the tunneling between neighbouring disks to achieve an effective $d = 2 + \varepsilon$ dimensionality.

The most interesting outlook of the experiment presented here is the study of the effects of interactions on the localization problem. The investigation of the interplay between disorder and interactions would indeed close the gap with the original problem of metal-insulator transitions for electrons and it is relevant to a number of different physical systems, ranging from superconductors, graphene and light in nonlinear media to biological molecules as DNA. A first step in this sense has been done in the very end of Chapter 5, where we studied what happens to a non-interacting localized sample when weak interactions are suddenly turned on. The first preliminary observations showed that weak interactions break AL triggering transport in a subdiffusive regime. A more complete experimental characterization and a detailed study of the existing theoretical predictions will allow to investigate for the first time the phenomenon of subdiffusion in three-dimensional systems.

The number of phenomena arising from the interplay of disorder and interactions is actually large and it spans from many-body localization [66] to Bose-Einstein condensation in presence of disorder [80, 81, 82]. Theoretical approaches to these kind of problems are really hard, due to the high degree of complexity, which is beyond reach both for analytical and numerical methods. In the past two decades ultracold gases have been successfully employed as quantum simulators of complex systems and in the same case of the experiment reported in this thesis they have proved their value in this sense. For this reason, the experiments on ultracold gases are certainly the most promising system to tackle the long-standing questions concerning with disorder and interaction. They offer for example the opportunity of studying both short and long-range interactions, the first being achievable in an experimental system like ours, the second by making use of newly explored systems like dipolar atoms/molecules or Rydberg atoms. One would indeed expect that the two kinds of correlations lead to different kind of regimes, which would be interesting to investigate.

Bibliography

[1] P. W. Anderson, "Absence of Diffusion in Certain Random Lattices", *Phys. Rev.* **109**, 1492 (1958).

[2] *50 Years of Anderson Localization*, E. Abrahams ed. (World Scientific, 2012).

[3] N. F. Mott, "Metal-insulator transitions", *Phys. Today* **31**, 42 (1978).

[4] P. A. Lee, T. V. Ramakrishnan, "Disordered electronic systems", *Rev. Mod. Phys.* **57**, 287 (1985).

[5] S. Roy, M. Landini, A. Trenkwalder, G. Semeghini, G. Spagnolli, A. Simoni, M. Fattori, M. Inguscio and G. Modugno, "Test of the Universality of the Three-Body Efimov Parameter at Narrow Feshbach Resonances", *Phys. Rev. Lett.* **111**, 053202 (2013).

[6] A. Trenkwalder, G. Spagnolli, G. Semeghini, S. Coop, M. Landini, P. Castilho, L. Pezzè, G. Modugno, M. Inguscio, A. Smerzi and M. Fattori, "Observation of Quantum Phase Transitions with Parity-Symmetry Breaking and Hysteresis" (submitted).

[7] G. Feher and E. A. Gere, "Electron Spin Resonance Experiments on Donors in Silicon. II. Electron Spin Relaxation Effects", *Phys. Rev.* **114**, 1245 (1959).

[8] D. J. Thouless, "Electron in disordered systems and the theory of localization", *Phys. Rep.* **13**, 93 (1974).

[9] E. Abrahams, P. W. Anderson, D. C. Licciardello, T. V. Ramakrishnan, "Scaling theory of Localization: Absence of Quantum Diffusion in Two Dimensions", *Phys. Rev. Lett.* **42**, 10 (1979).

[10] B. Kramer, A. MacKinnon, "Localization: theory and experiment", *Rep. Prog. Phys.* **56**, 1469-1564 (1993).

[11] Jørgen Rammer, "Quantum Transport Theory", Perseus Books, Reading, Mass., (1998).

[12] F. J. Wegner, "Exact density of states for lowest Landau level in white noise potential superfield representation for interacting systems", *Z. Phys. B* **51**, 279 (1983).

[13] E. P. Wigner, "On a class of analytic functions from the quantum theory of collisions", *Ann. Math.*, **53**, 36 (1951).

[14] K. B. Efetov, “Supersymmetry and theory of disordered metals”, *Adv. Phys.*, **32**, 53–127 (1983).

[15] F. Evers, A. D. Mirlin, “Anderson transitions”, *Rev. Mod. Phys.* **80**, 1355-1417 (2008).

[16] A. MacKinnon and B. Kramer, “One-Parameter Scaling of Localization Length and Conductance in Disordered Systems”, *Phys. Rev. Lett.* **47**, 1546 (1981).

[17] K. Slevin and T. Ohtsuki, “Corrections to Scaling at the Anderson Transition”, *Phys. Rev. Lett.* **82**, 382 (1999).

[18] B. Bulka, M. Schreiber and B. Kramer, “Localization, Quantum Interference, and the Metal-Insulator Transition”,*Z. Phys. B 66*, 21 (1987).

[19] S. Katsumoto, F. Komori, N. Sano and S. Kobayashi, “Fine tuning of metal-insulator transition in $\mathrm{Al}_{0.3}\mathrm{Ga}_{0.7}\mathrm{As}$ using persistent photoconductivity”, *J. Phys. Soc. Jap.* 56, 2259 (1987).

[20] D. Belitz and T. Kirkpatrick, “The Anderson-Mott transition”, *Rev. Mod. Phys.* **66**, 261 (1994).

[21] D. Vollhardt, P. Wölfle, in *Electronic Phase Transitions* (eds. Hanke, W. & Kopaev, Yu. V.) 1978 (Elsevier, Amsterdam, 1992).

[22] C. A. Müller and D. Delande, “Disorder and interference: localization phenomena” in *Ultracold Gases and Quantum Information: Lecture Notes of the Les Houches Summer School*, edited by C. Miniatura et al. (Oxford University Press, 2011).

[23] A. M. Garcìa-Garcìa, “A semiclassical theory of the Anderson transition”, *Phys. Rev. Lett.* **100**, 076404 (2008).

[24] A. Lagendijk, B. van Tiggelen and D. S. Wiersma, “Fifty years of Anderson localization”, *Physics Today* **62**(8), 24 (2009).

[25] M. Segev, Y. Silberberg and D. N. Christodoulides, “Anderson localization of light”, *Nat. Photonics* **7**, 197 (2013).

[26] H. Hu et al. “Localization of ultrasound in a three-dimensional elastic network”, *Nat. Phys.* **4**, 845-848 (2008).

[27] T. Sperling et al. “Direct determination of the transition to localization of light in three dimensions”, *Nat. Photonics* **7**, 48-52 (2013).

[28] F. Scheffold and D. Wiersma, “Inelastic scattering puts in question recent claims of Anderson localization of light”, *Nat. Photonics* **7**, 934 (2013).

[29] G. Maret, T. Sperling, W. Bührer, A. Lubatsch, R. Frank and C. M. Aegerter, "Inelastic scattering puts in question recent claims of Anderson localization of light", *Nat. Photonics* **7**, 934-935 (2013).

[30] G. Lemarié, H. Lignier, D. Delande, P. Szriftgiser and J.C. Garreau, "Critical state of the Anderson transition: between a metal and an insulator", *Phys. Rev. Lett.* **105**, 090601 (2010).

[31] M. Lopez, J.-F. Clément, P. Szriftgiser, J.C. Garreau and D. Delande, "Experimental test of universality of the Anderson transition", *Phys. Rev. Lett.* **108**, 095701 (2012).

[32] J. Chabé et al. "Experimental observation of the Anderson metal-insulator transition with atomic matter waves", *Phys. Rev. Lett.* **101**, 255702 (2008).

[33] J. Billy et al., "Direct observation of Anderson localization of matter-waves in a controlled disorder", *Nature* **453**, 891 (2008).

[34] G. Roati et al., "Anderson localization of a non-interacting Bose-Einstein condensate", *Nature* **453**, 895 (2008).

[35] S. S. Kondov, W. R. McGehee, J. J. Zirbel, B. DeMarco, "Three-dimensional Anderson localization of ultracold matter", *Science* **334**, 66 (2011).

[36] F. Jendrzejewski, A. Bernard, K. Müller, P. Cheinet, V. Josse, M. Piraud, L. Pezzé, L. Sanchez-Palencia, A. Aspect and P. Bouyer, "Three-dimensional localization of ultracold atoms in an optical disordered potential", *Nat. Phys.* 8, 398-403 (2012).

[37] W. R. McGehee, S. S. Kondov, W. Xu, J. J. Zirbel and B. DeMarco, "Three-Dimensional Anderson Localization in Variable Scale Disorder", *Phys. Rev. Lett.* **111**, 145303 (2013).

[38] C. A. Müller and B. Shapiro, Comment on "Three-dimensional Anderson Localization in Variable Scale Disorder", *Phys. Rev. Lett.* **113**, 099601 (2014).

[39] W. R. McGehee, S. S. Kondov, W. Xu, J. J. Zirbel and B. DeMarco, "McGehee *et al.* Reply", *Phys. Rev. Lett.* **113**, 099602 (2014).

[40] W. Ketterle, D. S. Durfee, D. M. Stamper-Kurn, "Making, probing and understanding Bose-Einstein condesates". In *Bose-Einstein condensation in atomic gases*, Proceedings of the International School of Physics Enrico Fermi, Course CXL, edited by M. Inguscio, S. Stringari and C.E. Wieman (IOS Press, Amsterdam, 1999) pp. 67-176.

[41] M. Landini, "A tunable Bose-Einstein condensate for quantum interferometry" (PhD thesis), University of Trento, http://eprints-phd.biblio.unitn.it (2012).

[42] M. Landini, S. Roy, L. Carcagnì, D. Trypogeorgos, M. Fattori, M. Inguscio and G. Modugno, "Sub-Doppler laser cooling of potassium atoms", *Phys. Rev. A* **84**, 6 (2011).

[43] M. Landini, S. Roy, G. Roati, A. Simoni, M. Inguscio, G. Modugno and M. Fattori, "Direct evaporative cooling of ^{39}K atoms to Bose-Einstein condensation", *Phys. Rev. A* **86**, 6 (2012).

[44] C. J. Joachain, "Quantum Collision Theory", North Holland, Amsterdam (1983).

[45] C. Cohen-Tannoudji, J. DuPont-Roc and G. Grynberg, "Atom- Photon Interactions: Basic Processes and Applications", Wiley Science Paperback Series, Wiley (1998).

[46] W. Ketterle, N.J. van Druten, "Evaporative cooling of atoms", Advances in Atomic, Molecular, and Optical Physics, edited by B. Bederson and H. Walther, Vol. 37, 181-236 (1996).

[47] C. Chin, R. Grimm, P. Julienne, E. Tiesinga, "Feshbach Resonances in Ultracold Gases", *Rev. Mod. Phys.* **82**, 1225-1286 (2010).

[48] C. D'Errico, M. Zaccanti, M. Fattori, G. Roati, M. Inguscio, G. Modugno and A. Simoni, "Feshbach resonances in ultracold ^{39}K", *New J. Phys.* **9**, 223 (2007).

[49] J. W. Goodman, "Speckle Phenomena in Optics : Theory and Applications", (Roberts and Co. 2007).

[50] B. Shapiro, "Cold atoms in the presence of disorder", *J. Phys. A* **45**, 143001 (2012).

[51] G. Semeghini, M. Landini, P. Castilho, S. Roy, G. Spagnolli, A. Trenkwalder, M. Fattori, M. Inguscio and G. Modugno, "Measurement of the mobility edge for 3D Anderson localization", *Nat. Phys.* **11**, 554–559 (2015).

[52] M. Piraud, L. Pezzé and L. Sanchez-Palencia, "Matter wave transport and Anderson localization in anisotropic three-dimensional disorder", *Eur. Phys. Lett.* **99**, 50003 (2012).

[53] R. C. Kuhn, O. Sigwarth, C. Miniatura, D. Delande and C. A. Müller, "Coherent matter wave transport in speckle potentials", *New J. Phys.* **9**, 161 (2007).

[54] A. Yedjour and B. A. Van Tiggelen, "Diffusion and localization of cold atoms in 3D optical speckle", *Eur. Phys. J. D* **59**, 249–255 (2010).

[55] M. Piraud, L. Pezzé and L. Sanchez-Palencia, "Quantum transport of atomic matter waves in anisotropic two-dimensional and three-dimensional disorder", *New J. Phys.* **15**, 075007 (2013).

[56] D. Delande and G. Orso, "Mobility edge for cold atoms in laser speckle potentials", *Phys. Rev. Lett.* **113**, 060601 (2014).

[57] E. Fratini and S. Pilati, "Anderson localization of matter waves in quantum-chaos theory", *Phys. Rev. A* **91**, 061601 (2015).

[58] B. Deissler, M. Zaccanti, G. Roati, C. D'Errico, M. Fattori, M. Modugno, G. Modugno and M. Inguscio, "Delocalization of a disordered bosonic system by repulsive interactions", *Nat. Phys.* **6**, 354-358 (2010).

[59] Y. Dubi, Y. Meir, and Y. Avishai, "Nature of the superconductor–insulator transition in disordered superconductors", *Nature* **449**, 876 (2007).

[60] E. R. Mucciolo and C. H. Lewenkopf, "Disorder and electronic transport in graphene", *J. Phys. Condens. Matter* **22**, 273201 (2010).

[61] R. G. Endres, D. L. Cox, and R. R. P. Singh, "Colloquium: The quest for high-conductance DNA", *Rev. Mod. Phys.* **76**, 195 (2004).

[62] S. A. Gredeskul and Y. S. Kivshar, "Propagation and scattering of nonlinear waves in disordered systems",*Phys. Rep.* **216**, 1 (1992).

[63] T. Pertsch, U. Peschel, J. Kobelke, K. Schuster, H. Bartelt, S. Nolte, A. Tünnermann and F. Lederer, "Nonlinearity and Disorder in Fiber Arrays",*Phys. Rev. Lett.* **93**, 053901 (2004).

[64] T. Schwartz, G. Bartal, S. Fishman and M. Segev, "Transport and Anderson localization in disordered two-dimensional photonic lattices",*Nature* **446**, 52 (2007).

[65] Y. Lahini, A. Avidan, F. Pozzi, M. Sorel, R. Morandotti, D. N. Christodoulides and Y. Silberberg, "Anderson Localization and Nonlinearity in One-Dimensional Disordered Photonic Lattices",*Phys. Rev. Lett.* **100**, 013906 (2008).

[66] D.M. Basko, I.L. Aleiner and B.L. Altshuler, "Metal–insulator transition in a weakly interacting many-electron system with localized single-particle states", *Ann. Phys.* **321**, 1126–1205 (2006).

[67] L. Fallani, J. E. Lye, V. Guarrera, C. Fort and M. Inguscio, "Ultracold Atoms in a Disordered Crystal of Light: Towards a Bose Glass", *Phys. Rev. Lett.* **98**, 130404 (2007).

[68] M. Pasienski, D. McKay, M. White and B. DeMarco, "A disordered insulator in an optical lattice", *Nat. Phys.* **6**, 677 (2010).

[69] E. Lucioni, B. Deissler, L. Tanzi, G. Roati, M. Zaccanti, M. Modugno, M. Larcher, F. Dalfovo, M. Inguscio and G. Modugno, "Observation of Subdiffusion in a Disordered Interacting System", *Phys. Rev. Lett.* **106**, 230403 (2011).

[70] E. Lucioni, L. Tanzi, C. D'Errico, M. Moratti, M. Inguscio and G. Modugno, "Modeling the transport of interacting matter waves in a disordered system by a nonlinear diffusion equation", *Phys. Rev. E* **87**, 042922 (2013).

[71] B. Gadway, D. Pertot, J. Reeves, M. Vogt and D. Schneble, "Probing an ultracold-atom crystal with matter waves",*Phys. Rev. Lett.* **107**, 145306 (2011).

[72] C. D'Errico, E. Lucioni, L. Tanzi, L. Gori, G. Roux, I. P. McCulloch, T. Giamarchi, M. Inguscio and G. Modugno, "Observation of a Disordered Bosonic Insulator from Weak to Strong Interactions",*Phys. Rev. Lett.* **113**, 095301 (2014).

[73] M. Schreiber, S. S. Hodgman, P. Bordia, H. P. Lüschen, M. H. Fischer, R. Vosk, E. Altman, U. Schneider and I. Bloch, "Observation of many-body localization of interacting fermions in a quasirandom optical lattice", *Science* **349**, 842-845 (2015).

[74] M. Robert-de-Saint-Vincent, J.-P. Brantut, B. Allard, T. Plisson, L. Pezzé, L. Sanchez-Palencia, A. Aspect, T. Bourdel and P. Bouyer, "Anisotropic 2D Diffusive Expansion of Ultracold Atoms in a Disordered Potential", *Phys. Rev. Lett.* **104**, 220602 (2010).

[75] M.C. Beeler, M.E.W. Reed, T. Hong and S.L. Rolston, "Disorder-driven loss of phase coherence in a quasi-2D cold atom system", *New J. Phys.* **14**, 073024 (2012).

[76] J-P. Bouchaud and A .Georges, "Anomalous diffusion in disordered media: statistical mechanisms, models and physical applications", *Phys. Rep.* **195**, 127 (1990).

[77] R. Metzler and J. Klafter, "The random walk's guide to anomalous diffusion: a fractional dynamics approach", Phys. Rep. 339, 1 (2000).

[78] S. Flach, D. O. Krimer and C. Skokos, *Phys. Rev. Lett.* **102**, 024101 (2009).

[79] T. V. Laptyeva, J. D. Bodyfelt, D.O. Krimer, C.Skokos and S. Flach, "The crossover from strong to weak chaos for nonlinear waves in disordered systems", *EPL* **91**, 30001 (2010).

[80] K. Huang and H.-F. Meng, "Hard-sphere Bose gas in random external potentials", *Phys. Rev. Lett.* **69**, 644-647 (1992).

[81] T. Nattermann and V. L. Pokrovsky, "Bose-Einstein condensates in strongly disordered traps", *Phys. Rev. Lett.* **100**, 060402 (2008).

[82] S. Pilati, S. Giorgini and N. Prokof 'ev, "Superfluid transition in a Bose gas with correlated disorder", *Phys. Rev. Lett.* **102**, 150402 (2009).